Coupling of the Intertropical Convergence Zone and the Hadley Cells to the Ocean's Circulation

by

Brian Marcus Green

B.S.E. Aerospace Engineering
University of Michigan, 2007

M.E. Mechanical Engineering
Rensselaer Polytechnic Institute, 2012

Submitted to the Department of Earth, Atmospheric and Planetary Sciences
in partial fulfillment of the requirements for the degree of

Doctor of Science in Climate Science

at the

MASSACHUSETTS INSTITUTE OF TECHNOLOGY

September 2018

Signature redacted

Signature of Author .....
Department of Earth, Atmospheric and Planetary Sciences
August 31, 2018

Signature redacted

Certified by .....
John Marshall
Cecil and Ida Green Professor of Oceanography
Thesis Supervisor

Signature redacted

Accepted by .....
Robert D. van der Hilst
Schlumberger Professor of Earth and Planetary Sciences
Head of Department of Earth, Atmospheric and Planetary Sciences

Coupling of the Intertropical Convergence Zone and the Hadley Cells to the Ocean's Circulation

by

Brian Marcus Green

Submitted to the Department of Earth, Atmospheric and Planetary Sciences
on August 31, 2018, in partial fulfillment of the
requirements for the degree of Doctor of Science in
Climate Science

ABSTRACT

Patterns of tropical precipitation are sensitive to the atmosphere's energy balance and shift, for example, into the hemisphere heated most strongly by radiation and surface heat fluxes. By redistributing heat around the globe, the ocean circulation plays an important role in the atmosphere's energy balance and is a potentially strong control on the region of intense tropical rainfall known as the intertropical convergence zone, or ITCZ. This thesis explores several aspects of the coupling of the ocean's heat transport to the ITCZ and atmospheric circulation.

First, I study connections between Atlantic Ocean heat transport variability and the position of the ITCZ in the 20th Century. Using atmospheric reanalyses and reconstructions of tropical precipitation, I find correlations between sea surface temperatures in the North Atlantic, the ITCZ position, and tropospheric temperatures that are consistent with Atlantic Ocean-forced ITCZ shifts.

The rest of the thesis focuses on aspects of the coupling of the ocean's subtropical cells (STCs) to the ITCZ and the atmosphere's Hadley cells. By forcing an idealized atmosphere-ocean global climate model with an inter-hemispheric heating contrast, I find the STCs act to strongly damp the resulting ITCZ shift through their cross-equatorial heat transport, which partially compensates the imposed heating contrast. Coupled to the Hadley cells and ITCZ by the trade winds, heat transport by the STCs always acts to weaken ITCZ shifts and is a powerful control on the ITCZ position, keeping it "stuck" to latitudes near the equator. Applying the results from the idealized experiments, I estimate the STCs act to damp ITCZ shifts on Earth by a factor of two.

In the case of a hemispherically symmetric climate with the ITCZ on the equator, I study the influence of the STCs on the strength of the Hadley cells by performing a range of global warming and cooling experiments on the same idealized model. Compared to the case without any ocean heat transport, the STCs act to strongly weaken the Hadley cells, particularly in cold climates, by reducing the meridional heating contrast across the cells. Using a new energy balance framework to quantify this cross-cell heating contrast, I show that part of the impact of the STCs' poleward heat transport is offset by anomalous equatorward energy transport by atmospheric eddies. My results suggest the STCs act to weaken the Hadley cells further than previously thought.

Thesis Supervisor: John Marshall
Title: Cecil and Ida Green Professor of Oceanography

Acknowledgements

Compiling the chapters of this thesis has given me a sense of taking a tour of my years in graduate school, tracing a line from the first time I downloaded a dataset to when the final sentences were added to Chapter 6. My path to this point extends backward much further than these past six years, making recounting everyone who has helped me along it a seemingly impossible task. Nonetheless, dear reader, this feels like an appropriate moment to reflect on how I got here, and I would like to take a couple paragraphs to express my gratitude to a few people who have made this thesis possible.

Though my name is front and center on the first page, the research presented below was performed in collaboration with my advisor John Marshall and my thesis committee: Tim Cronin, Paul O'Gorman, Alan Plumb, and Gerard Roe. I would like to thank them for their support and feedback, as well as Aaron Donohoe, who made invaluable contributions to Chapter 2. In particular, I would like to thank John for responding, way back in 2011, to my unsolicited email seeking guidance on pursuing a career in climate science with the generous offer to chat about it on the phone; he has been equally generous with his time and ideas ever since. Learning the MITgcm has been a years-long process, and Jean-Michel Campin has been very patient with me and my many questions. Chapters 2 and 3 have been peer-reviewed and published already, and I would like to thank the editors and reviewers at *Geophysical Research Letters* and *Journal of Climate* for carefully reviewing the research and providing helpful comments. My teachers and teacher's assistants at MIT have given me a world-class education, and I am grateful to them for equipping me with the technical skills to conduct research in climate science. For my entire

time at graduate school, I have been spoiled with a paycheck, for which I have the Lord Foundation, MIT, and the National Oceanic and Atmospheric Administration to thank.

The support of my family and friends has been invaluable throughout all the highs and lows of graduate school but, to avoid both writing an acknowledgements section that is longer than the rest of this thesis and crying all over my keyboard, whose waterproofing and resistance to corrosion is suspect, I will simply list a few of them here. My family: Gordon Green, Yolanda Green, Amanda Blok, Ana Blok, Neil Blok. My friends: Dan Amrhein, Kyle Armour, Joern Callies, Ellie Doig, Aaron Donohoe, Margaret Duffy, Carl Gladish, Danielle Gruen, Mukund Gupta, Eric Heininger, Nick Hiebert, Yavor Kostov, Sophia Merrifield, Melissa Moulton, Tyler Rohr, Aditi Sheshadri, Stephanie Tillman, and Emily Zakem. Thank you all so much, and I look forward to celebrating with you soon.

Finally, I would like to thank my high school physics teacher, Gary Campbell, for first inspiring in me an interest in physics and how it shapes the world around me.

Contents

Chapter 1

Overview

1.1 The Intertropical Convergence Zone and the Atmosphere's Energy Balance

Tropical rainfall rates are the highest recorded on Earth in the annual mean (Figure 1.1a), delivering water to millions of people and playing an important role in the global hydrological cycle. Over the oceans, the distribution of rainfall is often organized into east-west bands which shift north and south seasonally following the following the solar heating. Over land, rainfall has a larger seasonal cycle, and there are strong summer monsoons in Asia, Africa, and South America. Land occupies a small fraction of the tropical surface, though, and the zonally averaged rainfall (Figure 1.1b) has many of the characteristics of the oceanic distribution, with a sharp peak centered just north of the equator.

The peak in the zonally averaged tropical rainfall distribution, termed the intertropical convergence zone (ITCZ), is fed by the surface convergence of air whose water vapor content is precipitated out in the ITCZ by moist convection. Upper-level divergence at the top of the convection balances this surface convergence, and the ITCZ forms the ascending branch of the atmosphere's meridionally overturning Hadley cells. Closed by descent in the subtropics of both hemispheres, the Hadley cells and ITCZ covary over the seasonal cycle, centered in the Northern Hemisphere (NH) during boreal summer and in the Southern Hemisphere (SH) during austral summer. Like the ITCZ, the Hadley circulation is biased north of the equator in the annual mean.

The Hadley cells are thermally direct circulations, with their upper branches having a higher energy content than their lower branches, transporting energy away from the ITCZ (Neelin and Held 1987) and across the equator in the annual mean (Donohoe et al. 2013). The latitude of the ITCZ, then, is anti-correlated with the atmosphere's cross-equatorial energy transport, with the Hadley cells transporting energy southward across the equator in NH summer and northward across the equator in SH summer. This coupling of the ITCZ to the Hadley cells and their cross-equatorial energy transport has profound implications for climate, tying the position of the ITCZ to the atmosphere's hemispheric energy balance. If one hemisphere's atmosphere is heated relative to the other, barring perfect compensation by fluxes of radiation at the top of the atmosphere, the Hadley cells are forced to transport a fraction of that heating across the equator and the ITCZ is shifted into the heated hemisphere (Kang et al. 2009). The energetic framework of Kang et al. (2009) has received a great deal of attention in recent years because it allows the position of the zonal mean ITCZ to be tied to a wide range of forcing agents (see the reviews of Chiang and Friedman (2012) and Schneider et al. (2014)).

Out of this energetic framework, the Atlantic Ocean's meridional overturning circulation (AMOC) has emerged as an important modulator of the ITCZ position. In the modern climate, the global ocean transports roughly 0.4 PW (1 PW = 10^{15} W) of heat northward across the equator in the annual mean (Marshall et al. 2014), with the Atlantic Ocean responsible for the majority of that transport (Trenberth and Caron 2001). This heat transport is balanced by a warmer NH fluxing more longwave radiation to space and the atmospheric circulation transporting energy southward across the equator. A large fraction of this southward cross-equatorial energy transport is accomplished by the Hadley cells. Because the longwave radiation imperfectly compensates the ocean's cross-equatorial heat transport, the position of the ITCZ in

the NH in the annual mean has been attributed to the AMOC's northward cross-equatorial heat transport (Frierson et al. 2013, Marshall et al. 2014).

The AMOC and its heat transport have also been implicated in past shifts of the ITCZ. Over the past 50,000 years, the North Atlantic has experienced a series of cooling events, termed stadials, which have been interpreted as a weakening of the AMOC and its cross-equatorial energy transport (Boyle and Keigwin 1987, Henry et al. 2016). Coincident with these NH coolings are indications of southward shifts of the ITCZ in a wide range of paleoclimate proxy records (Stager et al. 2011, Arbuszewski et al. 2013, Collins et al. 2013, McGee et al. 2018). Climate models simulating stadial events, often by "hosing" the North Atlantic with a large flux of freshwater to weaken the AMOC, show similar southward ITCZ shifts (Zhang and Delworth 2005, Broccoli et al. 2006), consistent with the energetic framework (McGee et al. 2014).

Paleoclimate proxy records are necessarily local, sparse, and indirect; there are few observationally-based estimates of the impact of AMOC variability on the global ITCZ position. Twentieth-Century observations show correlations between North Atlantic sea surface temperature (SST) variability and summer rainfall in India and northern Africa (Zhang and Delworth 2006), but the connection to the global ITCZ remain unclear. Recently, several reconstructions and reanalyses of the global atmospheric circulation and precipitation over the 20th Century have become available – can a signature of AMOC variability be detected in the ITCZ position? If so, can it be explained by the energetic framework?

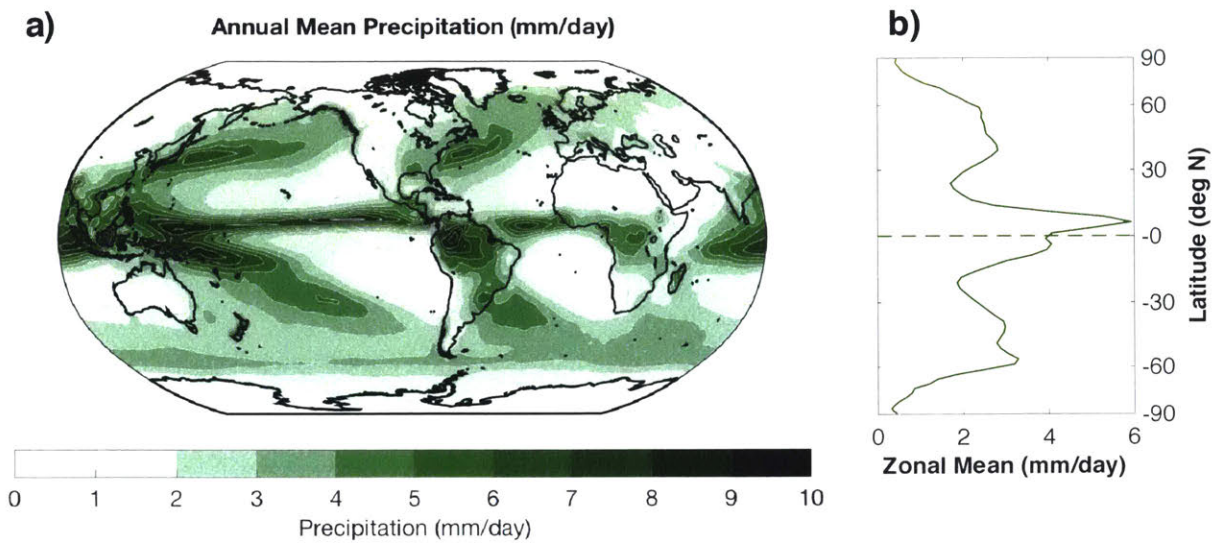

Figure 1.1. (a) Annual mean precipitation rate, averaged between 1979 and 2008, in the GPCP 2.2 product (Adler et al., 2003). (b) The annual mean precipitation rate averaged across longitudes (zonal mean).

1.2 Coupling of the Atmosphere and Ocean Circulations in the Tropics

Cross-equatorial energy transports and shifts in the ITCZ position have received a great deal of attention in the context of the atmosphere responding to changes in the ocean's deep overturning circulation, but the role of the shallower wind-driven circulation has been relatively unexamined. Despite being confined to the upper kilometer or so, by virtue of the relatively strong temperature gradients there, the wind-driven circulation is responsible for the majority of the global ocean's meridional transport of heat (Ferrari and Ferreira, 2011). While a deep overturning circulation appears to dominate heat transport in the Atlantic, it is virtually absent in the Pacific and Indian Oceans, where the wind-driven circulation is stronger.

The meridionally overturning subtropical cells (STCs, McCreary and Lu 1994) are the circulations responsible for the majority of the ocean's heat transport in the tropics, particularly in the Pacific and Indian Oceans (Klinger and Marotzke 2000). The surface branch of the STCs, in approximate Ekman balance with the surface wind stress, is driven poleward by the easterly trade winds in the Atlantic and Pacific Oceans. In those basins, the distribution of the trade winds results in Ekman suction of thermocline water to the surface near the equator and Ekman pumping of surface downward in the subtropics. Once subducted into the thermocline, the subtropical surface water flows toward the equator where it upwells to close the circulation. In the Indian Ocean, the annual mean surface wind stress drives surface flow southward across the equator, pumping it into the thermocline in the SH. The cooler subsurface water flows northward across the equator in a western boundary current, upwelling in the NH. Though the pathways of the subsurface return flow vary from basin to basin (see a review of the STCs in Schott et al. 2004), the STCs are efficient at transporting heat due to the temperature contrast between their warm surface branches and cooler subsurface branches.

Meridional energy transports by the atmosphere and wind-driven ocean are coupled by surface winds and temperatures, with important implications for the ITCZ. Because Ekman balance holds to within a couple degrees of the equator, the surface branches of the Hadley and subtropical cells are similar in strength. Taking advantage of this coupling, Held (2001) estimated the ratio of their energy transports as the ratio of the two circulations' vertical energy contrasts. Assuming the Hadley cells' ascending branches conserve moist static energy and the STCs' lower branches conserve the SSTs of the latitude where they are subducted, the ratio of their energy transports is a simple function of the surface temperature. As a result, the STCs are predicted to transport more energy meridionally near the equator, reflecting their larger vertical

energy contrast there, with the Hadley cells transporting more energy in the subtropics. This result represents a potentially powerful constraint on ITCZ dynamics: on timescales long enough for the wind-driven ocean circulation to adjust, its ability to transport heat might play an important role in the atmosphere's response to an inter-hemispheric heating contrast.

To date, though, the focus of modeling studies seeking to understand the climate's response to inter-hemispheric forcing has been on the atmosphere's response: the ocean has only played a passive role and is usually represented by a stationary "slab" layer (e.g. Kang et al. 2008, 2009; Frierson and Hwang 2012; Frierson et al. 2013). In the coupled system, the wind-driven ocean is constrained to move with the atmospheric circulation via the surface wind stress and shifts in the latter would be expected to drive shifts in the former, affecting the combined energy transport. Particularly as they relate to cross-equatorial energy transport, the STCs could play a major role in hemispheric energy balance, potentially transporting a large fraction of the energy imbalance across the equator. This would result in a smaller ITCZ shift and damping of the atmospheric response, raising several questions. Can the wind-driven ocean transport large quantities of heat across the equator, where Ekman balance breaks down? What role might this heat transport play in moderating ITCZ shifts and the atmosphere's energy budget? And how strongly does the climate system have to be forced to move the ITCZ significantly off of the equator?

1.3 The Strength of the Hadley Circulation

The result of Held (2001) also has important implications for the strength of the Hadley circulation. Earth's Hadley cells lie in a regime where the magnitude of their mass transport is set both by the meridional heating contrast across the cell (Schneider 1977, Held and Hou 1980,

Lindzen and Hou 1988, Plumb and Hou 1992) and the divergence of momentum fluxes by atmospheric eddies (Walker and Schneider 2006). In the limit where their strength is controlled solely by the heating contrast, the cells' upper branches conserve angular momentum as they flow away from the equator, leading to strong subtropical westerly jets. Waves originating in the extratropics break in the upper branch of the Hadley cells, weakening the subtropical jet but strengthening the poleward flow. Depending on the forcing agent, changes in either the heating contrast or the eddy momentum flux divergence can affect the strength of the cell (Merlis 2015, Tandon et al. 2013, Caballero 2007, Bordoni and Schneider 2008, Schneider and Bordoni 2008). Cooling the ascending branch of the Hadley cells and heating the descending branch, the STCs weaken the heating contrast, potentially weakening the circulation.

By coupling a simple representation of the STCs following Klinger and Marotzke (2000) to an atmospheric general circulation model, Levine and Schneider (2011) found that the STCs' heat transport consistently weakened the Hadley cells. Their analysis of the zonal momentum budget of the cells' upper branches shows that the weakening is primarily due to a reduced cross-cell heating contrast. Furthermore, their STCs reduce the rate of Hadley cell weakening in a warming world. Levine and Schneider focus their analysis of the mechanisms of Hadley cell expansion or weakening, but do not quantitatively discuss role the ocean plays in these processes. For example, they attribute a reduction of Hadley cell weakening by the STCs in warm climates to a reduction of the meridional temperature gradient, but do not discuss this result in the framework of Klinger and Marotzke (2000) and Held (2001).

This leaves several questions regarding the impact of the wind-driven ocean on the strength of the Hadley cells. First, is it true that a reduction in the STCs' gross stability in warm climates reduces their impact? Can other components of the climate system, such as radiation

and energy transport by atmospheric eddies, act to offset the effects of the STCs' heat transport? And can other components of the wind-driven circulation, such as the subtropical gyres and their poleward heat transport out of the subtropics, affect the strength of the Hadley cells?

1.4 The Contents of this Thesis

This thesis seeks to answer the questions outlined above, focusing on the connections between the AMOC and ITCZ shifts in the 20th Century, and the role of the STCs in moderating ITCZ shifts and the strength of the Hadley cells.

In Chapter 2, we (my collaborators and I) study correlations between multi-decadal indices of North Atlantic and North Pacific SSTs and the ITCZ position over the 20th Century. We find that on these timescales, estimates of the zonal mean ITCZ position from a statistical reconstruction and atmospheric reanalyses show northward shifts when the North Atlantic and North Pacific oceans are warm. In the case of the Atlantic-ITCZ connection, atmospheric reanalyses show corresponding northward shifts of the Hadley cells' ascent region, and a relatively warm NH troposphere, consistent with an inter-hemispheric heating contrast forced by the AMOC. In the case of the Pacific-ITCZ connection, only shifts of the ascent region are seen, and the mechanisms tying the three together are likely different than the one proposed by Kang et al. (2009). Sea surface temperatures in the North Atlantic are only indirectly linked to the AMOC and its heat transport, but our results contribute to the argument that, on decadal and longer timescales, the two are connected.

To study the influence of the STCs on the ITCZ and Hadley cells, we perform a series of idealized experiments using a fully coupled atmosphere-ocean version of the MITgcm (Marshall et al. 1997a, 1997b, 2004; Adcroft et al. 2004), comparing experiments with an active ocean

circulation to those where its heat transport are held fixed. Our goal is to study the coupling between the tropical atmosphere and ocean circulations in an idealized setting, with the view that our results and mechanisms can then be used to understand the behavior of more complex climate models and disentangle relationships from past and future observations. In each case, we apply our results to hypothetical climate change scenarios on Earth.

In Chapter 3, we force the model with an inter-hemispheric asymmetry of the surface albedo distribution, which heats the NH, cools the SH, and shifts the ITCZ northward. When the ocean circulation is allowed to adjust to the forcing, the ITCZ shift is damped by a factor of four relative to the case where the ocean's heat transport it held fixed. We attribute about half of this difference to the cross-equatorial heat transport by a wind-driven cross-equatorial cell (CEC) of the type seen in the Indian Ocean in the annual mean. The CEC, acting on the meridional SST gradient and driven by the surface wind stress distribution as described in Held (2001), is more efficient at transporting heat across the equator than the atmosphere, acting to offset the inter-hemispheric heating asymmetry and damping the ITCZ shift. We argue that, because the CEC is coupled to the Hadley cells above by the surface wind stress, it always acts to damp ITCZ shifts and that the ITCZ position is less sensitive to inter-hemispheric asymmetries in climate than previously thought.

In Chapter 4, we seek to understand how robust the damping of ITCZ shifts by the ocean circulation is, and how far it is possible to shift the ITCZ off of the equator. We run the MITgcm in a similar configuration as in Chapter 3, varying the forcing magnituide and distribution and again comparing the fully coupled case to one where the ocean circulation is held fixed. For inter-hemispheric heating asymmetries that are polar-amplified, the ocean is again efficient at damping ITCZ shifts, both through its cross-equatorial heat transport and by having secondary

impacts on the adjustment of the longwave radiation and the relationship between the ITCZ position and the Hadley cells' energy transport. If the forcing is confined to the tropics, the CEC is narrowed, increasing the temperature of the water supplying its lower branch and reducing the efficiency of its heat transport. Across the whole range of simulations, though, the CEC acts to damp the ITCZ shift, and we interpret our results for shifts of the Earth's ITCZ, estimating that a similar CEC could damp any meridional migrations by a factor of two.

The focus of Chapter 5 is on the impact of the STCs on the strength of the Hadley cells across a range of global warming and cooling simulations. For global mean SSTs ranging from -5 to 35 °C, the STCs always act to weaken the Hadley cells, primarily by reducing the meridional heating contrast across them. Using an energetic framework, we find that the poleward heat transport by the STCs is partially compensated by anomalous equatorward energy transport by atmospheric eddies relative to simulations where the ocean's heat transport is set to zero. Adding a pole-to-pole barrier in the ocean to create horizontally circulating gyres, we find that the Hadley cells are strengthened relative to the case without the barrier, primarily due to a weakening of the STCs rather than poleward heat transport by the gyres. Fluxes of angular momentum by atmospheric eddies are sensitive to the distribution of the zonal mean zonal winds in the upper troposphere, generally acting to further weaken the Hadley cells in the simulations with a fully coupled ocean. The STCs in our experiments weaken the Hadley cells more than in Levine and Schneider (2011), particularly in cold climates, because mixing at the STCs' poleward edge increases the gross stability and heat transport of the cell.

Our results, discussed in Chapter 6, indicate that the ocean circulation and heat transport play a leading-order role in the dynamics of the ITCZ and Hadley cell. Applications of the coupling of the ITCZ, trade winds, and ocean circulation to shifts of the ITCZ in the

paleoclimate record are discussed, as are connections between the wind-driven ocean circulation and the strength of the monsoon circulation. This thesis focuses on the behavior of the zonal mean ITCZ, and steps forward in extending this work to the study of regional precipitation variability are proposed.

Chapter 2

Twentieth Century Correlations Between Extratropical SST Variability and ITCZ Shifts

The inter-tropical convergence zone (ITCZ) is a global-scale band of tropical precipitation lying, in the annual mean, just north of the equator. Its position can be tied to the atmosphere's energy balance: the northern hemisphere is heated more strongly at the surface than the southern, biasing the atmosphere's circulation and ITCZ north of the equator to offset that heating. In the context of this energy balance framework, we examine multi-decadal connections between variations in the position of the global ITCZ and indices of extratropical sea surface temperature (SST) variability over the 20th Century. We find that the ITCZ and atmospheric circulation are shifted farther to the north during periods when the North Atlantic and North Pacific are anomalously warm. Additionally, a warmer North Atlantic is correlated with a relatively warm northern hemisphere atmosphere. Our results suggest an important role for the ocean circulation in modulating ITCZ migrations on decade-and-longer timescales.

[1]A slightly edited version of this chapter appeared in *Geophysical Research Letters* in September, 2017: Green, B., J. Marshall, and A. Donohoe, 2017: Twentieth century correlations between extratropical SST variability and ITCZ shifts. *Geophys. Res. Lett.*, 44, 9039-9047, doi: 10.1002/2017GL075044.

2.1 Extratropical SSTs, Cross-Equatorial Energy Transport, and the ITCZ Position

The ITCZ occupies a narrow range of latitudes, particularly in the Atlantic and eastern Pacific oceans (Figure 2.1a). It is located between the atmosphere's two Hadley cells, which are responsible for the majority of the atmosphere's meridional energy transport in the tropics (cf. Marshall et al. 2014 Figure 3) and migrates with those circulations over the course of the seasonal cycle (Donohoe et al., 2013). When the sun heats the northern hemisphere (NH) atmosphere more strongly during boreal summer, the Hadley cells (and ITCZ) are centered north of the equator and transport energy southward across the equator, opposing the solar heating imbalance. The opposite occurs during boreal winter, when the Hadley cells and ITCZ are centered in the southern hemisphere (SH).

This relationship between inter-hemispheric heating contrasts and the position of the ITCZ can be found across a large range of timescales (e.g. Donohoe et al. 2014, McGee et al. 2014), and a framework has emerged for interpreting their connection (Kang et al. 2009; see the review in Schneider et al. 2014). When the ocean, or a top-of-atmosphere radiative imbalance, preferentially heats one hemisphere's extratropical atmosphere relative to the other, eddies anomalously export a fraction of that energy into the tropics; the remainder is radiated away to space or stored in the climate system. The Hadley cells, and thus the ITCZ, shift into the warmer hemisphere and transport the excess energy across the equator into the cooler hemisphere. For example, northward cross-equatorial energy transport by the Atlantic meridional overturning circulation (AMOC), heating the NH and cooling the SH, has been argued by Frierson et al. (2013) and Marshall et al. (2014) to bias the ITCZ north of the equator in the annual mean. The sensitivity of the ITCZ position to inter-hemispheric heating contrasts has also been seen in

climate models simulating a range of forcings, including changes in high-latitude ice cover (Chiang and Bitz 2005), changes in the AMOC's energy transport (Zhang and Delworth 2005, Broccoli et al. 2006, Sun et al. 2013), and global warming (Frierson and Hwang 2012).

Across these simulations, changes in the sea surface temperature (SST) contrast between the NH and SH are correlated with meridional shifts in the Hadley cells and migrations of the ITCZ. Sea surface temperatures are, of course, only indirectly related to the heating or cooling of the atmosphere, but they have proven useful proxies when sufficient data to estimate the energy balance is unavailable (e.g. Zhang et al. 2007). Inter-hemispheric SST contrasts have been linked to ITCZ shifts in the paleoclimate record (McGee et al. 2014), in model simulations of paleoclimate (Donohoe et al. 2013) and appear to be connected to Sahel precipitation changes in the 20th Century (see the review in Chiang and Friedman 2012). Here we take an observational approach, guided by the energetic framework, to SST-ITCZ-atmospheric circulation relationships established in models but less rigorously studied in observations. For consistency with the Kang et al. (2009) framework we focus on extratropical SST variability; connections between that SST variability and the ocean circulation's energy transport are discussed in Section 2.4.

2.2 Twentieth Century Reconstructions and Reanalyses of SST, Precipitation, and Atmospheric Circulation

Two leading patterns of extratropical NH SST variability are the Atlantic multi-decadal oscillation (AMO; Kerr (2000); Figure 2.1c) and the Pacific decadal oscillation (PDO; Mantua et al. (1997); Figure 2.1d). Using the HadISST version 1.1 reconstruction from 1870-2012 (Rayner et al. 2003), we define the AMO index as the difference between average North Atlantic and

global mean SST, following Trenberth and Shea (2006). Its time series (Figure 2.2a) shows variability across a range of timescales, with multiple warm (1924-1966, 1995-2012) and cold (1902-1923, 1967-1994) periods lasting several decades. This broad-spectrum variability makes referring to the AMO (and PDO, for that matter) as an "oscillation" somewhat problematic; however, in keeping with convention, we will retain the original acronym. The SST anomalies associated with a 1σ warm anomaly of the annual mean AMO index (+0.14 K) show basin-wide warming in the North Atlantic, peaking at +0.5 K off of the eastern Canadian coast (Figure 2.1c).

The PDO index is often defined as the time series of the first principal component (PC) from an empirical orthogonal function (EOF) analysis of monthly mean SST anomalies from 20 °-70 °N in the Pacific (Mantua et al. 1997). When the PC time series is regressed back onto SST, the resulting pattern of SST anomalies shows cooling over almost all of the North Pacific (cf. Deser et al. 2010 Figure 10). Given this pattern of SST anomalies, we simplify the definition of the PDO by defining it similarly to the AMO, removing the global mean SST from its average value between 20 °N and 70 °N in the Pacific. Our resulting PDO index time series (Figure 2.2e) and spatial pattern of SST anomalies (Figure 2.1d) are both highly correlated with those resulting from an EOF analysis as in Mantua et al. (1997); R = -0.86 and -0.66, respectively (Appendix A1 Figure A1.1). Even though it is not identical to the original definition of the PDO, we feel our newly defined index is similar enough that we retain the original acronym.

We use the Smith et al. (2012; hereafter referred to as S12) precipitation reconstruction to analyze precipitation and ITCZ variability. It estimates monthly precipitation rates over the whole globe with a horizontal resolution of 5 ° and covers the years 1900-2008. Most of the precipitation associated with the ITCZ falls over the ocean, so by estimating precipitation over both land and ocean S12 provides a better estimate of the ITCZ's position than a land-only

reconstruction. Fitting EOFs calculated from the satellite-based Global Precipitation Climatology Project (GPCP) precipitation estimates to the Global Historical Climatology Network (GHCN) rain gauge reconstruction back to 1900, S12 also applies a correction to precipitation over the ocean using available SST and sea level pressure data. Tropical precipitation variability in the S12 reconstruction has been shown to match well with GPCP estimates, and when the reconstruction methodology is applied to an independent 20th Century reanalysis, it is able to reproduce large scale multi-decadal variability despite its relatively short reference period (Smith et al. 2013). Estimates of the time mean and zonal mean precipitation climatology are shown in Figure 2.1a, b. The ITCZ is clearly seen in the tropical Atlantic and Pacific, and zonal mean tropical precipitation peaks north of the equator.

Because rain gauge-based precipitation estimates are relatively sparse in the early part of the 20th Century (cf. Smith et al. 2012 Figure 2), we supplement the S12 reconstruction with two atmospheric reanalyses from the National Oceanic and Atmospheric Administration (NOAA) and the European Centre for Medium-Range Weather Forecasts (ECMWF). The NOAA 20th Century Reanalysis (Compo et al. 2011; hereafter referred to as N20CR) version 2 has 2° horizontal resolution and covers the years 1871-2011. The ECMWF's 20th Century reanalysis (Hersbach et al. 2015; hereafter referred to as E20CM), covers the years 1900-2010 at 0.125 ° horizontal resolution. Both reanalyses enforce SST and sea ice concentrations as boundary conditions and are forced by variations in incoming solar radiation, CO_2 concentrations, and aerosols; E20CM is also forced with varying ozone concentrations. Neither reanalysis assimilates observations of humidity, so their resulting precipitation estimates are strongly controlled by each model's treatment of moist physics and are not directly observationally constrained. Consequently, we only use these products to supplement the S12 reconstruction.

Defining the position of the ITCZ as the latitude that divides regions of equal total precipitation between 20 °N and 20 °S (the centroid, following Donohoe et al. 2013), time series of its annual mean anomalies about average positions of 1.7 °N, 1.9 °N, and 2.1 °N for S12, N20CR, and E20CM, respectively, are shown in Figure 2.2b-d. When low-pass filtered to isolate their multi-decadal variability (see Appendix A1.1 for details), all three ITCZ time series are correlated, with S12 and E20CM being the most similar: from 1900 to 2008, R = 0.69 between S12 and E20CM, 0.49 between S12 and N20CR, and 0.41 between E20CM and N20CR. Additionally, all three products' time series are highly correlated with observed inter-annual ITCZ variability over the satellite era (Appendix A1.2). While the three time series often differ for a given year, a consistent feature of multi-decadal ITCZ variability is seen in all three products: the ITCZ was located southward earlier in the century, further north after 1930, and moved south again around 1980.

To estimate atmospheric circulation anomalies, we use the NCEP/NCAR reanalysis (Kalnay et al. 1996) from 1948 to 2012. We define an index of Hadley cell strength at the equator (Ψ_{eq}) as the value of the vertically averaged mass transport streamfunction at the equator, and an index of the inter-hemispheric temperature contrast in the troposphere ($T_{interhem}$) as the difference between NH and SH average temperatures between the surface and 300 hPa. See Appendix A1.1 for additional details on the calculations. While the atmospheric circulation and temperatures in the NCEP/NCAR reanalysis are constrained by radiosonde observations, E20CM and N20CR are forced primarily at the surface by SSTs. Tropical SSTs and large-scale precipitation have dynamic and thermodynamic connections (see the review in Sobel (2007)), making E20CM and N20CR output useful for studying ITCZ dynamics, but SSTs alone do not

sufficiently constrain the atmospheric circulation above the surface. As such, we limit discussions of circulation anomalies in E20CM and N20CR to Appendix A1.3.

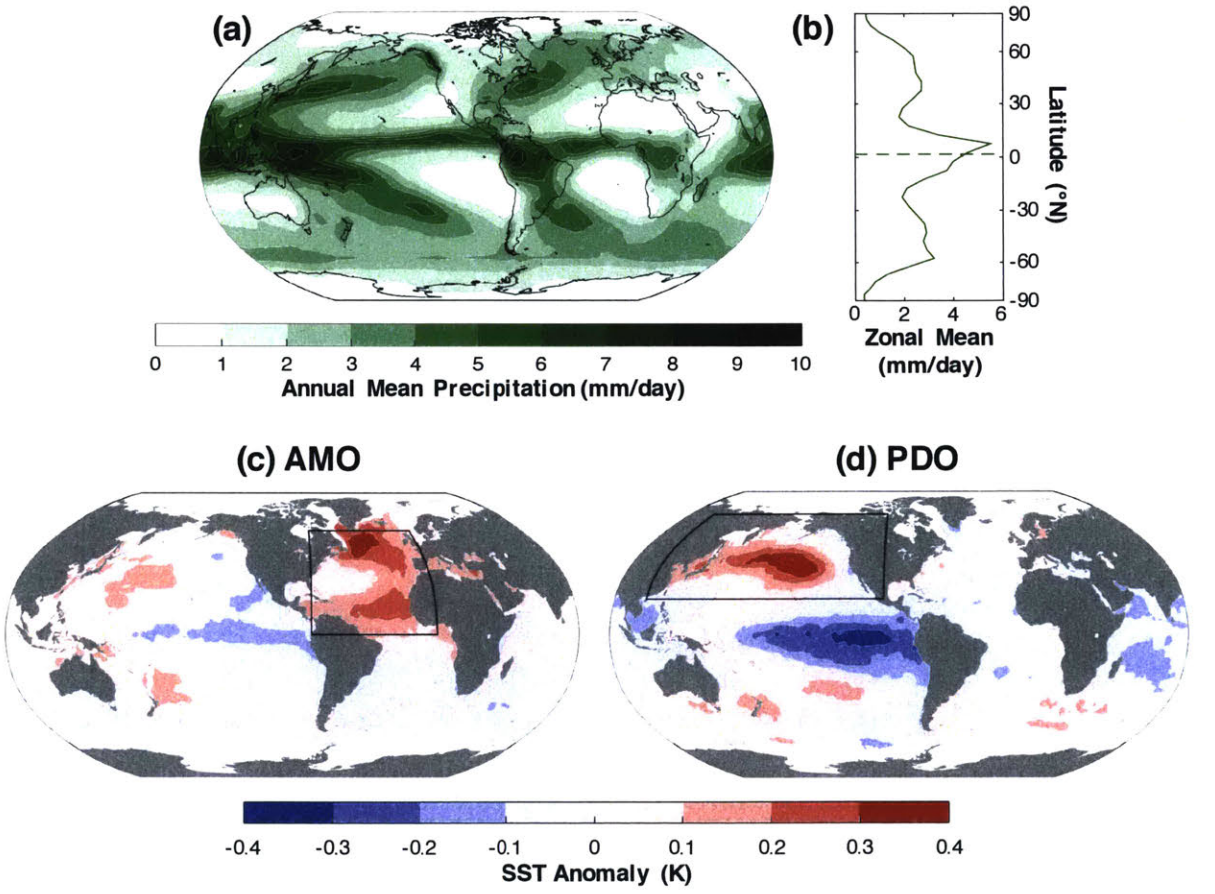

Figure 2.1. Precipitation climatology and patterns of North Atlantic and North Pacific SST variability. Top: annual mean (a) precipitation rate (contour interval: 1 mm/day) and its (b) zonal average from the Smith et al. (2012) reconstruction. The green dashed line indicates the time mean ITCZ position of 1.7 °N. Bottom: SST anomalies regressed against +1σ of the annual mean (c) AMO and (d) PDO indices. The contour interval is 0.1 K. Black lines indicate the regions SSTs are averaged over to generate the AMO and PDO indices.

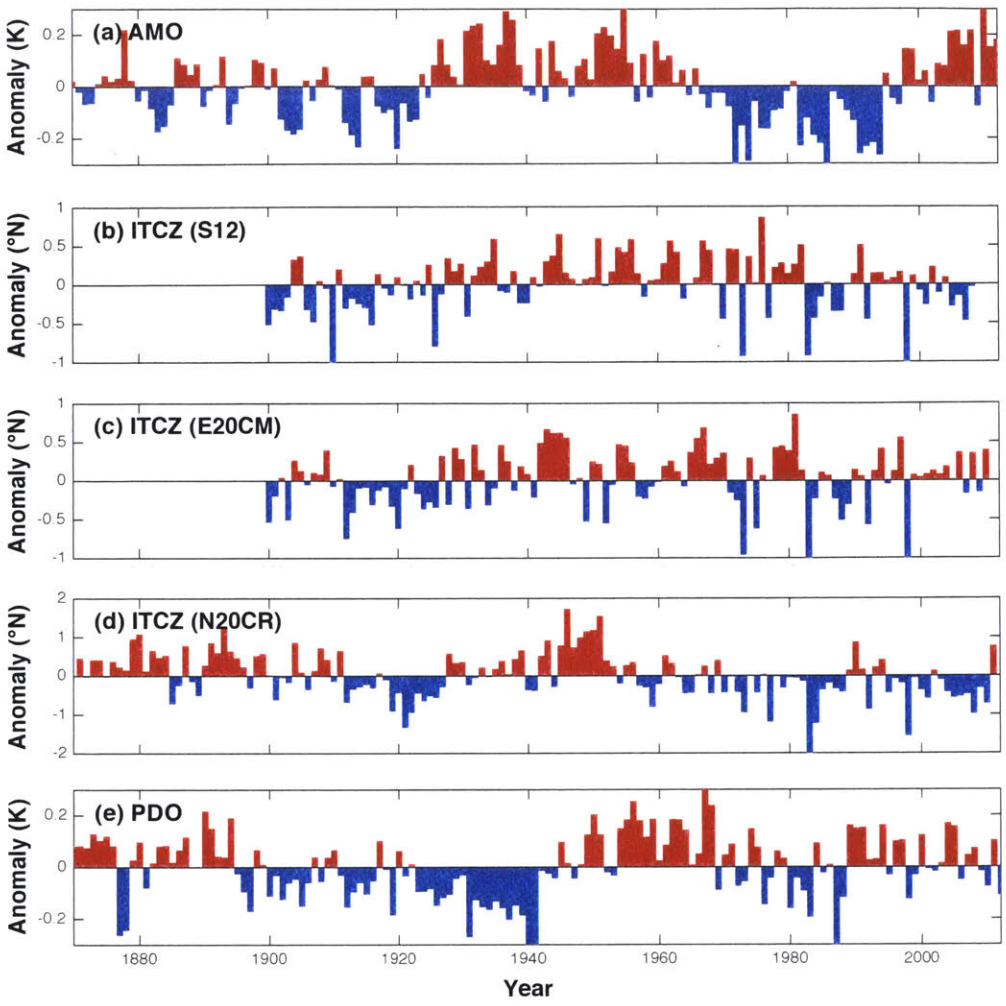

Figure 2.2. Time series of annual mean (a) AMO index, (b) S12 ITCZ position, (c) E20CM ITCZ position, (d) N20CR ITCZ position, and (e) PDO index anomalies.

2.3 ITCZ, AMO/PDO, and Tropospheric Co-Variability

To test for connections between extratropical SSTs and the ITCZ position, we perform a multiple regression analysis on the ITCZ position using the AMO and PDO indices as predictors, low-pass filtering each time series using a cutoff period of 10 years to isolate its multi-decadal variability (see Appendix A1.1 for details). We find that the S12 ITCZ shifts north when the

North Atlantic and Pacific are warm: a $+1\sigma$ (+0.14 K) AMO anomaly is associated with a northward ITCZ shift of $0.07\,° \pm 0.05\,°$ and a $+1\sigma$ (+0.12 K) PDO anomaly is associated with a northward ITCZ shift of $0.10\,° \pm 0.06\,°$ (Appendix A1 Table A1.1). Error estimates are for a $\pm 1\sigma$ confidence interval. The AMO and PDO indices each explain roughly 10 % of the ITCZ variance on multi-decadal timescales ($R^2 = 0.11$ and 0.14, respectively).

In the NOAA and ECMWF reanalyses, the ITCZ position is correlated with the AMO index, but not necessarily with the PDO index. The AMO-ITCZ correlations are significant to 1σ (N20CR: $R^2 = 0.12$, E20CM: $R^2 = 0.20$), but the PDO-ITCZ correlations are only significant in the N20CR product ($R^2 = 0.06$). The ITCZ shifts associated with a warm phase AMO are larger in the reanalyses than in S12 but are still within error estimates of each other (Appendix A1 Table A1.1). It should be noted that the AMO and PDO indices are not correlated with one another ($R^2 = 0.00$ for the low-pass filtered time series), making the total fraction of the ITCZ's variance explained by the multiple regression analysis equal to the sum of the two R^2 values.

Complex spatial patterns are seen in the precipitation anomalies associated with a northward ITCZ shift (Figure 2.3a). When low-pass filtered precipitation anomalies are regressed against a northward shift of the ITCZ position, statistically significant (to 1σ) anomalies in the tropics peak in the West Pacific, with a smaller north-south dipole in the Atlantic. Locally, these anomalies can reflect a pure shift in the ITCZ position (such as those seen in the central Pacific), a contraction/intensification of the local ITCZ (West Pacific), or a combination of the two (Atlantic). In the zonal mean, these anomalies project neatly onto a positive-negative dipole centered on the time mean ITCZ position (Figure 2.3b), reflecting a northward shift of the precipitation centroid.

Precipitation anomaly patterns indicative of northward ITCZ shifts are also seen when low-pass filtered anomalies are multiple-regressed against the AMO and PDO indices. Maps of S12 precipitation anomalies associated with warm phase AMO and PDO indices (Figure 2.3c, e) have significant (to 1σ) spatial correlations with those associated with a northward ITCZ shift: between 20 °N and 20 °S, $R_{AMO,ITCZ} = 0.65$ and $R_{PDO,ITCZ} = 0.54$. Statistically significant precipitation anomalies associated with a warm phase AMO show a tri-pole pattern in the western Pacific similar to those associated with a northward ITCZ shift, and significant positive anomalies in the northern tropical Atlantic and Sahel are consistent with those in Zhang and Delworth (2006). The pattern of anomalies associated with a warm phase PDO is slightly different, with a north-south dipole in the central Pacific. These central Pacific anomalies are statistically significant, but the anomalies in the western and southern Pacific are not. North-south dipoles of precipitation anomalies centered on the time mean ITCZ position are seen when zonal mean precipitation anomalies are multiple-regressed against the AMO and PDO indices (Figure 2.3d, f), consistent with a northward shift of the precipitation centroid.

In the reanalyses, similar precipitation anomaly patterns are seen for a northward ITCZ shift and a warm North Atlantic, and the anomalies associated with warm phases of the AMO and PDO in both E20CM and N20CR remain largest in the western and central Pacific, respectively (Appendix A1 Figures A1.2, A1.3). The zonal mean precipitation anomalies in Appendix A1 Figure A1.3f show that the statistically significant PDO-ITCZ position correlation in N20CR is a result of subtropical precipitation anomalies projecting onto the centroid metric, rather than a shift or intensification of the zonal mean tropical precipitation maximum. For the regressions onto both the ITCZ position and local precipitation anomalies, the reanalyses support

the AMO-ITCZ connection seen in the S12 reconstruction, but they cast doubt on the connection between the PDO and the ITCZ position.

Consistent with northward ITCZ shifts, we also find correlations between anomalies in the Hadley cells, inter-hemispheric tropospheric temperature contrasts, and the AMO and PDO indices in the NCEP/NCAR reanalysis. During warm phases of the AMO and PDO, anomalous cross-equatorial Hadley cells are seen (Figure 2.4a, b), with rising motion north of the equator. We also observe anomalous inter-hemispheric temperature contrasts reflecting a relatively warm NH troposphere (Figure 2.4c, d). Temperature anomalies associated with a warm North Atlantic are spread over the depth of the troposphere with a local maximum of 0.15 K near the surface (at 850 hPa) and are significant (to 1σ), while those associated with a warm North Pacific peak in the middle troposphere (at 700 hPa) with a weaker magnitude of 0.10 K and are not significant. Conversely, streamfunction anomalies associated with the PDO are larger than those associated with the AMO: the 7.4 Sv maximum anomaly in Figure 2.4b is larger than the 4.8 Sv maximum anomaly in Figure 2.4a. While both streamfunction anomalies are significant (to 1σ), are not significantly different from each other.

Regressing the AMO and PDO indices against the Ψ_{eq} and $T_{interhem}$ indices from the NCEP/NCAR reanalysis, we find that the AMO explains more of their variance than the PDO does (Appendix A1 Table A1.1). At multi-decadal timescales, the AMO index is (to 1σ) significantly correlated with both inter-hemispheric atmospheric temperature contrasts and cross-equatorial mass transport by the Hadley cells ($R^2 = 0.74$ and 0.41, respectively). It is remarkable to note that the AMO index explains over 70 % of the low-pass filtered inter-hemispheric tropospheric temperature contrast. While the PDO is significantly correlated with Ψ_{eq} ($R^2 = 0.17$), it is not significantly correlated with $T_{interhem}$ ($R^2 = 0.02$), reflecting the lack of significance

in the temperature anomalies in Figure 2.4d. This suggests different mechanisms connect the AMO and PDO to ITCZ shifts.

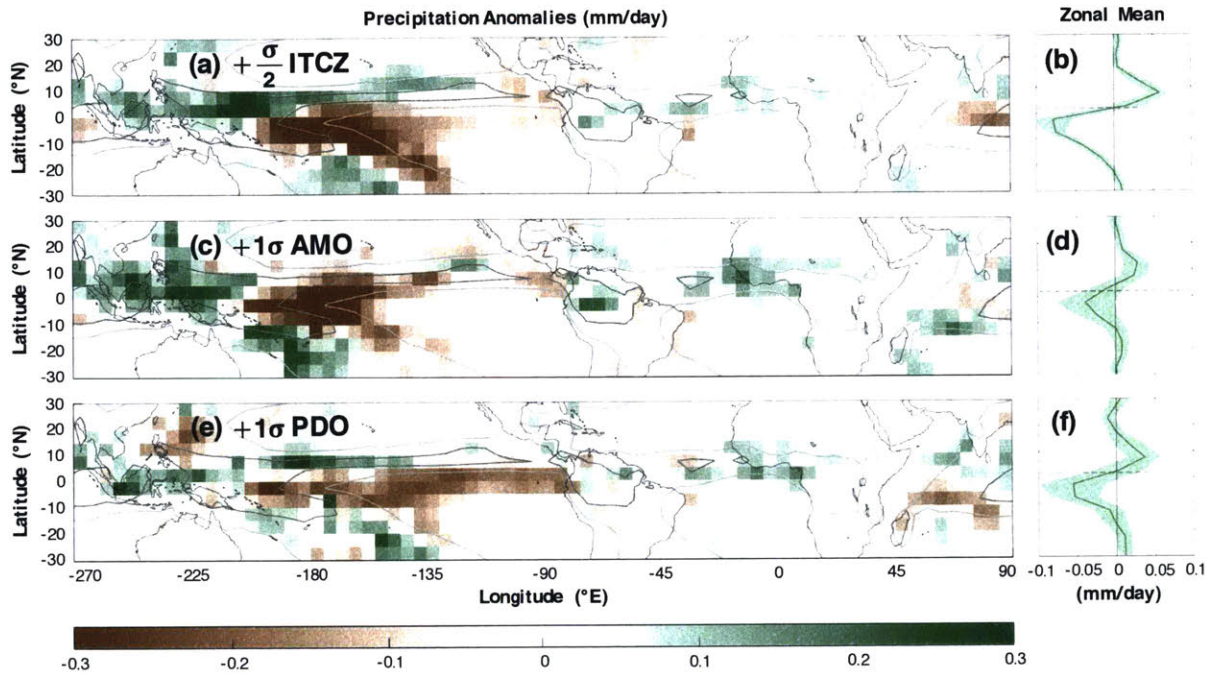

Figure 2.3. Maps of S12 precipitation anomalies. (a, c, e) Local precipitation anomalies and their (b, d, f) zonal averages regressed against (a, b) +σ/2 ITCZ shift, (c, d) +1σ AMO index, and (e, f) +1σ PDO index. Light and dark grey contours show the 3 mm/day and 6 mm/day climatology of annual mean precipitation, respectively. Green shadings around the zonal mean anomalies are ±1σ error estimates, and the green dashed line indicates the time mean ITCZ position of 1.7 °N.

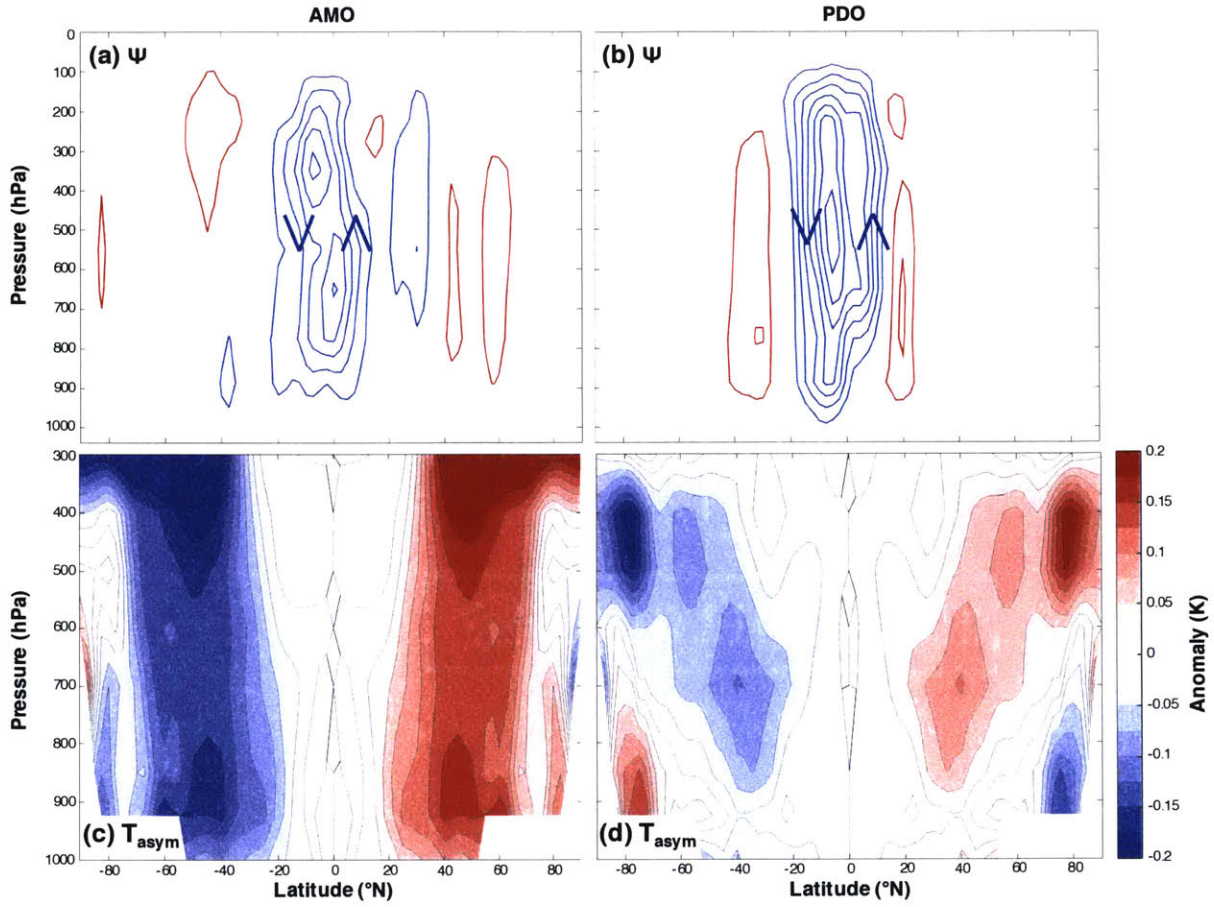

Figure 2.4. Atmospheric circulation anomalies. Top: meridional overturning streamfunction anomalies from the NCEP/NCAR reanalysis regressed onto (a) +1σ AMO and (b) +1σ PDO anomalies. Blue contours indicate negative anomalies and counter-clockwise rotation, indicated by chevrons, and red contours indicate positive anomalies and clockwise rotation. The contour interval is 1 Sv (10^9 kg/s) and the zero contour is not shown. Bottom: the hemispherically asymmetric component of zonal mean temperature anomalies (see Appendix A1.1) associated with (c) +1σ AMO and (d) +1σ PDO anomalies. Contour interval: 0.025 K.

2.4 Discussion of Timescales and Mechanisms

Our observed correlations between a warm North Atlantic, northward ITCZ and Hadley cell shifts, and inter-hemispheric tropospheric temperature contrasts are all consistent with the framework proposed in Kang et al. (2009) in which the atmosphere is forced by an inter-hemispheric heating contrast. We propose that these correlations are the result of a warm North Atlantic fluxing energy upwards into the atmosphere, a cool North Atlantic removing energy from the atmosphere, and that they are at least in part due to variations in the Atlantic Ocean's cross-equatorial energy transport. The relationship between North Atlantic SSTs and surface energy fluxes, though, is a function of timescale. On inter-annual timescales, warm SSTs are correlated with downward surface energy fluxes, indicating forcing by the atmosphere rather than the ocean (Gulev et al. 2013). The pattern of SST anomalies associated with a high-pass filtered AMO index (using a 10-year cutoff period) is very similar to that associated with the negative phase of the North Atlantic oscillation (NAO; Hurrell (1995); Appendix A1 Figure A1.4), a measure of internal atmospheric variability (Marshall et al. 2001). The NAO and high-pass filtered AMO time series are correlated, with R = -0.34 between 1870 and 2012, and regressions using a high-pass filtered AMO index explain much less variance of the ITCZ position ($R^2 = 0.04$), Ψ_{eq} ($R^2 = 0.01$), and $T_{interhem}$ ($R^2 = 0.24$) than the low-pass filtered time series does. Therefore, we do not expect the Kang et al. (2009) framework to apply to inter-annual AMO-ITCZ variability.

Conversely, on multi-decadal timescales a warm North Atlantic is correlated with upward surface energy fluxes (Gulev et al. 2013), which we interpret as the ocean circulation forcing the atmosphere by converging heat into the North Atlantic. Stochastic forcing by the atmosphere has been invoked to explain multi-decadal SST variability in the North Atlantic (Clement et al. 2015,

Clement et al. 2016), and after 1990 the AMO sharply transitions from a cool phase to a warm phase without any apparent northward shift of the ITCZ (Figure 2.2). It is possible that other forcing agents such as greenhouse gases and aerosols are contributing to these late 20th Century SST anomalies (Friedman et al. 2013), obscuring the impact of AMOC variability on the atmosphere's energy balance during that period. However, the observed positive SST-upward surface energy flux correlation over the full extent of the 20th Century cannot be explained without a role for ocean energy transport convergence (Zhang et al. 2016, O'Reilly et al. 2016). Furthermore, the Kang et al. (2009) framework we employ only requires an upward flux of energy at the surface into the atmosphere without specifying the processes responsible for that flux.

The mechanisms connecting North Pacific SSTs to ITCZ position and Hadley cell anomalies are likely different than for North Atlantic SSTs. The Pacific Ocean transports less energy across the equator than the Atlantic (Trenberth and Caron 2001), and its energy transport is thought to be dominated by shallow wind-driven circulations rather than a deep overturning circulation like the AMOC (Ferrari and Ferreira, 2011). Decadal SST variability in the North Pacific may be forced by, for example, the El Niño-Southern Oscillation (ENSO), ocean circulation variability, and extratropical atmospheric variability (Schneider and Cornuelle 2005), making PDO-ITCZ connections likely the result of a combination of processes. We do not find significant correlations between ENSO's Niño-3 index and the ITCZ position (S12: $R^2 = 0.00$, N20CR: $R^2 = 0.05$, E20CM: $R^2 = 0.03$), and inter-hemispheric temperature contrast and Hadley cell anomalies associated with one standard deviation of the Niño-3 index (not shown) are about half as strong as they are for the PDO anomalies in Figure 2.4. Tropical forcing of North Pacific SSTs does contribute to PDO index anomalies, though, and 300 hPa height anomalies show a

distinctive wave train pattern originating in the tropics when regressed against the PDO (Appendix A1 Figure A1.5). So, even though ENSO in our analysis does not appear to directly influence the ITCZ position, it could have an indirect influence through teleconnections to the extratropical atmosphere.

In conclusion, we have shown that the AMO explains a significant fraction of multi-decadal ITCZ variance across several estimates of 20th Century precipitation, but those estimates disagree on the influence of the PDO. In particular, despite being confined to the smaller Atlantic basin, the AMO explains 41 % of Hadley cell variability at the equator and a remarkable 74 % of the inter-hemispheric tropospheric temperature variability in the NCEP/NCAR reanalysis. It is believed that on multi-decadal timescales the AMO is affected by variations in the strength of the AMOC (see the review by Buckley and Marshall 2016), a driver of climate and climate variability that connects the two hemispheres. Moreover, the AMOC has predictability on decadal timescales (Tulloch and Marshall 2012), suggesting that AMOC predictability could be leveraged for the predictability of ITCZ migrations, with implications for precipitation variability along the entire tropical belt.

Chapter 3

Coupling of Trade Winds with Ocean Circulation Damps ITCZ Shifts

The position of the inter-tropical convergence zone (ITCZ) is sensitive to the atmosphere's hemispheric energy balance, lying in the hemisphere most strongly heated by radiative and turbulent surface energy fluxes. This study examines how the ocean circulation, through its cross-equatorial energy transport and associated surface energy fluxes, affects the ITCZ's response to an imposed inter-hemispheric heating contrast in a coupled atmosphere-ocean general circulation model. Shifts of the ITCZ are strongly damped due to a robust coupling between the atmosphere's Hadley cells and ocean's sub-tropical cells by the trade winds and their associated surface stresses. An anomalous oceanic wind-driven cross-equatorial cell transports energy across the equator, strongly offsetting the imposed heating contrast. The circulation of this cell can be described by the combination of trade wind anomalies and the meridional gradient of sea surface temperature, which sets the temperature contrast between its upper and lower branches. The ability of the wind-driven ocean circulation to damp ITCZ shifts represents a previously unappreciated constraint on the atmosphere's energy budget and indicates that the position of the ITCZ may be much less sensitive to inter-hemispheric heating contrasts than previously thought. Climatic implications of this damping are discussed.

[1]A slightly edited version of this chapter appeared in *Journal of Climate* in June, 2017: Green, B., and J. Marshall, 2017: Coupling of Trade Winds with Ocean Circulation Damps ITCZ Shifts. *J. Climate*, 30, 4395-4411, doi:10.1175/JCLI-D-16-0818.1.

3.1. Introduction and Background

Tropical rainfall is often organized into East-West bands, which collectively are referred to as the inter-tropical convergence zone. The global ITCZ moves between the Northern and Southern hemispheres (NH, SH) over the seasonal cycle, following the sun's heating, and resides in the NH in the annual mean (Donohoe et al. 2013). Large scale vertical motion in the tropical atmosphere is collocated with the ITCZ, where moist convection reduces the stratification experienced by those flows (Emanuel et al. 1994, Neelin 1997). Consequently, the ITCZ co-varies with the ascending branch of the Hadley circulation, whose two cells are closed by descent in the subtropics and are shown schematically in Figure 3.1. These two thermally direct cells transport energy in the direction of their upper branches, poleward and away from the ITCZ. The ITCZ's position is then anti-correlated with the atmosphere's cross-equatorial energy transport and lies in the hemisphere from which the Hadley circulation transports energy in the long-term mean (Marshall et al. 2014, Frierson et al. 2013), over the seasonal cycle (Donohoe et al. 2013), and in inter-annual variability (Donohoe et al. 2014, Adam et al. 2016).

The relationship between the ITCZ position and atmospheric cross-equatorial energy transport is shown schematically in Figure 3.1. When the ITCZ and Hadley cells are biased north of the equator (Figure 3.1a), the total Hadley circulation can be thought of as a superposition of hemispherically symmetric (Figure 3.1b) and asymmetric components (Figure 3.1c). At a given latitude ϕ, this decomposition of the total meridional overturning streamfunction ψ is expressed as

$$\psi(\phi) = \psi_{Sym}(\phi) + \psi_{Asym}(\phi) \quad (3.1a)$$

$$\psi_{Sym}(\phi) = \frac{1}{2} \cdot [\psi(\phi) - \psi(-\phi)] \quad (3.1b)$$

$$\psi_{Asym}(\phi) = \frac{1}{2} \cdot [\psi(\phi) + \psi(-\phi)]. \quad (3.1c)$$

Because the symmetric Hadley cells cannot transport mass and energy across the equator, the asymmetric cells are entirely responsible for the cross-equatorial energy transport. With rising air in the NH and descent closing the circulation in the SH, the asymmetric cell rotates counter-clockwise for an ITCZ residing in the NH; it rotates in the opposite sense if the ITCZ is in the SH. Combined with a positive stratification (gray lines, Figure 3.1a), the asymmetric Hadley cell transports energy southward across the equator away from the ITCZ.

A corollary of the connection between ITCZ position and cross-equatorial energy transport by the atmosphere is that the ITCZ is sensitive to the atmosphere's hemispheric energy balance. Heating of one hemisphere's atmosphere relative to the other affects the ITCZ's position by inducing the atmosphere to transport a fraction of the heating imbalance across the equator, a process sometimes referred to as "compensation" (Kang et al. 2008). As a result, the ITCZ resides in the hemisphere heated most strongly by the combination of radiative fluxes at the surface and top-of-atmosphere, and surface fluxes of sensible and latent heat. Its position can then be affected by a variety of factors not necessarily confined to the tropics and is sensitive to any hemispherically asymmetric forcing (see the review in Schneider et al. 2014).

Within this energy balance framework, several modeling studies have sought to understand the ITCZ's response to a variety of forcings and feedbacks. For example, if an anomalous freshwater flux is added to the North Atlantic, the ITCZ shifts southward as a slowdown in the Atlantic's meridional overturning circulation (AMOC) fluxes less energy across the equator and into the extratropical NH atmosphere (Zhang and Delworth 2005, Broccoli et al. 2006). Increases in NH high latitude ice cover, via their impact on surface albedo, can cool the atmosphere and result in a southward ITCZ shift away from the cooling (Chiang and Bitz 2005, Broccoli et al. 2006). Clouds have a strong impact on the Earth's energy budget, and hemispheric asymmetries in their distribution can lead to ITCZ biases in climate models (Hwang and Frierson 2013) and can affect the magnitude of the ITCZ's response to inter-hemispheric albedo contrasts (Voigt et al. 2014).

The focus of the above studies has been on the atmosphere's ability to compensate an inter-hemispheric heating contrast by shifting the ITCZ and transporting energy across the equator. Compared to the ocean, though, the atmosphere is inefficient at transporting energy in the tropics, where moist convection and the weak effects of rotation lead to weak moist static energy gradients away from the surface (Charney 1963, Neelin and Held 1987, Czaja and Marshall 2006). Thus, the Hadley cells in the deep tropics cannot act on large energy gradients to transport energy. In contrast, the tropical ocean is strongly stratified in temperature and the wind-driven sub-tropical cells (STCs, McCreary and Lu 1994) efficiently transport energy away from the equator due to the surface temperature difference between the tropics and subtropics (Klinger and Marotzke 2000, Held 2001, Czaja and Marshall 2006). Even though the STCs transport less mass than the Hadley cells, the ocean circulation is estimated to cool the tropics more strongly than the atmosphere in the annual mean (Trenberth and Caron 2001).

The STCs, because they are driven by trade winds imparting a surface stress, are strongly coupled to shifts in the Hadley circulation and the ITCZ. A northward shift of the ITCZ is accompanied by a weakening of the easterly wind stress in the NH and an enhancement in the SH (Lindzen and Hou 1988). This asymmetric pattern drives southward Ekman flow in the ocean in both hemispheres. If this warm southward surface flow crosses the equator, and is returned at depth at cooler temperatures, a southward cross-equatorial energy transport would result which cools the NH. This NH cooling would push the ITCZ southward, damping the initial northward shift. Hemispherically asymmetric wind stress patterns drive cross-equatorial near-surface flow and energy transports in, for example, the Indian Ocean in the annual mean (Miyama et al. 2003) and the global ocean over the seasonal cycle (Jayne and Marotzke 2001).

Here we explore the role of the ocean circulation and its cross-equatorial energy transport in damping ITCZ shifts in response to a heating of one hemisphere relative to the other. We find that cross-equatorial energy transport by the ocean is able to strongly compensate the imposed inter-hemispheric heating contrast, damping an ITCZ shift by a factor of four compared to the case where the ocean circulation is not allowed to respond to the forcing. The Hadley cells and STCs accomplish the majority of the cross-equatorial energy transport in the atmosphere and ocean, and their respective strengths are coupled by the surface wind stress associated with the trade winds. Similar to the atmosphere in Figure 3.1, the ocean circulation and surface wind stress distribution can be decomposed into symmetric and asymmetric components, with the asymmetric component of the ocean circulation responsible for its cross-equatorial energy transport. We will show that the asymmetric atmosphere and ocean circulations are coupled by the asymmetric trade wind stress distribution and are thus constrained to overturn in the same sense. Furthermore, because their upper branches have higher energy densities than their lower

branches, the Hadley cells and STCs will always transport energy in the same direction, damping ITCZ shifts compared to the atmosphere-only case.

Coupling of the Hadley cells and the STCs by the surface wind stress distribution, and the resulting implications for meridional energy transport, has been discussed for a hemispherically symmetric atmosphere by Held (2001) and Czaja and Marshall (2006). However, the coupling of the asymmetric circulations, their cross-equatorial energy transport, and the implications for ITCZ shifts have only been speculated on in passing in Box 1 of Schneider et al. (2014). Recent studies with coupled ocean-atmosphere GCMs note that the ocean and its cross-equatorial energy transport can damp ITCZ shifts in response to changes in Southern Ocean cloud properties (Kay et al. 2016, Hawcroft et al. 2016, Mechoso et al. 2016) and Artic sea ice concentrations (Tomas et al. 2016), but the mechanisms responsible for this damping remain unclear. Our results and analysis propose that a wind-driven hemispherically asymmetric ocean circulation might be responsible for the damped ITCZ shifts in these studies.

Our paper is set out as follows. In Section 3.2, we describe experiments in which a coupled atmosphere-ocean general circulation model (GCM) is forced by an inter-hemispheric albedo contrast. The model is run both with and without an active ocean circulation to highlight the role of the ocean's circulation in the model's response to the forcing. In Section 3.3, we analyze the resulting ITCZ shifts in terms of the hemispheric energy balance, showing how cross-equatorial energy transport by the ocean can damp ITCZ shifts. In Section 3.4, we show how the surface wind stress coupling the two fluids results in a wind-driven ocean circulation that always damps ITCZ shifts. In Section 3.5 we describe the characteristics of the anomalous cross-equatorial ocean cell, comparing it to the circulation of the Indian Ocean. A summary and discussion of the results follows in Section 3.6.

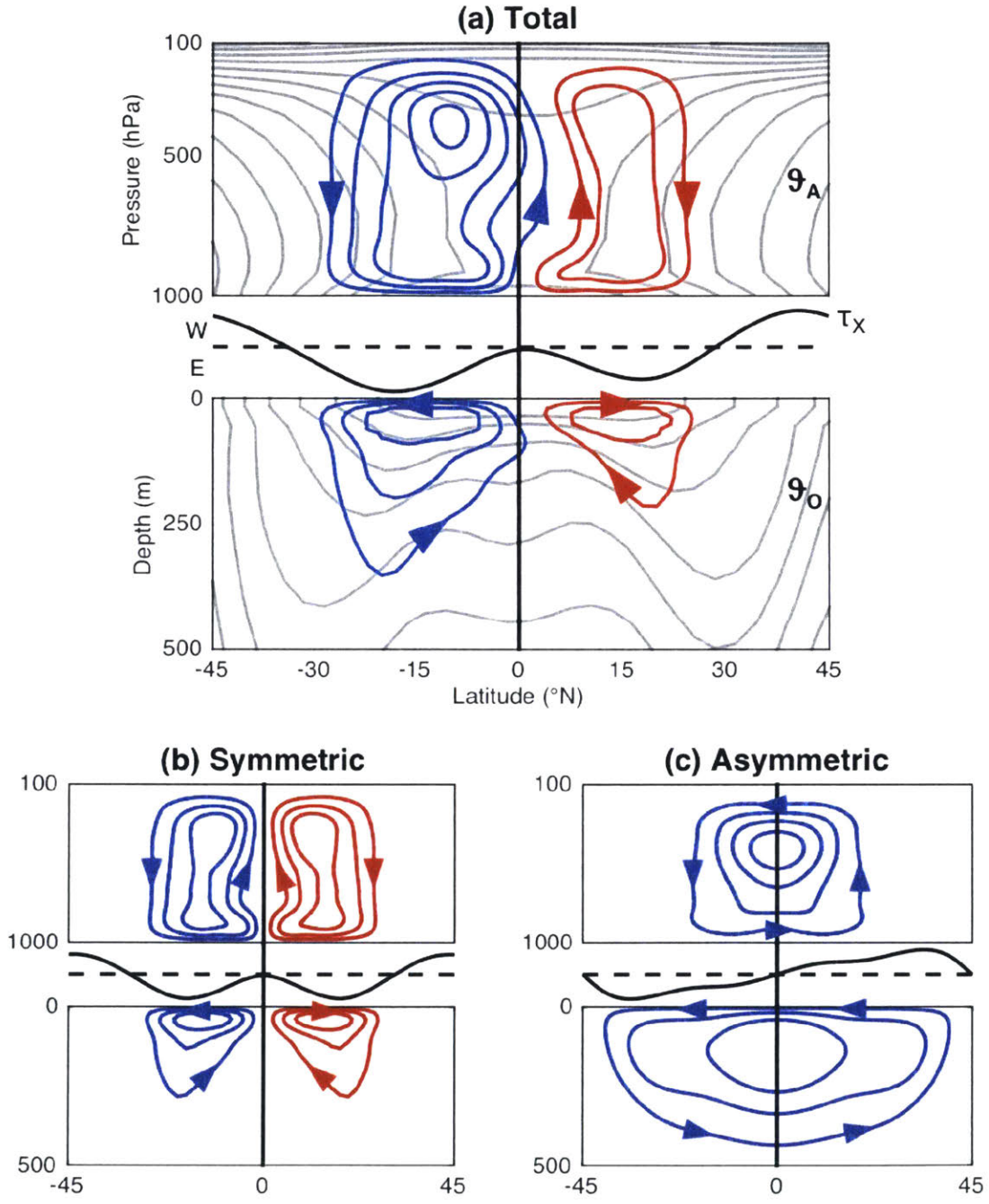

Figure 3.1. Schematic of the atmosphere-ocean circulation. (a): The total atmosphere circulation (top), surface zonal wind stress on the ocean (middle; E indicates easterly and W indicates

westerly), and ocean circulation (bottom). Contours of moist static energy (ϑ_A) and water temperature (ϑ_O) are shown in gray, generally increasing in value upward and equatorward. (b): As in (a), but for the symmetric component of the atmosphere and ocean circulations and the surface zonal wind stress. (c): As in (a), but for the asymmetric component of the atmosphere and ocean circulations and the surface zonal wind stress.

3.2 Model Framework and Experimental Design

We use a coupled atmosphere-ocean version of the MITgcm (Marshall et al. 1997a, 1997b, 2004), run on a cubed-sphere grid with roughly 2.8 ° horizontal resolution (Adcroft et al. 2004). The atmospheric component of the model has 26 pressure levels and employs a gray radiation scheme as in Frierson et al. (2007). The longwave optical thickness is modified by the distribution of water vapor, following Byrne and O'Gorman (2013), but there are no clouds or shortwave absorption in the atmosphere, and the planetary albedo is equal to the surface albedo. Convection and precipitation are parametrized as in Frierson et al. (2007), employing a modified Betts-Miller scheme; unstable regions are relaxed to a moist adiabatic lapse rate. A seasonal cycle of insolation at the top of the atmosphere is specified for a circular orbit with a 360-day period, an obliquity of 23.45 °, and a solar constant of 1360 W m^{-2}. We specify a distribution of surface albedo varying from 0.2 at the equator to 0.6 at the poles (Figure 3.2b) to broadly mimic the observed distribution of albedo.

To test the impact of the ocean circulation on the ITCZ, we run two configurations of the model: one where the ocean's circulation is "active" and one where it is "passive." The "active" oceanic component of the model is similar to Enderton et al. (2009), with 15 vertical levels spanning a depth of 3.4 km, and parametrizes geostrophic eddies using a Gent-McWilliams/Redi

scheme following Griffies (1998). Ocean basins are created by placing infinitesimally wide North-South vertical walls at grid cell edges, blocking the zonal flow from crossing a line of longitude. Here we use two of these walls, spaced 90 ° longitude apart and extending from the North Pole to 35 °S, to create a two-basin "Double Drake" geometry with a large Southern Ocean, as in Ferreira et al. (2010) (Figure 3.2a). The fully coupled model with the "active" ocean is spun up for 1000 years, at which point there are only small temperature trends in the deep ocean, on the order of 0.1K per century.

The atmosphere and ocean circulations in the fully coupled model have features similar to present-day Earth. Hadley cells in the NH and SH extend to roughly 30° latitude (Figure 3.3a), and the average of their annual mean strengths is 80 Sverdrups (Sv, $1\text{Sv} = 10^9\,\text{kg s}^{-1}$), with the NH cell 17 Sv stronger than the SH cell. The surface zonal wind stress on the ocean (Figure 3.3b) is easterly over the width of the Hadley cells, and westerly in the extratropics. The 90 ° wide small basin has a deep overturning circulation qualitatively similar to the AMOC, while the 270 ° wide large basin's circulation is dominated by the shallower subtropical cells and confined to the thermocline, as in the Pacific Ocean (Figure 3.3d, e). The global ocean overturning streamfunction between 45-60 °S shows upwelling in the Southern Ocean of deep water formed in the small basin.

Meridional energy transports in the tropics by the atmosphere and ocean are shown in Figure 3.4a, with both fluids transporting energy across the equator. The ocean's poleward energy transport is dominated by the time mean circulation, and 0.3 PW of energy is transported northward across the equator due to the deep overturning circulation in the small basin. While the time mean, zonal mean Hadley cells in this model accomplish a smaller fraction of the total atmospheric poleward energy transport than in nature (c.f. Marshall et al. 2014 Figure 3), they

are responsible for nearly all of the atmosphere's 0.2 PW of southward cross-equatorial energy transport. Tied to this southward cross-equatorial energy transport, the ITCZ position – calculated as the centroid of zonal mean precipitation between 20 °S and 20 °N following Donohoe et al. (2013) – is in the NH in the annual mean (Figure 3.4b). The relationship between the ITCZ position and the atmosphere's cross-equatorial energy transport can also be diagnosed from monthly means over the model's seasonal cycle, and regressing the latter onto the former yields a slope of 1.8 ° PW^{-1} for monthly mean values. This slope is somewhat lower than the Earth's 2.7 ° PW^{-1} (Donohoe et al. 2013). One possible reason for this is an excess of total tropical rainfall in our model relative to the Earth, making our centroid metric for the ITCZ less sensitive to changes in the tropical rainfall peak. Another is a higher net heating of the atmosphere at the equator in our model relative to the Earth, making the position of the ITCZ less sensitive to energetic perturbations in the "energy flux equator" framework of Schneider et al. (2014); see the discussion in Appendix A2. In the annual mean, the ITCZ resides in the NH, consistent with the stronger SH Hadley cell (Figure 3.3a) and southward cross-equatorial energy transport by the atmosphere (Figure 3.4a).

Results from "active" ocean model runs are compared to those using a "passive" ocean circulation, which consists of a stationary mixed layer heated by a specified pattern of heat fluxes, often termed a "slab" ocean. These heat fluxes are diagnosed from the annual mean net surface heat flux from the spun-up control run of the fully coupled configuration and represent ocean energy transport convergence into a given grid box. Annual mean mixed layer depths at each grid box are diagnosed from the fully coupled runs and applied as a constant boundary condition. To reduce the spin-up time of the model (200 years for the slab ocean configuration), mixed layer depths are limited to 300 m, only affecting the values near the North Pole in the

small basin. The seasonal cycle of mixed layer depths and ocean energy transport in the fully coupled model appear to have a minor impact on the large scale atmospheric circulation in the tropics: the seasonal cycle of the Hadley cells' strengths and the ITCZ position are similar (respective amplitudes of 199 and 205 Sv for the NH Hadley cell and 9.9 and 10.0 degrees latitude for the fully coupled and slab runs) between the slab ocean and fully coupled cases.

Once both model configurations are spun up, shifts in the ITCZ are forced by modifying the distribution of surface albedo (Figure 3.2b), reducing it to 0.5 at the North Pole and increasing it to 0.7 at the South Pole. This has the effect of heating the NH and cooling the SH, and the ITCZ is expected to shift north. Because the atmosphere does not interact with shortwave radiation in our model, all of the resulting heating or cooling initially occurs at the ocean surface. The forcing is applied instantaneously to ten ensemble members from both the fully coupled and slab ocean models, and ensemble members are initialized with snapshots of fields from their control runs taken at ten-year intervals. Ensemble means are composited on the year the forcing is applied. Changes in model fields from the forced runs are differenced from their 300-year averages in the control runs – years 1001-1300 in the fully coupled model, and years 201-500 in the slab ocean model. The adjusted, quasi-equilibrium response to the forcing is taken as the time mean, ensemble mean for years 101-200 after the forcing is applied, during which period trends in the model fields are relatively weak. Since the ocean circulation is free to change in the fully coupled model while its representation in the slab ocean model is fixed, differences in the responses of the two model configurations will serve to highlight the role of an active ocean circulation in affecting the model's response to the albedo forcing.

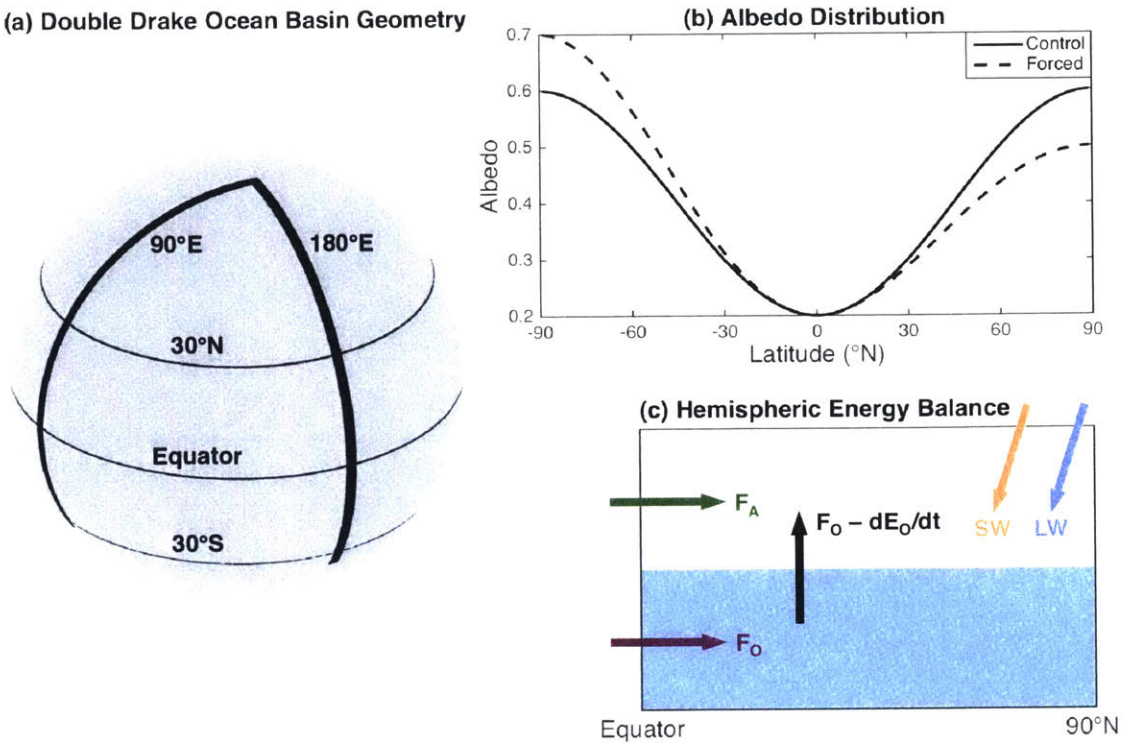

Figure 3.2. Model setup and hemispheric energy balance. (a): Ocean basin geometry, showing the two thin ridges at 90 °E and 180 °E extending from 90 °N to 35 °S, blocking zonal flow in the ocean. (b): Surface albedo distribution for the control (solid line) and forced (dashed line) model runs. (c): Terms in the hemispheric energy balance corresponding to those in Eq. (3.2).

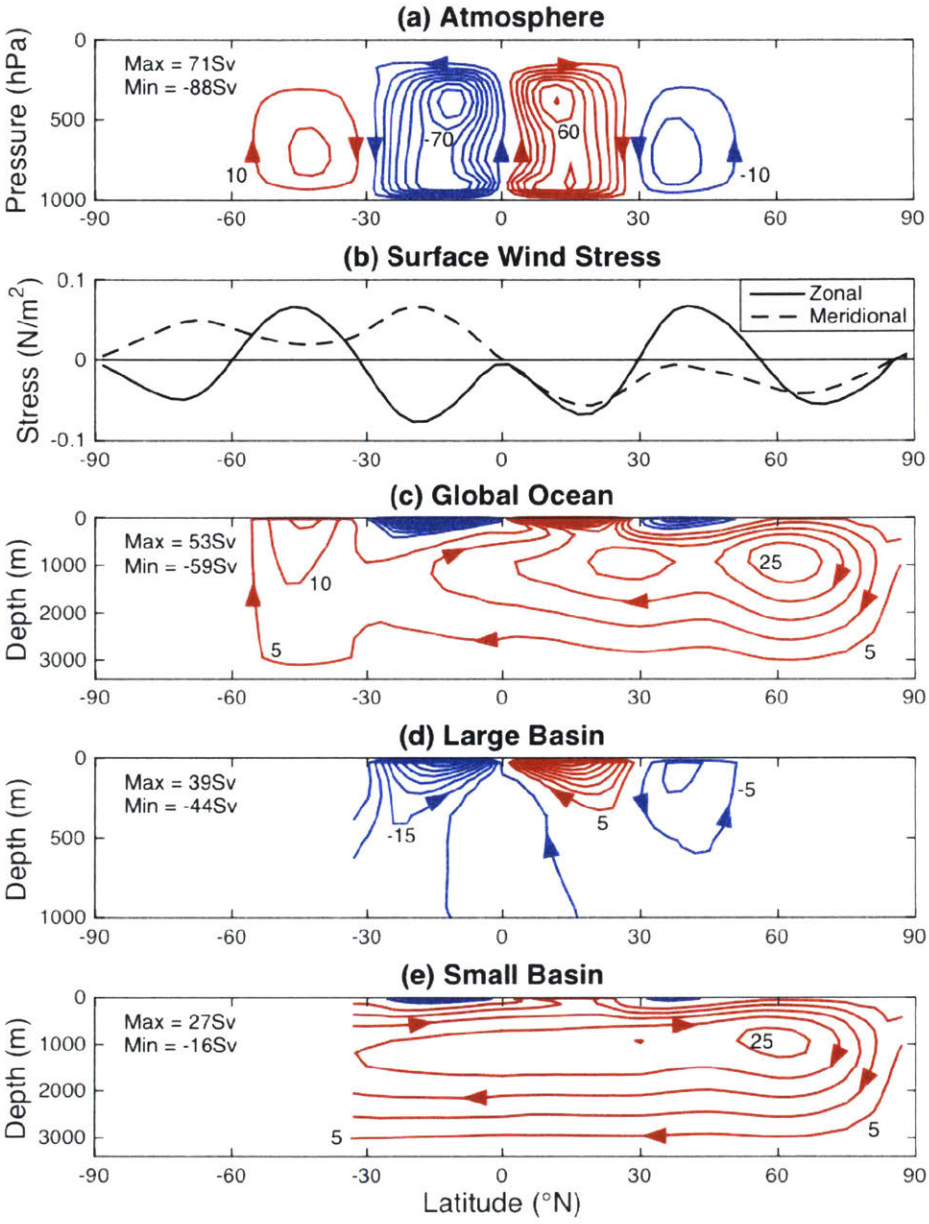

Figure 3.3. Fully coupled model run annual mean overturning circulations in the control simulation. (a, c, d, e): Zonal mean mass transport streamfunctions for the atmosphere (a, countour interval: 10 Sv), global ocean (c, contour interval: 5 Sv), and the large and small ocean

basins (d, e; contour interval: 5 Sv). Red contours indicate positive values and clockwise rotation, and blue contours indicate negative values and counter-clockwise rotation, shown by arrows. The zero contour is not shown. (b): Annual mean zonal (solid line) and meridional (dashed line) surface wind stress on the ocean.

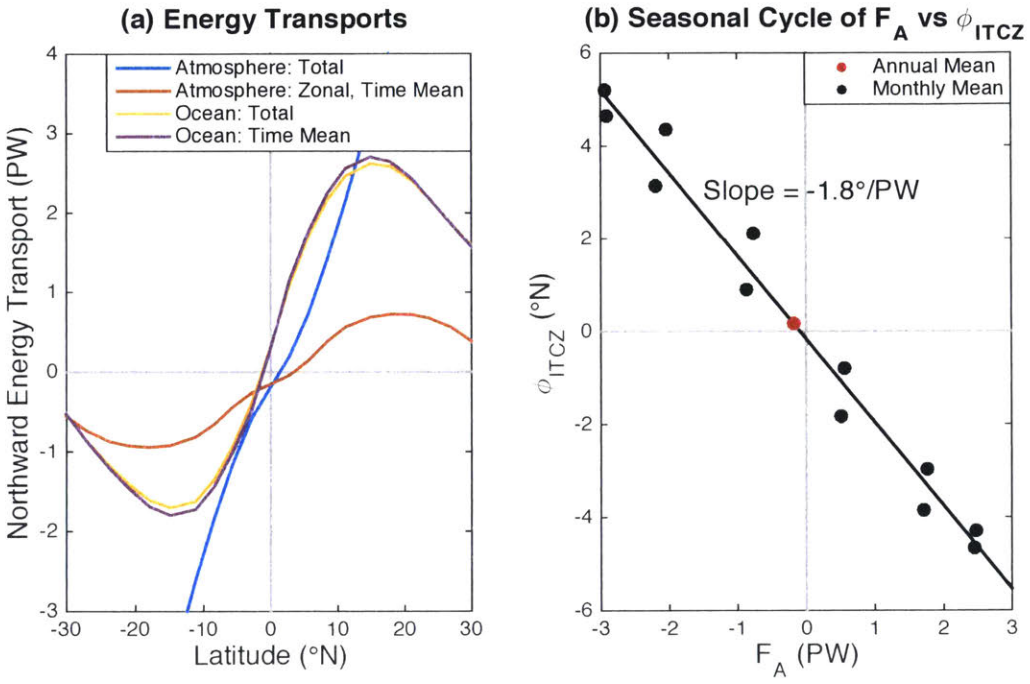

Figure 3.4. Fully coupled model run energy transport climatology. (a): Annual mean northward energy transports in the atmosphere and ocean. (b): Regression of cross-equatorial energy transport by the atmosphere onto the ITCZ position using monthly mean values (black dots) from the control run's seasonal cycle. The red dot is the annual mean ITCZ position and energy transport.

3.3 ITCZ Shifts and the Hemispheric Energy Balance

Fully coupled runs show a significantly reduced ITCZ shift when compared to runs with a slab ocean. Compositing on the year the albedo distribution is changed, the ITCZ's response to the forcing is weaker at all timescales in the fully coupled runs, and the quasi-equilibrated response shows a reduced shift by a factor of 4.30, from 2.44 degrees in the slab runs to 0.57 degrees (black lines, Figure 3.5a). In both the slab and fully coupled runs, the majority of the ITCZ's shift occurs in the first few years after the albedos are changed. This, when combined with the reduced ITCZ shift in the fully coupled runs during those years, suggests a rapid response of the ocean circulation.

In response to the imposed albedo contrast, the ocean circulation acts to damp the ITCZ shift. This damping can be diagnosed using the hemispheric energy budget, where tendencies of the atmosphere's and ocean's energy content, dE_A/dt and dE_O/dt, are equal to changes in the incoming fluxes of energy, shown schematically in Figure 3.2c. The energy budget for the NH is

$$\frac{dE_A}{dt} + \frac{dE_O}{dt} = SW + LW + F_A + F_O \,. \quad (3.2)$$

Here the net incoming energy flux is separated into downward shortwave (SW) and longwave (LW) radiation at the top of the atmosphere, and northward cross-equatorial energy transports by the atmosphere (F_A) and ocean (F_O). The units in Eq. (3.2) are watts; tendencies and radiative fluxes are integrated over the hemisphere. The difference between F_O and dE_O/dt is equal to the net flux of energy upward into the atmosphere at the surface. In our analysis, the contribution of the kinetic energy in both fluids to terms in Eq. (3.2) is neglected, and energy content in the

atmosphere is calculated using the moist enthalpy, equal to the sum of the sensible and latent heats. Energy transport in the atmosphere is calculated as the transport of moist static energy, which is the sum of the moist enthalpy and the potential energy.

After the atmosphere and ocean have adjusted in response to the forcing, in this case *SW*, the tendency terms go to zero. If the relationship between changes in the ITCZ latitude and the atmosphere's cross-equatorial energy transport is linear, following from Figure 3.4b, and given by

$$\Delta\phi_{ITCZ} = -b \cdot F_A \quad (3.3a)$$

where b is a positive constant, Eq. (3.2) can be rearranged to give

$$\Delta\phi_{ITCZ} = b \cdot SW \cdot C \quad (3.3b)$$

where

$$C = \frac{1}{1 + F_O/F_A + LW/F_A}. \quad (3.3c)$$

Here C is the "degree of compensation" by the atmosphere's cross-equatorial energy transport for the imposed forcing *SW*. A value of one means *SW* is perfectly compensated by F_A and the atmosphere transports the entire heating imbalance across the equator. A value of zero means the atmosphere transports no more energy across the equator, the ocean's cross-equatorial energy transport and longwave radiation compensate *SW*, and the ITCZ does not move. Diagnosed from

values of $\Delta\phi_{ITCZ}$ and F_A, the constant b is 1.9 ° PW^{-1} for the slab ocean case and 1.3 ° PW^{-1} for the fully coupled case.

Inspecting the terms in Eq. (3.2) for the slab ocean case, shown by the dashed lines in Figure 3.5b, the atmosphere's cross-equatorial energy transport compensates the shortwave forcing much more strongly than increased outgoing longwave radiation. The NH's slab ocean initially absorbs most of the heating imposed by the albedo reduction, but as its energy content tendency decays to zero, the magnitudes of F_A and LW increase to compensate SW. Unless the atmosphere's longwave radiative feedbacks are positive, destabilizing its response to a heating or cooling, LW will have the same sign as F_A, and LW/F_A will be positive. Averaging over years 101-200, the degree of compensation C for the slab ocean runs is 0.79, similar to values seen in previous experiments with a slab ocean and a tropical-subtropical component of the forcing (c.f. Seo et al. 2014 Figure 3c).

If the ocean circulation is allowed to dynamically adjust, however, the atmosphere is no longer the most strongly compensating component, and cross-equatorial energy transport by the ocean dominates the response in the fully coupled runs (solid lines in Figure 3.5b). Because it is deeper, the ocean's energy content tendency takes longer to decay to zero than in the slab ocean runs. Once it does, F_O emerges as the most strongly compensating term followed by F_A then LW. Compared to the slab ocean case, the atmosphere transports less energy across the equator and C decreases to 0.30. The coupled system, however, transports more energy across the equator than the atmosphere does in the slab ocean case. The fraction of the forcing compensated by longwave radiation to space (blue lines) is reduced in the fully coupled runs, where the addition of an active ocean circulation makes the coupled climate system more efficient at compensating the shortwave forcing.

Returning to Eq. (3.3c), it is clear that cross-equatorial energy transport by the ocean is the largest contributor to the reduced degree of atmospheric compensation in the fully coupled case: LW/F_A is similar for both model configurations (0.27 for the slab ocean and 0.39 for the fully coupled model), but F_O/F_A is 1.98 in the fully coupled case while it is zero in the slab ocean runs. A positive F_O/F_A indicates that the ocean and atmosphere are responding to the albedo forcing by both transporting energy southward across the equator, reducing the fraction of the forcing compensated by the atmosphere in the fully coupled runs. Put another way, if the ocean is able to partially compensate an imposed heating imbalance, the net imbalance the atmosphere experiences is reduced, and ITCZ shifts are damped when the atmosphere does not have to transport as much energy across the equator.

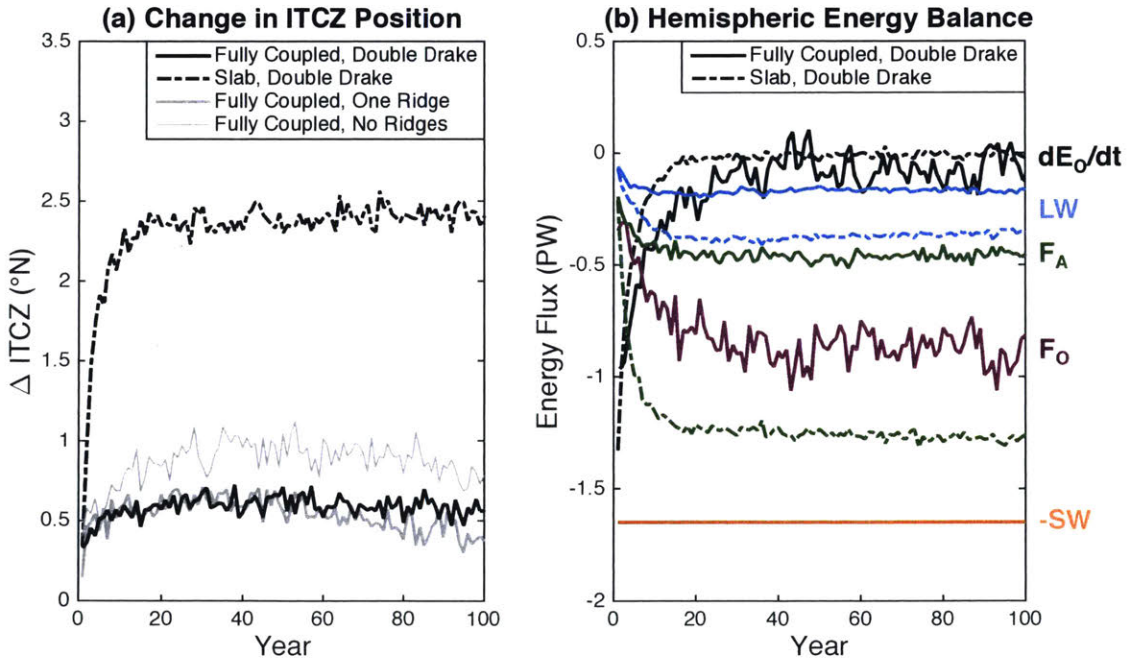

Figure 3.5. Composites of ensemble members beginning the year the albedo distribution is changed for the fully coupled (solid lines) and slab ocean (dashed lines) model runs. (a):

Changes in the latitude of the precipitation centroid. (b): Terms in the Eq. (2) energy budget. Gray lines in (a) indicate ITCZ shifts in fully coupled model runs employing one vertical wall in the ocean at zero longitude extending from the North Pole to the South Pole (One Ridge), or no vertical walls in the ocean to interrupt the flow (No Ridges). Note the atmospheric energy tendency in (b) is not plotted, owing to its small magnitude in the annual mean, and that the sign of the shortwave radiation forcing has been reversed.

3.4 Coupling of the Atmosphere and Ocean Circulations by the Surface Wind Stress

For the ocean to damp ITCZ shifts, it must transport energy across the equator in the same direction as the atmosphere, and the question arises whether that characteristic is robust. It is clear from past modeling studies (see, e.g. Zhang and Delworth 2005, Broccoli et al. 2006) that in some circumstances the opposite can occur. In response to a forced reduction in the strength of the AMOC and its northward energy transport by prescribing a flux of fresh water into the North Atlantic, the atmosphere in those studies shifts the ITCZ southward and transports energy northward across the equator, opposing the ocean's anomalous southward energy transport. However, the shallower STCs are mechanically coupled to the overlying atmosphere through the surface wind stress; their response to forcing will be driven by changes in those winds and could be very different than the AMOC's response to buoyancy forcing in the extratropics. Here we argue that because the STCs are driven by the surface wind stress distribution, they will always transport energy across the equator in the same direction as the atmosphere.

The atmosphere's and ocean's anomalous energy transport in the fully coupled runs are largely achieved by the time mean circulation, which accounts for 69 % of the atmosphere's and

100 % of the ocean's anomalous cross-equatorial energy transport. Anomalous time mean, zonal mean streamfunctions for the atmosphere and ocean, and zonal mean wind stress anomalies are shown in Figure 3.6. Streamfunction anomalies in the atmosphere are stronger than those of the ocean, and peak at about 500 hPa. Large basin ocean mass transport anomalies are strongest in the upper 1000 m, while anomalies in the small basin reflect weakening and shoaling of the deep meridional overturning circulation (MOC). The pattern of zonal wind stress anomalies shows a weakening of the trade winds in the NH and a strengthening in the SH and are consistent with a northward shift of the Hadley cells and the ITCZ. In the extratropics, dipoles of wind stress anomalies reflect a southward shift in the surface westerly jets.

The pattern of zonal wind stress anomalies is asymmetric about the equator, driving southward surface Ekman flow in the tropical ocean in both hemispheres (Figure 3.7). South of 12 °N, the maximum anomaly in the global ocean's anomalous mass transport streamfunction is equal to the Ekman mass flux times the circumference of a latitude circle, defined as

$$M_{Ek} = 2\pi a \cdot cos\phi \cdot \frac{\tau_X}{f} \quad (3.4)$$

where a is the radius of the Earth, τ_X is the zonal mean zonal wind stress at the surface, and f is the Coriolis parameter. North of 12 °N, changes in the small basin's deep MOC are stronger than the Ekman mass transport anomalies. The deep MOC, with mass transport streamfunction anomalies shown in Figure 3.6c peaking at a depth near 2000 m, is not expected to be in Ekman balance with the surface wind stress. When streamfunction anomalies are evaluated near a depth of 150 m, though, they match the Ekman mass transport.

Even though Ekman balance breaks down near the equator, the near-linearity of the zonal wind stress anomalies there (Figure 3.6b) does not drive strong Ekman suction or pumping, and the surface flow crosses the equator (as in Miyama et al. 2003). The anomalous Ekman mass transports plotted in Figure 3.7 are relatively well behaved near the equator because the zonal wind stress anomalies approach zero faster than the Coriolis parameter does. The resulting anomalous cross-equatorial cell, or CEC, is seen most clearly in the large basin (Figure 3.6d), where Ekman pumping and suction close the circulation at roughly 40 °S and 40 °N. Southward shifts in the surface westerly jets are responsible for anomalies in extratropical Ekman pumping and suction. The meridional extent of the CEC is set by the distance between the westerly wind maxima in each hemisphere and is significantly larger than the extent of the Hadley cells. While the CEC shares a surface branch with the STCs, it is distinct from them. Comparing Figure 3.6d to Figure 3.3d, note that upwelling branch of the STCs is not moved off of the equator, and that the return branch of the CEC is deeper than the subsurface flow of the STCs.

Anomalies in the atmosphere's mass transport streamfunction (Figure 3.6a) peak in the mid-troposphere and are not in Ekman balance with the surface winds equatorward of 15 degrees (Figure 3.7). Their vertical structure is similar to the climatological Hadley cells, though – compare Figure 3.6a to 3.3a – and indicative of a shift in those circulations. Streamfunction anomalies evaluated near the top of the planetary boundary layer at 900 hPa are same-signed as those above, and are in Ekman balance with the surface wind stress to within six degrees of the equator. This relationship also holds over the seasonal cycle in the control run, indicating that while peak Hadley cell anomalies are not in Ekman balance with the surface zonal wind stress, they are coupled to it.

The mass and energy transports of the overturning circulations in both fluids are related by their gross stabilities (Neelin and Held 1987, Held 2001), a measure of the energy contrast between their upper and lower branches. We may write, following Czaja and Marshall (2006) and Held (2001):

$$\frac{F_O}{F_A} = \frac{\psi_O}{\psi_A} \cdot \frac{S_O}{S_A}. \quad (3.5)$$

Gross stabilities S_O and S_A represent the respective energy contrasts between the upper and lower branches of the ocean and atmosphere circulations. Anomalous energy transports by the atmosphere and ocean are shown in Figure 3.7b. As mentioned in Section 3.3, the ocean transports nearly twice as much energy across the equator as the atmosphere, diverging more energy from the NH subtropics and converging it in the SH subtropics. The atmosphere diverges or converges more energy in the extratropical and polar latitudes, primarily through transient eddies and stationary waves rather than the zonal mean, time mean circulation. Near the equator, the atmosphere's southwards energy transport decreases, and the zonal mean, time mean Hadley cells are responsible for the majority of the cross-equatorial transport.

Guided by Eq. (3.5) and dividing anomalous cross-equatorial energy transports by peak mass transport streamfunction anomalies at the equator, the gross stability of the atmosphere is 1.3×10^4 J kg^{-1} and the ocean is 6.3×10^4 J kg^{-1}. The relatively high gross stability in the ocean is expected, since the specific heat capacity of water is larger than that of air, and the tropical thermocline is in general more stratified in temperature than the tropical atmosphere is in moist static energy. So, even though the atmosphere's anomalous circulation is stronger, the ocean transports more energy across the equator. Combining the positive gross stabilities of both fluids

with the constraint that their circulations must overturn in the same sense by Ekman balance, making ψ_O/ψ_A positive, F_O/F_A is positive from Eq. (3.5) and the atmosphere and wind-driven CEC are constrained to transport energy across the equator in the same direction. This coupled cross-equatorial energy transport results in the damping of ITCZ shifts described by Eq. (3.3b, c).

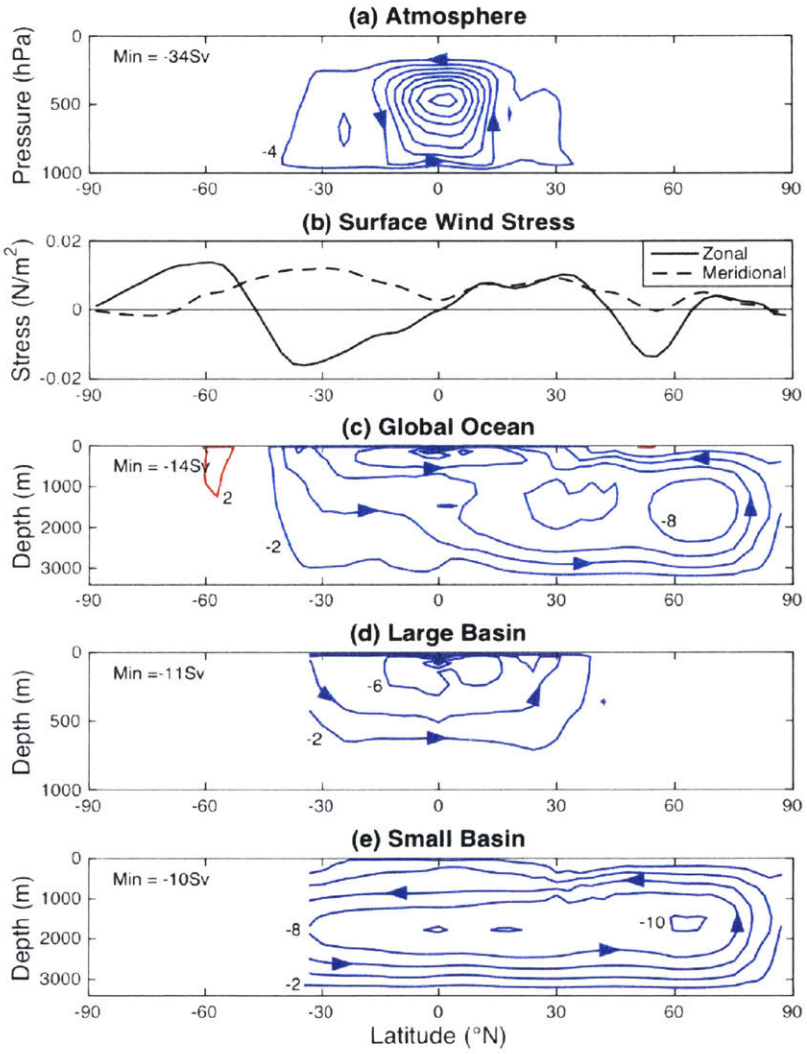

Figure 3.6. As in Figure 3.3, but for annual mean anomalies in the fully coupled runs, ensemble-averaged over years 101-200 after the albedo distribution is changed. Contour interval in (a): 4 Sv. Contour interval in (c,d,e): 2 Sv.

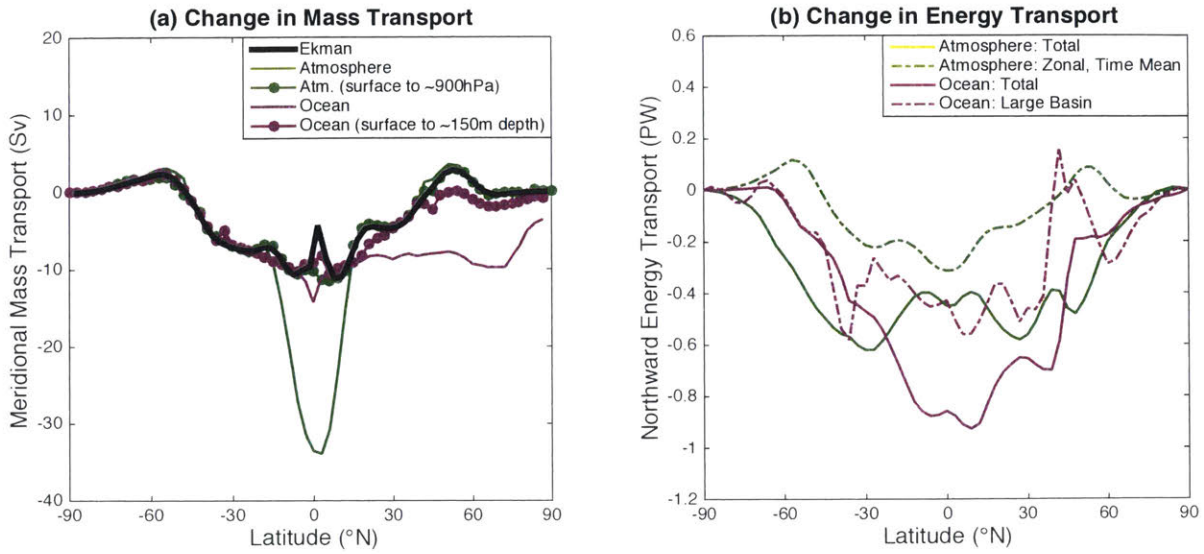

Figure 3.7. Mass and energy transport anomalies in the fully coupled model runs. (a): Black line: anomalous Ekman mass transport. Solid color lines: maximum mass transport streamfunction anomalies at each latitude. Lines with dots: mass transport streamfunction anomalies in the atmosphere at the 891 hPa model level (green) and at the 144 m depth model level in the ocean (purple). (b): Anomalous northward energy transports by the atmosphere and ocean.

3.5 Large Basin Cross-Equatorial Cell and Energy Transport

We have shown that the cross-equatorial cell's mass transport is in Ekman balance with the surface wind stress, but its cross-equatorial energy transport is also sensitive to its gross stability, which is set by the properties of the surface and return branches. In this section, we describe the properties and paths of these two branches, how they impact the energy transported by the CEC, and draw comparisons to the annual mean circulation in the Indian Ocean. Our focus will be on the circulation in the large basin, which is responsible for 46 % of the ocean's total cross-equatorial energy transport (Figure 3.7b). The anomalous circulation in the large basin is

shallower and more clearly wind-driven than that of the small basin (compare Figure 3.6d to 3.6e), where changes in the STCs can be difficult to separate from the large changes in the deep MOC.

Transforming the vertical coordinate from depth to temperature, the anomalous mass transport streamfunction in the large basin, including transport by both the steady and unsteady circulation, is shown in Figure 3.8. The warmer upper branch roughly follows zonal mean surface conditions, while the denser, colder lower branch conserves temperature as it flows northward across the equator. The temperatures in the lower branch are nearly identical to the seasonal minimum surface temperature – calculated as the average minimum monthly mean surface temperature from the forced runs – at their source latitudes near 40 °S, reflecting the Ekman pumping of water caused by the southward shift in the SH westerly jet. The southward cross-equatorial energy transport accomplished by this circulation is 0.41 PW, which when divided by its strength at the equator, 7.2 Sv, gives a gross stability of 5.9×10^4 J kg^{-1}, close to the value estimated above for the global time mean, zonal mean CEC. Dividing by the specific heat capacity of 3994 J kg^{-1} K^{-1} gives a temperature contrast between the upper and lower branches of 14 °C, close to the 15 °C difference between the -4 Sv contours at the equator in Figure 3.8.

This temperature contrast between the upper and lower branches is set by the SST difference between the tropics and extratropics. Ekman pumping, feeding the return branch of the CEC, is strongest near 40°S where the annual mean SST is 14 °C, 15 °C cooler than the equator. The water in the return branch is a couple degrees cooler than the annual mean SST at 40 °S, though, as it is formed during wintertime. Temperatures in the surface branch at the equator are also a couple degrees cooler than the annual mean SST there, offsetting the amplitude of the seasonal cycle of SST around 40 °S. As a result, the gross stability of the CEC

is approximately the annual mean SST difference between the equator and the extratropics, in this case 40 °S.

The pathways of the upper and lower branches are shown in Figure 3.9, where anomalous currents are displayed at the surface and on the 1026.5 kg m^{-3} potential density surface, a typical value for the lower branch flow. The surface currents forming the upper branch of the CEC diverge near 40 °N, cross the equator in the interior of the basin, and converge near 40 °S. On the 1026.5 kg m^{-3} potential density surface, water subducted near 40 °S travels westward and hits the Western boundary at 20-40 °S. The flow then bifurcates; some recirculates southward and the rest travels northward across the equator in a boundary current. This boundary current, integrated over 6-16 °C (corresponding to 240-930 m depth at the equator on the Western boundary) and 174-180 °W transports 7.8 Sv, close to the 7.2 Sv strength of the CEC at the equator in Figure 3.8.

The anomalous cross-equatorial cell we see in these simulations is reminiscent of the Indian Ocean's shallow overturning circulation. While it has a strong seasonal cycle, the annual mean Indian Ocean CEC is also characterized by cross-equatorial wind-driven flow near the surface and return flow in a deeper western boundary current (Schott et al. 2002), transporting an estimated 0.5 PW of energy southward across the equator (Trenberth and Caron 2001). Annual mean surface zonal wind stress in the Indian Ocean is nearly asymmetric about the equator, and Ekman transports are southward in the interior of the basin at both 3 °N and 3 °S. Like the anomalous CEC seen in our simulations, the annual mean Indian Ocean CEC returns this cross-equatorial mass transport in a deeper western boundary current, the Somali current, whose water eventually upwells in the Northern Hemisphere.

The Indian Ocean, however, has a counter-rotating "equatorial roll" under which the surface Ekman currents pass to cross the equator. The equatorial roll in observations is 50-100 m deep and only a couple degrees latitude wide, too narrow to be simulated in our model, and is not seen in Figure 3.6d. We do, however, notice near the equator a weakening of surface currents in Figure 3.9a and a dip to temperatures lower than zonal mean surface values of the surface branch in Figure 3.8. Near the equator, the surface branch is confined to the first model level, but in the grid cells immediately surrounding the equator, the southward flow spreads to the second model level (not shown) and slightly cooler temperatures. Because of its shallow depth, the Indian Ocean equatorial roll resides mostly in the weakly stratified mixed layer and does not significantly contribute to cross-equatorial energy transport in the Indian Ocean (Schott et al. 2002, Miyama et al. 2003). From the perspective of its cross-equatorial energy transport, then, the Indian Ocean CEC is an analogue of our anomalous CEC, with warm water moving southward near the surface and cooler water subducted by Ekman pumping returning northward in a western boundary current in the thermocline.

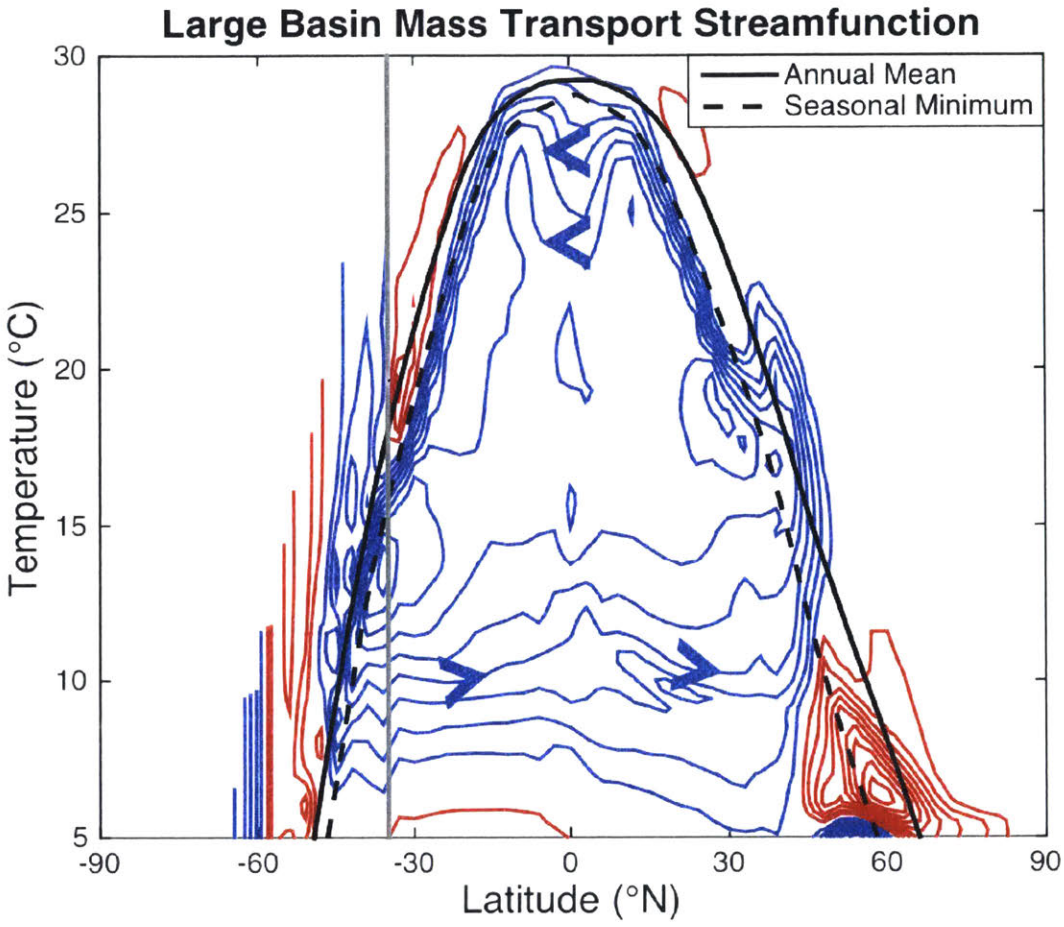

Figure 3.8. Mass transport streamfunction anomalies in the large basin, including the contributions from steady and unsteady transport. Contour interval: 1 Sv, and the zero contour is not shown. Red contours indicate positive values and clockwise rotation, and blue contours indicate negative values and counter-clockwise rotation, shown by chevrons. Black lines: zonal mean surface temperature in the large basin from the forced runs in the annual mean (solid) and the minimum monthly mean value calculated from the average seasonal cycle (dashed).

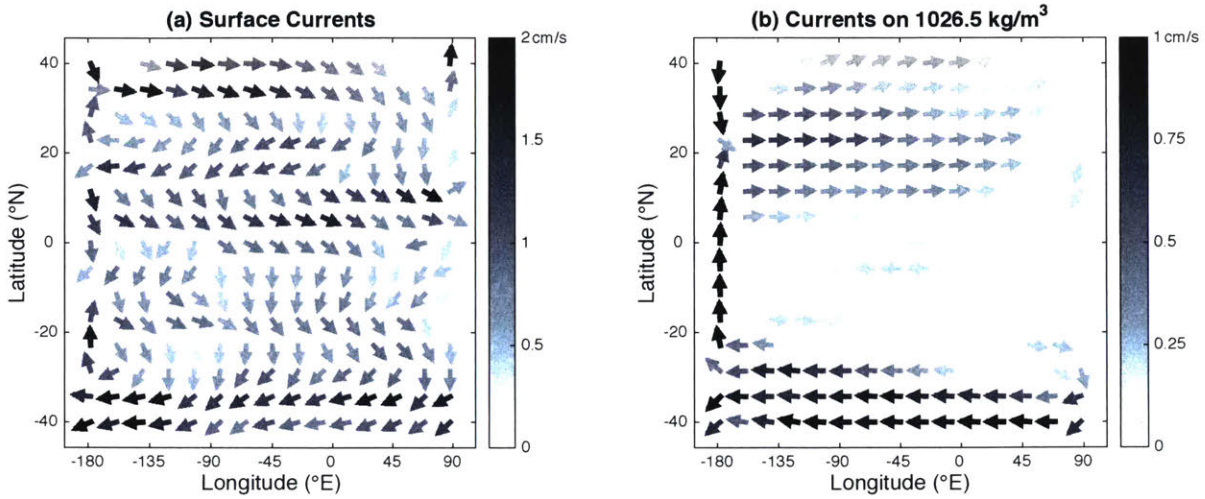

Figure 3.9. Pathways of anomalous cross-equatorial cell currents in the large basin. (a): Surface branch. (b): Return branch. Current speed is shown by shading, and direction is shown by arrows.

3.6 Summary and Discussion

By forcing a coupled ocean-atmosphere model with an inter-hemispheric albedo contrast and allowing the ocean circulation to adjust, we find that the resulting ITCZ shift is damped by a factor of four compared to a configuration where the ocean circulation is held fixed. The adjusted ocean circulation transports energy from the heated hemisphere to the cooled one, and its resulting cross-equatorial energy transport is the largest term in the atmosphere's adjusted hemispheric energy balance, helping offset the heating contrast imposed by the albedo distribution. As a result, the atmosphere is not required to transport as much energy across the equator than if the ocean circulation is held fixed. It therefore does not compensate for the heating contrast as strongly as when coupled to a slab ocean, and so the magnitude of the ITCZ shift is reduced. Key to this reduction is the anomalous ocean circulation acting to transport

energy across the equator in the same direction as the atmosphere, reducing the atmosphere's hemispheric heating imbalance.

We argue that the mechanical coupling between the Hadley cells, surface wind stress, and the tropical-subtropical ocean circulation ensures that that ocean circulation always acts to transport energy across the equator in the same direction as the atmosphere. This is accomplished by an Ekman-driven cross-equatorial cell, or CEC. The strength of the CEC is set by inter-hemispheric asymmetries in the trade winds. Its energy contrast is determined by the SST difference between the tropics and the extratropics, where the shift in the surface westerly jet sets the temperature of the subducted water forming its lower branch. By acting on a larger energy contrast than the Hadley cells, the CEC is more efficient at transporting energy across the equator than the atmosphere, and it transports more energy across the equator even though it is a weaker circulation.

The CEC is a hemispherically asymmetric circulation, and thus can be separated from the symmetric STCs by decomposing the mass transport streamfunction into symmetric and asymmetric components as in Figure 3.1. This decomposition ensures that the symmetric circulation, shown schematically in Figure 3.1b, is largely responsible for energy transport out of the tropics to higher latitudes, but not across the equator since its strength goes to zero there. The hemispherically asymmetric circulation in Figure 3.1c then represents the component that transports energy across the equator, enabling the ocean to compensate for inter-hemispheric heating asymmetries. Comparing Figure 3.1b to 3.1c, the hemispherically asymmetric CEC extends deeper than the symmetric STCs, and transports energy southward across the equator owing to its positive gross stability. The deeper CEC, whose lower water is subducted in the

cooler extratropics, then wraps around the shallower STCs, whose lower branch waters are subducted in the warmer subtropics.

The CEC in our simulations has characteristics reminiscent of the annual mean Indian Ocean circulation, with its surface branch crossing the equator in the interior of the basin and its lower branch crossing the equator in a western boundary current. Returning to Figure 3.5, though, the details of ocean basin geometry and the pathway of the lower branch appear to have a secondary effect. The two solid gray lines show ITCZ shifts from fully coupled simulations where, instead of a "Double Drake" ocean basin geometry, the model's ocean either has a single vertical wall (One Ridge) extending from the North Pole to the South Pole or no wall at all (No Ridges). In all three cases, the ITCZ shift is significantly reduced as compared to slab ocean runs, even when no western boundary current can form as in the no-wall case. The ITCZ shift timescale changes with ocean basin geometry, and its amplitude varies by a couple tenths of a degree across the cases, but the consistent damping of the shift by a fully coupled ocean circulation suggests the details of the ocean basin geometry are unimportant to leading order.

We believe that our key result – the ocean acting to damp ITCZ shifts – is insensitive to the choice of forcing, owing to the mechanical coupling of the atmosphere and ocean circulations by the surface wind stress. For example, if a large freshwater pulse floods an ocean basin containing a deep overturning circulation such as the AMOC, reducing its strength and northward energy transport as in Zhang and Delworth (2005), we can expect the resulting ITCZ shift to induce a wind-driven CEC that transports energy northward across the equator in the same sense as the overlying atmosphere. The CEC's northward energy transport would then oppose the deep circulation's anomalous southward energy transport, offsetting a large fraction of the inter-hemispheric heating experienced by the atmosphere and damping the ITCZ shift.

Furthermore, our results are not affected by the slope of the ITCZ position and atmospheric cross-equatorial energy transport relationship. While our model's slope of -1.8 ° PW^{-1} (Figure 3.4b) is shallower than it is for the Earth, the factor of four damping of ITCZ shifts by the ocean circulation is insensitive to the slope because it reflects the relative magnitudes of the shifts, not their absolute values (see Appendix A2).

Damping of ITCZ shifts by a wind-driven CEC may help explain some of the recent results seen in more comprehensive coupled atmosphere-ocean GCMs. In both Kay et al. (2016) and Tomas et al. (2016), ITCZ shifts are strongly damped in fully coupled models compared to slab ocean models, and anomalous cross-equatorial energy transport is dominated by the ocean in those papers and in Hawcroft et al. (2016). The hemispherically asymmetric pattern of trade wind anomalies in the Pacific in Tomas et al. (2016), their Figure 6a, would drive a southward cross-equatorial surface flow, constituting the surface branch of a CEC as described here. Isolating the asymmetric streamfunction anomalies would help identify if such circulation exists in their model. In Kay et al. (2016), the trade winds in the SH strengthen in all basins relative to the NH, and their hemispherically asymmetric component would drive a CEC in the thermocline hinted at in their Figure 10. Perhaps the clearest indication of a wind-driven CEC in a fully coupled GCM can be seen in Hawcroft et al. (2016), their Figure 7, where changes in the cross-equatorial energy transport by the ocean are dominated by the Pacific Ocean, which does not have a deep overturning circulation like the Atlantic. Combined with the relative increase of the trade winds in the SH (their Figure 3b-e), their results strongly hint at a large cross-equatorial energy transport (0.2-0.3 PW) by a wind-driven CEC.

Of course, our model simulations are for an idealized, water-covered planet, and several differences between our model configuration and the Earth would likely have some impact on

the efficacy of the CEC to compensate an inter-hemispheric heating contrast. Aside from the obvious reduction in surface area covered by the ocean, a significant fraction of the Earth's annual mean cross-equatorial mass transport associated with the Hadley cell occurs in the Somali jet (Heaviside and Czaja 2013). The wind stress resulting from such a concentrated atmospheric current might not drive the kind of oceanic CEC we see here. Additionally, the gross stability of the CEC in our simulations is set by Ekman pumping in the SH extratropics resulting from a southward shift in the surface westerly jet. If a different choice of forcing results in no shift of the surface westerly jet, the gross stability of the CEC would be reduced because its lower branch would be supplied by warmer water subducted in the subtropics. The CEC would then transport less energy across the equator, reducing its capacity to compensate the heating contrast and damp the ITCZ shift.

In summary, our results indicate that the ITCZ's position might be far less sensitive to inter-hemispheric heating contrasts than previously thought, and that the wind-driven ocean circulation can strongly compensate for such forcings. As an example, the Earth's ITCZ position and atmospheric cross-equatorial energy transport are related by a slope of roughly 2.7 ° PW^{-1} (Donohoe et al. 2013). For a degree of compensation of 80 % – appropriate if the ocean circulation is held fixed and F_O is set to zero in Eq. (3.3c) – the ITCZ would shift by 5 ° for 2.3 PW of forcing (Eq. 3.3b). If the ocean's cross-equatorial energy transport is not fixed and this sensitivity is reduced by a factor of four as a consequence of that transport, then a forcing of 9.1 PW is required to induce the same 5 ° ITCZ shift. This is equivalent to a massive 36 W m^{-2} heating over an entire hemisphere. In other words, to induce a northward ITCZ shift of 5 °, the SH's mean albedo would have to be increased by roughly 0.1, equivalent to covering an otherwise bare ocean surface with sea ice poleward of 30 °S! Such a back-of-the-envelope

calculation almost certainly overestimates the forcing necessary to realize a 5° ITCZ shift, but serves to highlight the dramatic changes in hemisphere mean climate necessary to move the global ITCZ more than a couple degrees off of the equator.

Chapter 4

The 'Sticky' ITCZ: Ocean-Moderated ITCZ Shifts

Across a range of simulations with a coupled atmosphere-ocean climate model, shifts in the Intertropical Convergence Zone (ITCZ) are induced by an interhemispheric heating contrast. The response to heating anomalies which are polar amplified are contrasted with those which are largest in the tropics. First, we find that ITCZ shifts are always damped relative to simulations in which the ocean circulation is held fixed, irrespective of the heating distribution, keeping the ITCZ "stuck" to latitudes near the equator. The damping is primarily due to the ocean's anomalous cross-equatorial energy transport associated with the coupling of the trade winds to an oceanic cross-equatorial cell (CEC). Second, we find that the damping effect is strongest when the forcing distribution is polar-amplified, which maximizes the efficiency of the CEC's cross-equatorial energy transport. Third, we argue that the ocean's energy transport can have secondary impacts on ITCZ shifts through its interaction with climate feedbacks. Finally, we discuss the implications of our study for our understanding of the role of CECs in damping ITCZ shifts in the present climate, estimating that a CEC could damp ITCZ shifts by a factor of two.

4.1. Introduction

Earth's northern hemisphere (NH) is slightly warmer than the southern (SH; Feulner et al. 2013) and its climatic equator is slightly north of the geographical equator. Interestingly, the hemispheric albedos are almost identical to one another and so the solar radiation absorbed in

each hemisphere is, to within measurement accuracy, the same: the NH is warm because of cross-equatorial heat transport in the Atlantic sector of a few tenths of a petawatt (10^{15} W; see the discussion in Marshall et al. 2014). But imagine a climate in which the hemispheric albedos were very different, demanding that the coupled atmosphere-ocean system transport large amounts – perhaps many petawatts – of energy across the equator. How would the coupled system achieve this? What would be the relative roles of the atmosphere and ocean in the balancing process? Would the partitioning of the energy transport between atmosphere and ocean be sensitive to whether the heating anomaly were polar- or equatorially-magnified?

Recently, several experiments using comprehensive global climate models (GCMs) forced with interhemispheric heating contrasts have pointed to a role for the tropical ocean circulation in moderating shifts of tropical rainfall patterns and the climatic equator. Known as the intertropical convergence zone, or ITCZ, the tropical rainfall maximum is collocated with the ascending branch of the atmosphere's Hadley cells, shifting with those circulations into the hemisphere heated most strongly by radiation and surface heat fluxes (see the review in Schneider et al. 2014). Compared to runs without an active ocean circulation, the tropical precipitation response to SH cooling by brightened clouds (Kay et al. 2016) and NH heating by Arctic sea ice loss (Tomas et al. 2016) is strongly muted in fully coupled atmosphere-ocean simulations. In both cases, the ocean circulation's cross-equatorial energy transport is responsible for offsetting a large fraction of the imposed heating contrast. If the ocean's response is decomposed into contributions from each basin, the Pacific Ocean, whose subtropical cells (STCs) are responsible for the majority of the basin's meridional energy transport in the tropics (Ferrari and Ferreira 2011), can be the largest contributor to the global response (Hawcroft et al. 2016).

Coupled to the Hadley cells above by the trade winds, the STCs are capable of transporting more energy in the tropics than their atmospheric counterparts (Held 2001, Czaja and Marshall, 2006) because they act on the highly stratified tropical ocean. In idealized GCM simulations of a water-covered Earth, experiments with a coupled atmosphere-ocean model (Green and Marshall 2017; hereafter GM17) and an atmospheric model coupled to a stationary slab ocean modified to simulate the STCs (Kang et al. 2018) have shown that the STCs and their associated CEC act to damp ITCZ shifts. The experiments in GM17 highlighted the basic mechanism behind the damping of ITCZ shifts by the STCs, shown schematically in Figure 4.1: the coupling to the atmosphere above by the trade winds generates an anomalous cross-equatorial cell (CEC) whenever the ITCZ shifts off of the equator. Driven by the anomalous cross-equatorial Hadley cell above, the oceanic CEC is capable of transporting more energy across the equator owing to its higher heat capacity and vertical temperature contrast. It is this cross-equatorial energy transport by the CEC, acting to offset the interhemispheric heating contrast, that reduces the amount of energy the Hadley cells must transport across the equator and damps the ITCZ shift. Using a simple energy balance framework, GM17 then showed how the cross-equatorial energy transport by the CEC can damp ITCZ shifts by a factor of four.

Here we further explore the damping of ITCZ shifts through their coupling to the tropical ocean circulation, attempting to induce extreme shifts by varying the magnitude of the interhemispheric heating contrast and its meridional distribution, using the same model as in GM17. We find that cross-equatorial energy transport by the CECs always acts to damp ITCZ shifts but the degree of damping depends on whether the heating profile reaches a maximum at poleward as opposed to equatorward latitudes. To a lesser extent, the degree of damping also depends on the interaction between the ocean's heat transport and radiative feedbacks. Finally,

we discuss the implications of our study for ITCZ shifts in the current climate and interpret our results in the context of an energy balance model proposed by Schneider (2017).

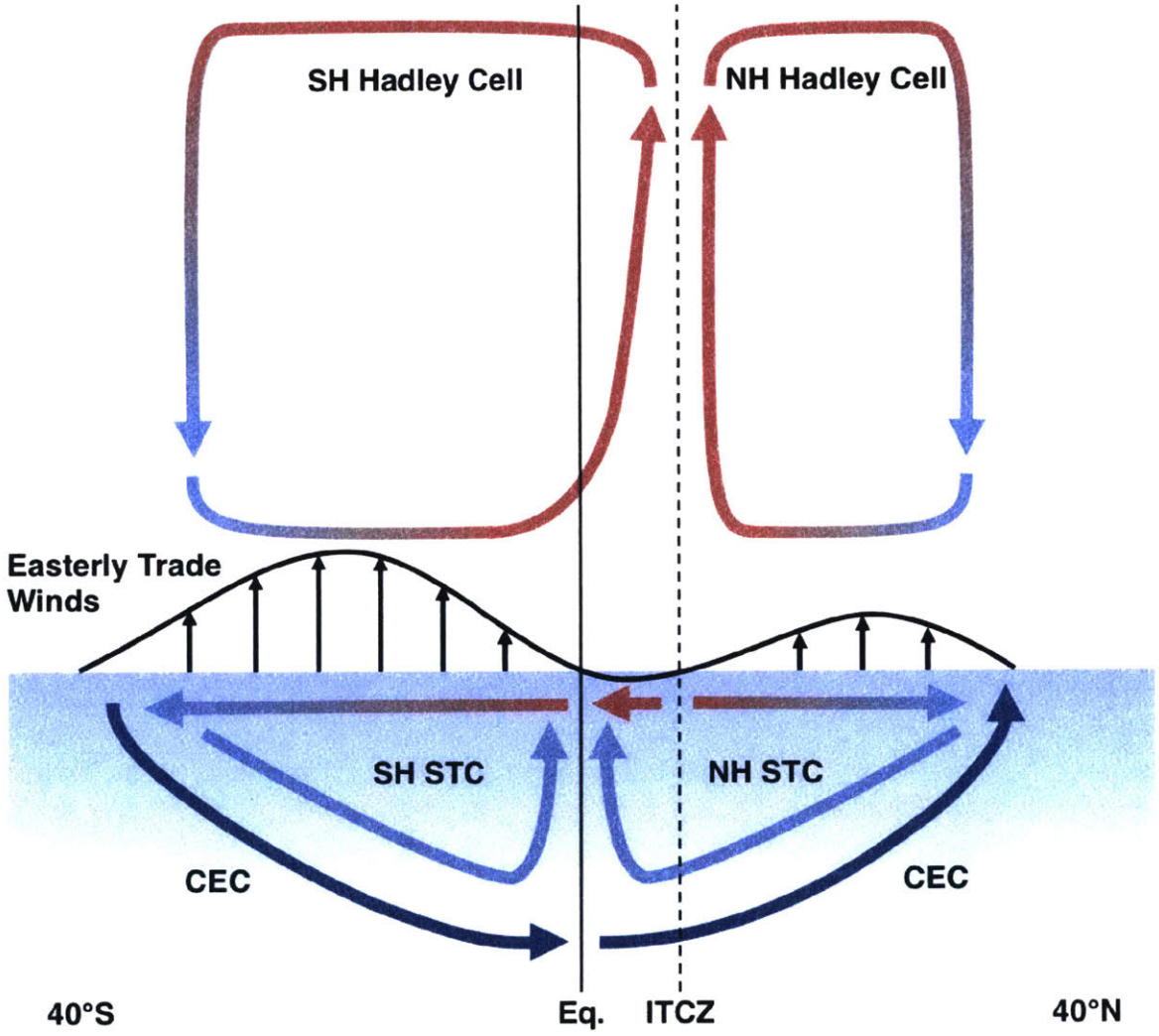

Figure 4.1. Schematic of the atmosphere and wind-driven tropical ocean circulations for a northward ITCZ shift. In the atmosphere, the colors of the arrows are meant to represent the moist static energy content of the air circulating in the Hadley cells. In the ocean, the colors represent the temperature of the water masses forming the STCs and the CEC. The equator and the latitude of the ITCZ are indicated with solid and dashed vertical black lines, respectively.

4.2. Model Configuration and Design of Experiments

We use the same model described in GM17, a coupled atmosphere-ocean version of the MITgcm (Marshall et al. 1997a, b, 2004) in configurations with and without an active ocean circulation. Both the atmospheric and oceanic components are run on a cubed-sphere grid with roughly 2.8 ° horizontal resolution in the tropics (Adcroft et al. 2004). The atmospheric component has 26 pressure levels, moist physics and a gray radiation scheme as in Frierson (2007), and includes a water vapor feedback on the longwave optical thickness as in Byrne and O'Gorman (2013). There are no clouds or shortwave absorption in the atmosphere, making the planetary albedo equal to the surface albedo, which we prescribe to be symmetric about the equator (Figure 4.2a). The model is run with a seasonal cycle of insolation for a circular orbit with an obliquity of 23.45 °.

The oceanic component of the model is also identical to GM17 and run in a configuration both with and without an active ocean circulation. In the active case, the ocean and its circulation are fully coupled to the atmosphere above; there are 15 vertical levels down to a depth of 3400 m. Two infinitesimally thin ridges, running from the North Pole to 35 °S, are spaced 90 ° longitude apart, creating a small 90 °-wide basin, a large 270 °-wide basin, and a circumpolar southern ocean. As described in Ferreira et al. (2010), this leads to localization of deep water formation and sinking in the polar latitudes of the small basin, and wind-driven circumpolar upwelling around the south pole, mimicking the global overturning cell of Earth's current climate. In the passive ocean circulation case, referred to as a "slab" ocean, the model has one stationary layer with specified patterns of depth and ocean heat transport convergence that match the annual mean from the fully coupled configuration's control run. Setting up the slab ocean configuration in this way allows us to attribute differences between its response and the fully

coupled configuration's response to the forcing described below to the adjustment of the ocean circulation in the fully coupled case.

The control runs of both the slab ocean and fully coupled models are very similar to each other, and identical to those in GM17. Shown in Figure 4.3a, the fully coupled control run's annual mean atmospheric circulation is qualitatively similar to the Earth's, with a SH Hadley cell that is stronger (88 Sv) than the NH Hadley cell (71 Sv). Surface easterly trade winds (Figure 4.3b) and the STC in the large basin (Figure 4.3c) are correspondingly stronger in the SH: 3.0 m s^{-1} and 45 Sv versus 2.7 m s^{-1} and 39 Sv in the NH. Sea surface temperatures (SSTs) are slightly higher in the NH than the SH and peak at 29 °C at the equator; their hemispheric means are 19 and 17 °C, respectively. It should be noted that the model does not form sea ice, resulting in polar SSTs that are below freezing, in which case the model calculates the density of seawater by extrapolating the curves for its equation of state (Jackett and McDougall, 1995) below the freezing point. The hemispheric asymmetries of Hadley cell and trade wind strengths, and of SST, are the result of a deep overturning circulation in the small basin that transports heat northward across the equator, as described in Ferreira et al. (2010) and shown in Figure 4.3d. This circulation heats the NH, cools the SH, and pushes the Hadley cells and ITCZ slightly north of the equator, similar to the effects of the Atlantic Ocean's deep overturning circulation.

To shift the ITCZ further northward in both the slab and fully coupled models, we rock the hemispherically symmetric albedo distribution of the control run about the equator, reducing its value in the NH at the same rate it is increased in the SH (Figure 4.2a). The control albedo distribution α_{ctrl} and changes to it, $\Delta\alpha_{polar}$ for polar-amplified changes and $\Delta\alpha_{tropics}$ for tropics-only changes, are specified as:

$$\alpha_{ctrl} = \frac{1}{5}(2x^2 + 1) \qquad (4.1a)$$

$$\Delta\alpha_{polar} = -G\frac{x}{|x|}x^2 \qquad (4.1b)$$

$$\Delta\alpha_{tropics} = \begin{cases} -G' \cdot \sin(2\pi x), & |x| \leq 0.5 \\ 0, & |x| > 0.5, \end{cases} \qquad (4.1c)$$

where x is the sine of latitude. The multiplicative constant G specifies the magnitude of the polar-amplified albedo change; for the distributions in Figure 4.2a, it ranges from 0.1 to 0.4. In the most extreme case, G = 0.4, the NH albedo is a constant 0.2 and the SH albedo increases from 0.2 at the equator to 1.0 at the south pole. For tropics-only changes in albedo, G' is scaled so that when annual mean changes in absorbed shortwave radiation at the surface (Figure 4.2b) are averaged over the hemisphere, they match the first three polar-amplified distributions. It has values of 0.07, 0.14, and 0.22, and only three forcing amplitudes are used to prevent the albedo from decreasing below zero. The average heating of the NH in the lowest forcing case is 9.2 W m^{-2} for both the polar-amplified tropics-only forcing cases.

The modified albedo distributions are applied instantaneously to control runs of both the fully coupled and slab ocean model configurations, which are spun up for 1000 and 200 years respectively, and the models are then integrated further forward in time for 200 years. All results presented here are averages over the last one hundred years (101-200) after the forcing is applied, at which point the circulations and energy balance are in statistical equilibrium. In GM17, the energy balance equilibrated roughly 50 years after the forcing was applied, and the same is true for these runs (cf. Figure 5 of GM17). The control runs of the fully coupled and slab

ocean configurations are run for a further 100 years after the forced runs are initiated, and time means and monthly climatologies of the control runs for comparison to the forced responses are taken over these 100 years.

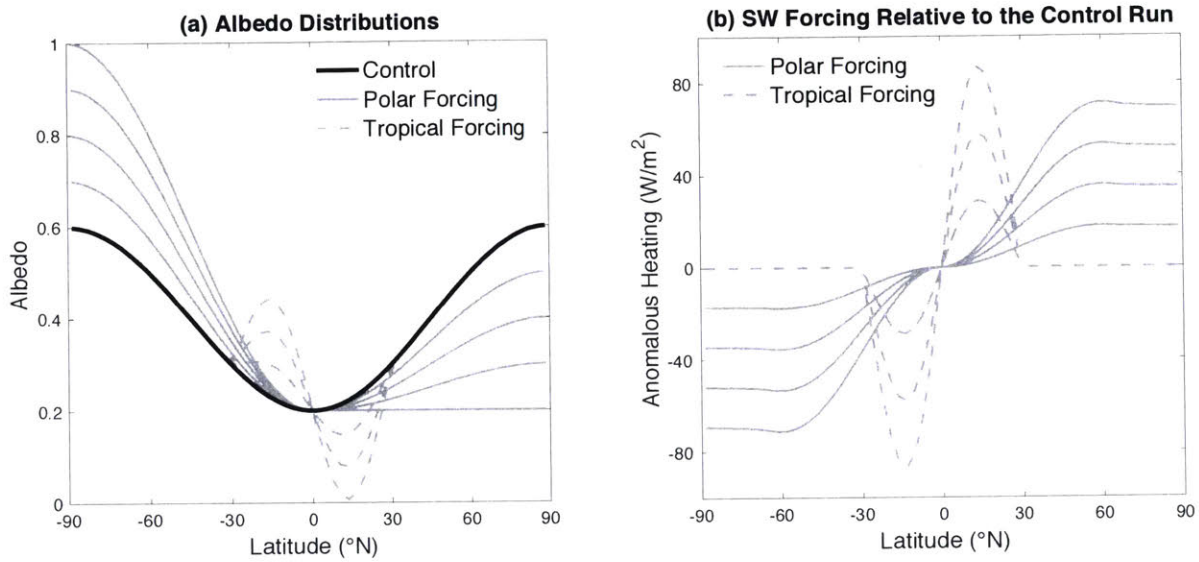

Figure 4.2. Distributions of interhemispheric forcing. (a) Surface albedo distributions for the control run (black line), polar forcing cases (solid gray lines), and tropical forcing cases (dashed gray lines). (b) The resulting changes in the net absorbed shortwave radiation in the annual mean.

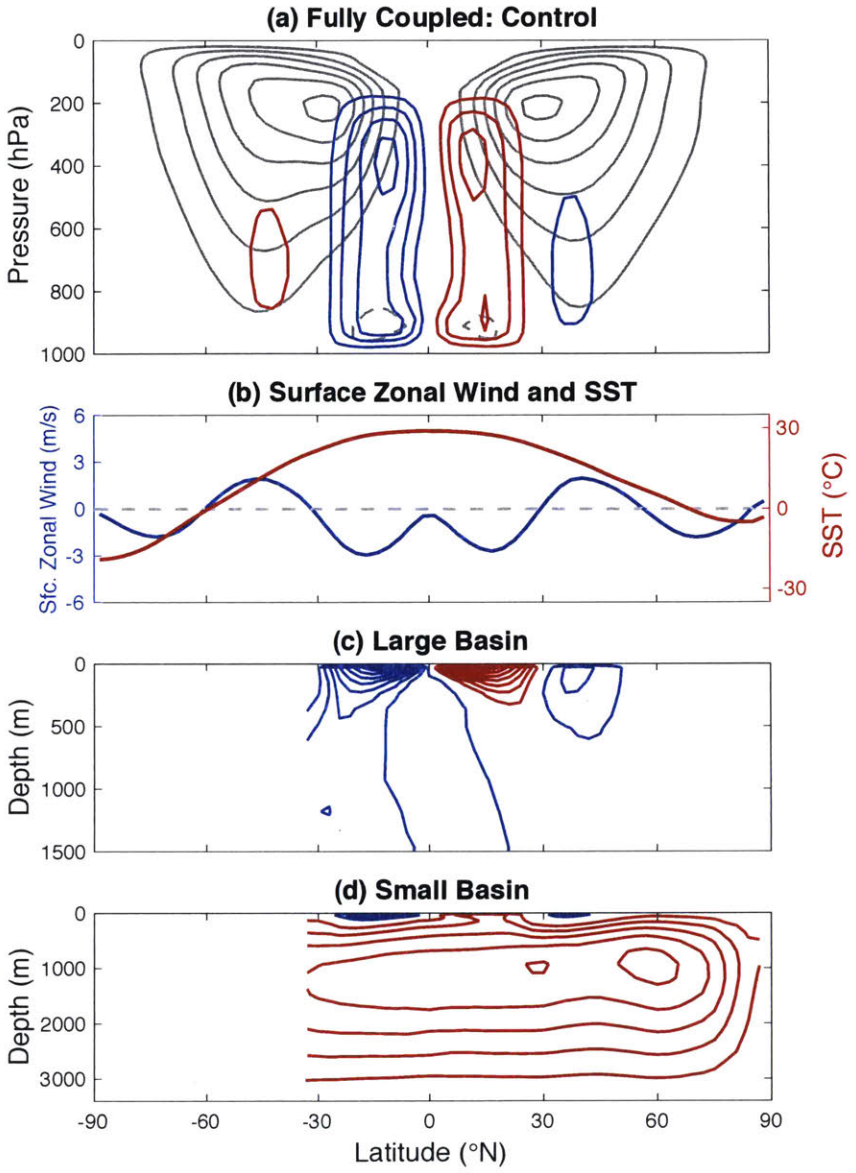

Figure 4.3. Zonal mean atmosphere and ocean circulations for the fully coupled control run. (a) Contours of the meridionally overturning streamfunction, with red contours indicating clockwise rotation and blue contours indicating counterclockwise rotation; the contour interval is 30 Sv (1 Sv = 10^9 kg s^{-1}). The gray contours indicate the zonal mean zonal wind; the contour interval is 5 m s^{-1}. (b) Zonal mean zonal wind at the model level closest to the surface, located at 993 hPa,

and zonal mean sea surface temperature. (c) Contours of the meridionally overturning circulation in the large basin and (d) the small basin, with red contours indicating clockwise rotation and blue contours indicating counterclockwise rotation; the contour interval is 5 Sv. The zero contour is not shown for both the zonal wind and the overturning streamfunctions.

4.3. ITCZ Shifts in the Polar-Amplified Forcing Cases

Comparing the responses of the zonal mean precipitation in the fully coupled runs to the slab runs for the polar-amplified forcing (Figures 4.4a and b, respectively), the anomalies are significantly damped in the fully coupled case. We define the ITCZ position using the centroid metric of Donohoe et al. (2013), where an area-weighted latitude of zonal mean precipitation is calculated between 20 °S and 20 °N. The northward shift of the ITCZ in the fully coupled runs is damped relative to the slab runs by a factor of 3.4 in the lowest forcing case, steadily declining to a factor of 2.1 in the highest forcing case. Correspondingly, the anomalous cross-equatorial energy transport by the atmosphere in the fully coupled runs is also reduced, between a factor of 2.5 and 2.7.

Changes in the zonal mean atmospheric circulation are much more dramatic in the slab ocean configuration. The NH Hadley cell in both model configurations has vanished in the highest forcing case (Figures 4.5a, d) and replaced by a single large cross-equatorial Hadley cell with a strength of 242 Sv in the fully coupled model and 590 Sv in the slab ocean model. The distributions of zonal mean zonal wind, in both the fully coupled and slab models show similarities, with the NH subtropical westerly jet at roughly 200 hPa being replaced by an eddy-driven extratropical jet. This jet is weaker in the slab ocean configuration, where eddies converge less angular momentum into the jet (not shown), perhaps as a result of the weaker meridional

gradient of extratropical SSTs in that model (Figure 4.5e). The stronger equatorial easterlies near the tropopause in the slab ocean case are consistent with the larger ITCZ shift, since air ascending in the poleward-displaced ITCZ in the slab runs has lower planetary angular momentum than in the fully coupled runs. Near-surface wind anomalies are correspondingly higher in the slab ocean case, with stronger SH easterly trade wind anomalies and a dramatic reversal of the NH trade winds to westerlies. The surface zonal stress imparted by these westerly winds is in approximate Ekman balance with the northward near-surface flow of the Hadley cell; the weaker cross equatorial Hadley cell in the fully coupled case does not reach the surface in the NH and the zonal winds just north of the equator are weak. Figures 4.5c and f show that the adjustment of ocean's overturning cells in both basins results in southward surface cross-equatorial flows and northward anomalous flow below.

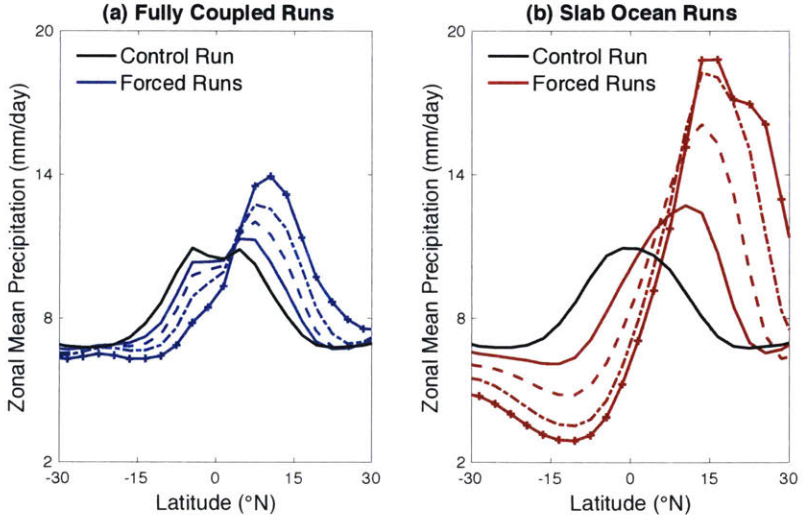

Figure 4.4. The precipitation response to the polar-amplified forcing distribution. (a) Annual mean, zonal mean precipitation in the fully coupled runs, with the blue lines indicating the precipitation distributions in response to progressively higher forcing amplitudes. (b) The same, but for the slab ocean runs.

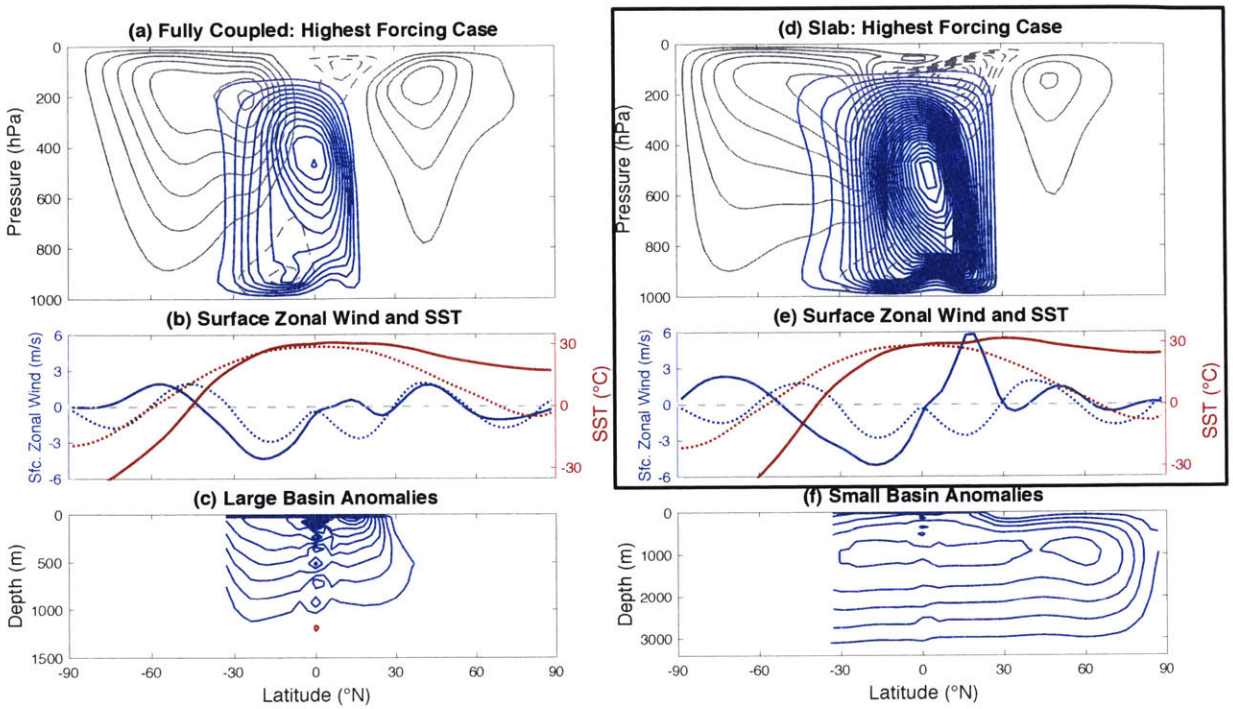

Figure 4.5. The response of the zonal mean circulation to the highest amplitude polar-amplified forcing, with the black box indicating slab ocean results. (a) The atmospheric meridional overturning streamfunction in the fully coupled run and (d) the slab ocean run, as in Figure 4.3a. Contour interval: 30 Sv and 5 m s^{-1}. (b) The near-surface zonal wind stress and SST in the fully coupled run and (e) slab ocean run, as in Figure 4.3b, with the control run distributions plotted as dashed lines. (c) Anomalies of the large basin and (f) small basin overturning streamfunctions. Contour interval: 5 Sv.

4.3.1. The Hemispheric Energy Balance

Contributions to the damped response of the ITCZ shift in the fully coupled case can be diagnosed using the atmosphere's energy balance, which ties the position of the ITCZ to the interhemispheric heating contrast. At a given latitude, any change in the net heating h (in W m^{-2})

of the atmosphere must be balanced by cooling due to anomalous net shortwave *sw* or longwave *lw* radiation at the top of the atmosphere and the anomalous divergence of the atmosphere's and ocean's northward energy transports, f_A and f_O:

$$h = -sw - lw + \nabla \cdot f_A + \nabla \cdot f_O. \qquad (4.2a)$$

Here, both *sw* and *lw* are defined as positive for downward fluxes at the top of the atmosphere to represent heating of the column. The term h represents any externally imposed heating; the terms on the right-hand side represent the adjustment of the climate system. Integrating h over both hemispheres and averaging the NH energy balance with the negative of the SH energy balance, Eq. (4.2a) becomes (in W):

$$H = -SW - LW - F_A - F_O \qquad (4.2b)$$

where F_A and F_O are the atmosphere's and ocean's northward cross-equatorial energy transports. In Eq. (4.2b), H now represents the anomalous interhemispheric heating contrast, positive if the NH is heated relative to the SH. By modifying the albedo distribution in Figure 4.2a, we apply an anomalous interhemispheric heating contrast at the top of the atmosphere, shown in Figure 4.2b, and the curves are the imposed anomalous heating h. For our antisymmetric heating distribution, H is equal to the integral of h over the NH. Since our model's atmosphere does not absorb shortwave radiation, the adjustment of *sw* and *SW* to the prescribed heating is identically zero, though these terms could be included in the energy budget to account for, for example, cloud

radiative effects or surface albedo feedbacks. The values of LW, F_A, and F_O are all anomalies relative to the control run.

On Earth and over the seasonal cycle of our model's control run (Figure 4.6a), the relationship between the ITCZ position and the atmosphere's cross-equatorial energy transport is approximately linear, so we can relate the ITCZ shift $\Delta\phi_{ITCZ}$ to F_A by the slope constant b:

$$\Delta\phi_{ITCZ} = -b \cdot F_A. \qquad (4.2c)$$

Over the seasonal cycle, the slope b is 1.8 ° PW^{-1} in the fully coupled control run; in the slab case control run, it is 2.1 ° PW^{-1}; on Earth, it is approximately 3 ° PW^{-1} (Donohoe et al., 2013). Our model has a lower value of b than the Earth for two reasons: an excess of subtropical precipitation that makes the centroid metric less sensitive to shifts in the precipitation maximum, and an ocean that cools the atmosphere at the equator more strongly than it does on Earth (Green and Marshall 2017). The model's atmosphere does not absorb shortwave radiation, resulting in an excess of surface heating by that stream relative to Earth, and precipitation rates are higher than they are in the real world. Our model's peak and subtropical precipitation rates in the fully coupled control run are 11 and 7 mm/day, respectively (Figure 4.4a); their values are approximately 6 and 2 mm/day on Earth. Combining Equations 4.2b and 4.2c, the relationship between the ITCZ shift and the interhemispheric heating contrast is:

$$\Delta\phi_{ITCZ} = b \cdot H \cdot C \qquad (4.3a)$$

$$C = \frac{-F_A}{H} = \frac{1}{1 + F_O/F_A + LW/F_A} \qquad (4.3b)$$

where C, the "degree of compensation", is the fraction of the interhemispheric heating contrast compensated for by the atmosphere's cross-equatorial energy transport. While the responses of the atmosphere's and ocean's circulations, and radiative fluxes are not easily separable, Eq. (4.3) shows how their interplay can affect the response of the ITCZ. If either the heated hemisphere loses more radiation to space (positive LW/F_A), or the ocean transports heat across the equator away from that hemisphere (positive F_O/F_A), the net heating experienced by that hemisphere's atmosphere is reduced, and its cross-equatorial energy transport and ITCZ shift are damped. If, however, the opposite occurs and the responses of the radiative fluxes or ocean energy transport act to amplify the imposed heating contrast (negative LW/F_A or F_O/F_A), the atmosphere has to compensate for a larger fraction of that heating and the ITCZ shifts even further.

The terms in Eq. (4.3b) are shown in Figure 4.6b for each model run versus the magnitude of the imposed heating contrast H. The degree of compensation is typically 0.8 in the slab case but only 0.3 in the coupled cases. This is due in large part to the large F_O/F_A term, representing an offsetting of the imposed heating H by an ocean circulation transporting roughly 70 % more energy southward across the equator than the atmosphere. Also contributing to a reduction of the degree of compensation in the fully coupled runs is an increase in LW/F_A, representing an increase in the efficiency of the longwave radiation at offsetting the heating contrast relative to the atmosphere's cross-equatorial energy transport. At lower values of the forcing amplitude, reductions in the slope b in the fully coupled runs (1.5 versus 1.9 ° PW^{-1} in the slab runs) also act to damp the ITCZ shift, but for the highest forcing case, they amplify it (1.4 versus 1.3 ° PW^{-1} in the slab runs). Since the terms in the energy balance in Figure 4.6b are approximately constant with forcing amplitude, the changes in b explain why ITCZ shifts in the fully coupled runs are less damped at higher forcing amplitudes. Given that F_O/F_A dominates

LW/F_A in the energy balance, and is nearly constant with the forcing amplitude, it is clear the large southward cross-equatorial energy transport by the ocean relative to the atmosphere is responsible for the damping of the ITCZ shifts.

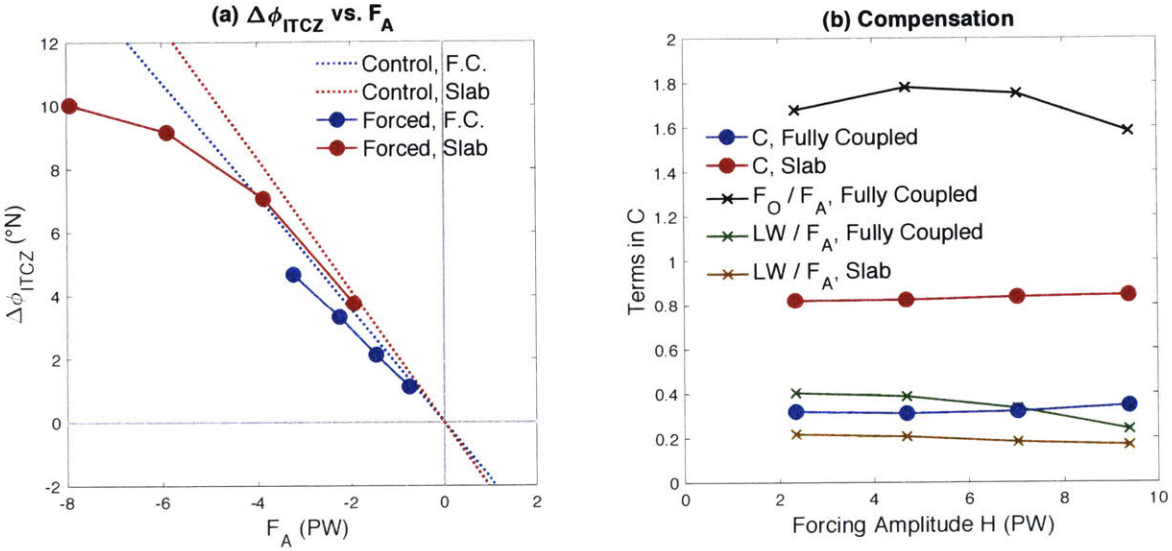

Figure 4.6. ITCZ shifts and the hemispheric energy balance for the polar-amplified forcing distribution. (a) The shift in the annual mean ITCZ position relative to the control runs versus the anomalous cross-equatorial energy transport in the atmosphere. Dashed lines indicate a least-squares linear regression of the two quantities' monthly mean climatologies from the fully coupled and slab ocean models' control runs. (b) The degree of compensation and the values of LW/F_A and F_O/F_A in the fully coupled and slab ocean runs, corresponding to the terms in Eq. (4.3b).

4.3.2. The Ratio of the Cross-Equatorial Energy Transports

The largest contributor to the relatively high cross-equatorial energy transport by the ocean in Figure 4.6b is the high stratification of the tropical ocean. Splitting the ratio of the oceanic to

atmospheric energy transports into the product of the ratio of their mass transports and gross stabilities as in Held (2001) and Czaja and Marshall (2006),

$$\frac{F_O}{F_A} = \frac{\psi_O}{\psi_A} \cdot \frac{c_O}{c_P} \cdot \frac{S_O}{S_A}, \qquad (4.4)$$

the ratios ψ_O/ψ_A and S_O/S_A are shown in red in Figure 4.7. By using the specific heat capacity of seawater (c_O, 3994 J kg^{-1} K^{-1}) and the specific heat at constant pressure of dry air (c_P, 1004 J kg^{-1} K^{-1}), the gross stabilities S_O and S_A have units of Kelvin, representing a measure of the temperature contrast between the upper and lower branches of the anomalous circulations. For the atmosphere, this measure of the gross stability represents the temperature contrast between parcels in the upper and lower branches of the circulation if all of their latent heat and potential energy were converted into sensible heat. Though the anomalous ocean circulation is 73-75 % weaker than the atmosphere, its gross stability is 54-59 % higher (red lines with circles). Compounding the higher temperature contrast of the oceanic circulation is the relatively high heat capacity of seawater; the ratio c_O/c_P is nearly four, making its product with the ratio of the gross stabilities range from 6.1-6.3. Thus F_O/F_A in Eq. (4.4) is 1.6-1.8.

The Hadley cells are responsible for the large majority, 78-82 %, of the atmosphere's cross-equatorial energy transport in the fully coupled runs, and their gross stability is within a couple Kelvin of a fit of the seasonal cycle in the control run (Figure 4.7b). It is slightly higher than the fit of the seasonal cycle across all the forcing amplitudes but lies within the range of individual monthly means. The ocean's anomalous cross-equatorial energy transport is accomplished by two distinct circulations: a shallow, wind-driven CEC confined to the thermocline in the large basin (Figure 4.5c), and a deep overturning circulation in the small basin

(Figure 4.5f), making the oceanic gross stability plotted in Figure 4.7b slightly unintuitive. Splitting the cross-equatorial energy transport into its small basin and large basin components and calculating the gross stability for each, both are lower than the global mean since the mass transport anomalies in each basin peak at different depths. The peak mass transport anomaly of the global zonal-mean ocean is then weaker than the sum of the two basins' peak mass transports, artificially increasing the global ocean's gross stability. Both basins' gross stabilities, though, are higher than the atmosphere's for all forcing amplitudes.

As the forcing amplitude increases, the gross stability of the large basin's CEC also increases, from 15 K to 19 K. The structure of the CEC, though, doesn't significantly change with the forcing amplitude, with southward-flowing surface water subducted in the SH extratropics returning northward in the thermocline. With the lower branch water conserving temperature as it flows northward, the gross stability of the CEC at the equator in our simulations is set by the SST contrast between the equator and the SH surface westerly jet, as in GM17. As the forcing amplitude increases, SH extratropical SSTs decrease (Figure 4.5b) and the gross stability of the CEC increases.

In the small basin, circulation anomalies are dominated by a weakening of the deep MOC, which shuts down completely in the highest forcing case and is replaced by a shallower CEC of the type seen in the large basin. With a large fraction of its upper branch inside the thermocline and its lower branch in the weakly stratified deep ocean, the deep MOC has a gross stability of 11 K in the control run, smaller than an anomalous CEC in the large basin. As the small basin's deep MOC weakens and its shallower CEC strengthens, the temperature contrast between the upper and lower branches of the circulation increases; the gross stability increases from 14 K in the lowest forcing case to 21 K in the highest forcing case. In the highest forcing

case, the anomalous circulation's gross stability is higher than the large basin's and is set by the difference between equatorial SSTs and the temperature of the deep ocean, rather than the temperature difference across the thermocline. The shift from a deep MOC to a shallow CEC in the small basin varies the fraction of its contribution to F_O as the forcing amplitude increases. For the three weakest forcing amplitudes, each basin contributes nearly equally to F_O; for the highest forcing amplitude, the small basin's contribution reduces to 43 % because the deep MOC can no longer weaken and because the 90 °-wide small basin's shallow CEC is weaker than its counterpart in the 270 °-wide large basin.

Although it is constrained to overturn in the same sense at the atmosphere's circulation by its coupling to the trade winds, the tropical ocean circulation is not constrained to have the same strength, and its anomalies are weaker in our simulations (Figure 4.7a). Similar to GM17, the anomalous cross-equatorial ocean circulation in these simulations is approximately in Ekman balance with the surface wind stress, nearly matching the Ekman mass transport calculated from zonal wind stress anomalies averaged at 6 °N and 6 °S. The Ekman transport, confined to a near-surface frictional layer in the ocean and atmosphere, is weaker than the total atmospheric overturning anomaly, which peaks in the mid-troposphere (Figure 4.8a). For the atmospheric and oceanic mass transports to be identical, the peak atmospheric overturning anomaly would have to extend down to the top of this layer, located at approximately 900 hPa in our model.

The atmosphere's angular momentum balance, where the divergence of angular momentum transport by the Hadley cells and eddies is balanced by torques associated with surface friction and pressure torques (cf. Peixoto and Oort, 1992 Eq. 11.12-13), dictates the strength of the trade winds and the resulting oceanic overturning circulation. The anomalous oceanic CEC in our simulations is driven by a hemispherically asymmetric pattern of surface

zonal wind stress, so in Figure 4.8b we plot the difference between the torques at 6 °N and 6 °S exerted on the atmosphere by the zonal wind stress anomalies and the convergence of angular momentum transport by the Hadley cells. Over both the seasonal cycle in the control run and in the annual mean of the forced runs, the two nearly perfectly balance each other, and the effects of eddy momentum transport are small (there are no surface pressure torques in our model's atmosphere). That both the annual mean angular momentum balance and the mass transport ratio ψ_O/ψ_A in the forced runs closely match the seasonal cycle in the control run suggest that the strength of an anomalous oceanic CEC can be predicted by the seasonal cycle of the Hadley cells, without accounting for the effects of eddy angular momentum transport. It is also worth noting that as long as the oceanic CEC is in Ekman balance with the surface wind stress, depending on the atmosphere's angular momentum balance, its strength may increase and approach that of the anomalous Hadley cell, but it can never be stronger and the ratio ψ_O/ψ_A cannot exceed unity.

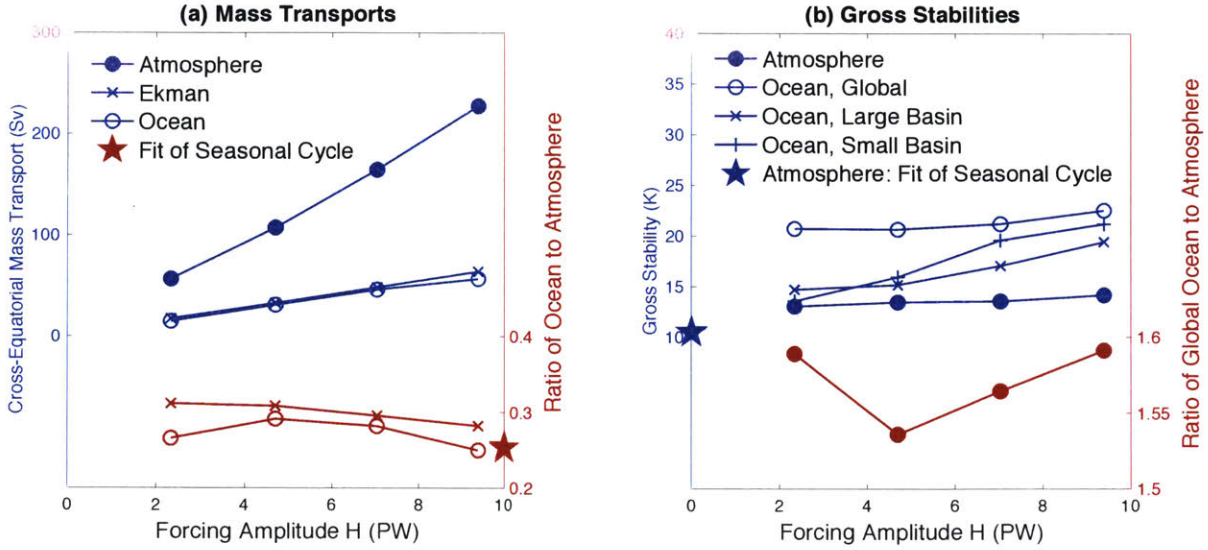

Figure 4.7. Contributions to the atmosphere's and ocean's cross-equatorial energy transports in the fully coupled model runs for the polar-amplified forcing distribution. (a) Annual mean mass transport anomalies (blue), taken as the peak meridional overturning streamfunction anomaly at the equator in the atmosphere and an average of peak anomalies at 6 °N and 6 °S in the ocean. The Ekman transport is calculated using the surface wind stress anomalies at 6 °N and 6 °S, integrating the resulting Ekman transport in longitude, and averaging the two values. The ratio of the ocean and Ekman mass transport anomalies to the atmosphere's is shown in red, with a fit of the Ekman-atmosphere ratio (indicated with a star) calculated as a least-squares fit of monthly mean climatologies from the control run. (b) Gross stabilities (blue), calculated as the ratio of the anomalous cross-equatorial energy and mass transports, divided by the heat capacity. The blue star indicates the average monthly mean gross stability of the atmosphere from the control run. The ratio of the atmosphere's to the global ocean's gross stability is shown in red.

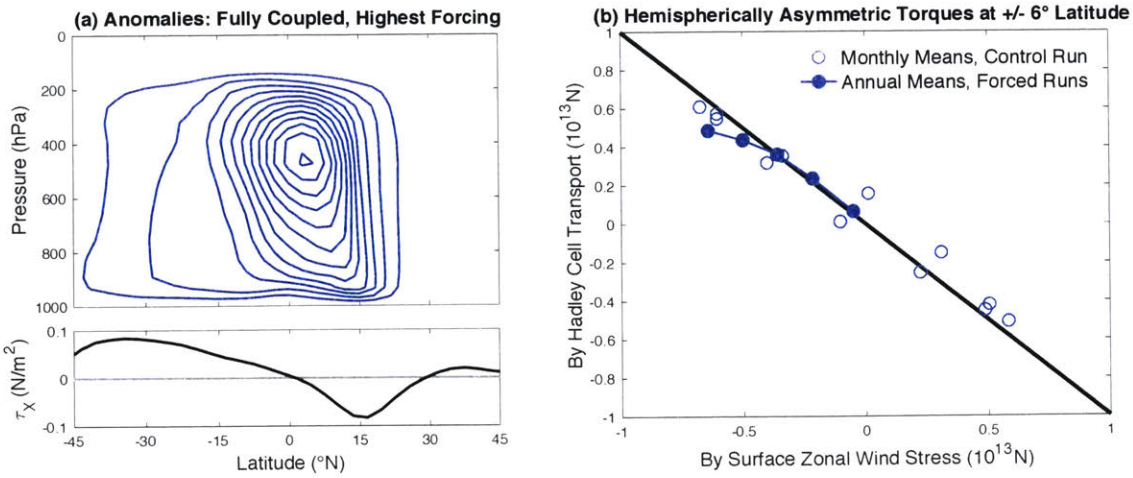

Figure 4.8. The atmosphere's angular momentum balance in the fully coupled model for the polar-amplified forcing distribution. (a) Anomalies in the highest forcing case in the meridional overturning streamfunction (top, coutour interval: 20 Sv) and the surface zonal wind stress on the atmosphere (bottom). (b) The difference between the integrated (vertically and zonally) torques on the atmosphere at 6 °N and 6 °S, with positive values indicating a positive torque on the northern hemisphere atmosphere relative to the southern hemisphere. The y-axis is the convergence of angular momentum transport by the time mean, zonal mean circulation, and the x-axis is the torque exerted by the zonal mean zonal wind stress at the surface.

4.3.3. The Ocean's Impact on the Radiative Response

The increased longwave radiative efficiency LW/F_A in the fully coupled runs (Figure 4.6b) also contributes to the damping of ITCZ shifts, although the effect is small relative to F_O/F_A. Per Petawatt of cross-equatorial atmospheric energy transport, the NH in the fully coupled runs is fluxing nearly double the anomalous longwave radiation to space than it is in the slab runs for all the forcing amplitudes. This increase in the efficiency of the longwave radiation can be

understood by returning to the atmosphere's energy balance. Modifying Eq. (4.2a) by incorporating the convergence of the ocean's heat transport into the left-hand side to define a "net heating" of the atmosphere, $h_{net} = h - \nabla \cdot f_O$, the atmosphere's energy balance at a given latitude is:

$$h_{net} = -lw - sw + \nabla \cdot f_A. \qquad (4.5a)$$

In the slab ocean runs, there is no change in the ocean heat transport convergence and $h_{net} = h$. Since *sw* is again zero for our simulations, the response of the atmosphere to the combination of the albedo forcing and anomalous ocean heat transport convergence is a balance between outgoing longwave radiation at the top of the atmosphere and atmospheric energy transport divergence. An integral of Eq. (4.5a) over a hemisphere, analogous to Eq. (4.2b), yields a balance between the hemisphere's net heating, its net outgoing longwave radiation *LW*, and the atmosphere's cross-equatorial energy transport F_A. The increase in LW/F_A in the fully coupled runs indicates a shift in the response from the latter to the former and, we will argue, is a result of the ocean's heat transport modifying the meridional profile of the net heating of the atmosphere.

The meridional profiles of net heating can be compared between the simulations by normalizing Eq. (4.5a) by the northern hemisphere's average net heating (the SH average is the same magnitude but opposite sign), denoted with an overbar:

$$\frac{h_{net}}{\bar{h}_{net}} = \frac{-lw}{\bar{h}_{net}} + \frac{\nabla \cdot f_A}{\bar{h}_{net}}. \qquad (4.5b)$$

These normalized profiles are plotted in Figure 4.9a versus the sine of latitude to area-weight the distribution. All of the slab ocean cases collapse onto a single line taking the shape of the albedo forcing, and it is notable how similar the fully coupled cases are given the range of forcing amplitudes. Comparing the two sets of curves, the effect of the ocean's heat transport in the fully coupled runs is to concentrate the net heating at higher latitudes; in the tropics, heating in the NH has changed to cooling and cooling in the SH has changed to heating.

The redistribution of net atmospheric heating in the fully coupled runs to higher latitudes is due to the mismatch of the profiles of the albedo-forced heating and the ocean's anomalous heat transport convergence and resulting surface heat fluxes. The heating driven by the albedo changes is strongly polar-amplified, but roughly half of the ocean's anomalous cross-equatorial heat transport is diverged or converged equatorward of 30 ° (Figure 4.9b), heating and cooling the atmosphere at latitudes where the imposed heating is weak. In the highest forcing case, 74% of the large basin's cross equatorial heat transport is converged/diverged equatorward of 30 °. Because the large basin's anomalous heat transport is coupled to the atmospheric circulation above, the redistribution of a polar-amplified heating profile further poleward by the type of wind-driven CEC described in GM17 appears to be a robust feature of the climate's response.

By itself, a change in the distribution of the net heating profile is not sufficient to alter the balance between the longwave radiative fluxes and atmospheric cross-equatorial energy transport – the atmosphere's partitioning of its response between radiative fluxes and energy transport divergence must also have a meridional dependence. In our simulations, the longwave radiative feedback (defined as the change in outgoing longwave radiation at the top of the atmosphere divided by the change in SST) is positive when averaged between the equator and 30 ° latitude and negative when averaged between 30 ° and the poles, reflecting the relative efficiency of the

extratropical atmosphere at radiating heating anomalies away to space. Our gray radiation model only has Planck, lapse rate, and water vapor feedbacks, of which only the water vapor feedback is positive, and the net positive tropical radiative feedback can be attributed to the relatively high concentrations of water vapor there.

With our model's atmosphere able to radiate heating anomalies to space more efficiently at high latitudes, by concentrating the profile of the net heating of the atmosphere there, the ocean increases the relative contribution of longwave radiative fluxes to equilibrating the atmosphere's energy balance. This effect can be related to the ratio LW/F_A by integrating Eq. (4.5a) over a hemisphere and dividing by F_A. Re-arranging the terms gives

$$\frac{LW}{F_A} = \frac{1}{C_S} - 1 \qquad (4.5c)$$

$$C_S = \frac{-F_A}{H_{net}} = \frac{-F_A}{H + F_O} \qquad (4.5d)$$

where C_S is the "slab compensation," the degree of compensation expected in a slab ocean model if it was presented with the forcing distribution h_{net}. Equation (4.5c) is equivalent to Eq. (4.3b) if F_O/F_A was removed from the denominator and F_O was added to H. Since the profiles of net heating in Figure 4.9a are further polar-amplified in the fully coupled runs and the atmosphere more efficiently radiates heating anomalies to space at those latitudes, the atmosphere's degree of compensation C_S decreases compared to the slab ocean runs (Figure 4.9c) and LW/F_A increases. This result is consistent with previous modeling studies with a slab ocean GCM, where C_S was higher for forcing distributions that were polar-amplified (Seo et al. 2014, Kang et al.

2014). Moreover, in simulations of global warming, patterns of ocean heat uptake interacting with radiative feedbacks have been shown to alter the equilibrium climate sensitivity (Rose et al. 2014); our results reinterpret this effect for interhemispheric forcing.

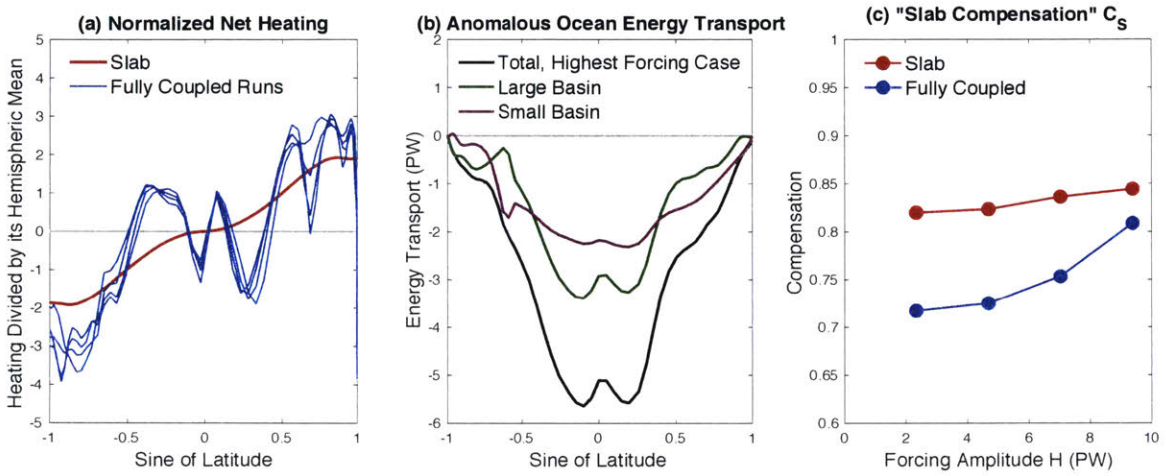

Figure 4.9. The effect of the ocean on the atmosphere's radiative fluxes for the polar-amplified forcing distribution. (a) Normalized net heating of the atmosphere, following Eq. (4.5b). (b) Anomalous ocean energy transport in the fully coupled, highest forcing case. (c) The atmosphere's degree of compensation for the "net heating" it experiences, following Eq. (4.5c).

4.3.4. The Relationship Between the ITCZ Position and the Atmosphere's Cross-Equatorial Energy Transport

The connections between the ocean circulation and the slope of the $\Delta\phi_{ITCZ}$-F_A relationship are less direct and vary with the forcing magnitude. Differences in the slope can be interpreted as a measure of how efficiently the atmosphere moves energy across the equator: to accomplish a given cross-equatorial energy transport and equilibrate its energy budget, a lower value of b means that the atmosphere doesn't have to shift the ITCZ as far as it would for a higher value.

For a given atmospheric cross-equatorial energy transport F_A, the slope b is always reduced in the fully coupled runs (solid lines, Figure 4.10a). As the forcing amplitude increases in the slab ocean runs and the magnitude of F_A increases past its maximum in the fully coupled runs, b reduces as the atmosphere becomes more efficient at moving energy southward across the equator. This is perhaps to be expected, particularly at high forcing amplitudes, if the Hadley cells enters a non-linear, angular momentum conserving regime and the strength of the cross-equatorial cell increases super-linearly with the latitude of the ITCZ (Lindzen and Hou 1988, Plumb and Hou 1992). Indeed, as the ITCZ moves further northward in the slab runs, the strength of the anomalous cross-equatorial Hadley cell increases super-linearly with its position, but the relationship remains linear for the smaller ITCZ shifts in the fully coupled runs (not shown). The apparent amplification of ITCZ shifts at high forcing amplitudes by the ocean circulation's effect on b, then, is artificial – the high ITCZ shifts in the slab ocean runs are only realized without the damping effect of the ocean's cross-equatorial energy transport.

At lower forcing amplitudes and values of F_A, b is consistently lower in the fully coupled runs, contributing to the damping of the ITCZ shift. Comparing the precipitation distributions for similar values of F_A (-2.2 PW in the fully coupled case versus -1.9 PW in the slab case; Figure 4.10b), part of the reason for the lower slope in the fully coupled run are the higher precipitation rates in the subtropics. The centroid metric we use is an area-weighted latitude of precipitation between 20 °S and 20 °N, and the increases in precipitation between 5 °S and 20 °S project onto a southward shift of the metric relative to the slab case. This increase in subtropical precipitation in the fully coupled model is also seen when comparing its highest forcing case to the slab model's second-lowest forcing case.

Since we are focusing on changes in the position of the ITCZ, rather than in subtropical precipitation rates, we compare the results using the centroid metric to those where the position of the ITCZ is defined as the latitude where the atmosphere's northward energy transport vanishes, termed energy flux equator (EFE; Kang et al. 2008). By using the atmosphere's energy transport distribution to define the ITCZ position, the EFE metric is more closely related to the atmosphere's energy balance than the centroid metric, at the cost of not being directly related to changes in precipitation.

For all forcing amplitudes, the slope b using the EFE metric is higher in the fully coupled runs relative to the slab ocean runs (Figure 4.10a), implying an amplification of the ITCZ shift in the fully coupled case. However, we again see that this is because of a dependence of b on the magnitude of F_A. In the EFE estimation of the ITCZ position, the curvature of the atmosphere's northward energy transport with latitude plays a non-negligible role once the ITCZ moves more than a couple degrees from the equator (Bischoff and Schneider 2016). In agreement, we see a reduction in monthly mean values of b as the magnitude of F_A increases in the control simulations for both the fully coupled and slab ocean models' control runs (Figure 4.10c). However, this same dependence of b on F_A over the control runs' seasonal cycles is not seen if the centroid metric is used.

At a given value of the atmosphere's cross-equatorial energy transport F_A, there appears to be a reduction in the slope b using the EFE metric for the fully coupled runs. Again comparing the lowest-forcing slab case to the second-highest forcing fully coupled case, b is reduced by 11 %. In the EFE framework, this means that the atmosphere is diverging more heat between the ITCZ position and the equator in the fully coupled run, steepening the slope of its northward energy transport distribution as a result of a net input of energy into the region. Comparing the

two runs between the equator and 9 °N, the approximate latitude of the ITCZ in both cases, there is an increase in the net surface energy flux of 5.2 W m^{-2} in the fully coupled run, of which 23 % is compensated by an increase in the outgoing longwave radiation at the top of the atmosphere. The rest of the heating is diverged by the atmosphere, steepening the slope of its energy transport curve and reducing the value of b. This local increase in the upward surface heat flux is a result of a convergence of the ocean's heat transport, seen just north of the equator in Figure 4.9b, and is connected to a reduction in the ocean's anomalous southward heat transport right at the equator. Across all forcing amplitudes, similar reductions in the southward heat transport at the equator occur in the fully coupled runs and are related to a sinking and cooling of some of the surface wind-driven flow as it crosses the equator (see GM17). As a consequence of the equatorial structure of the wind-driven CEC, a reduction in the slope b and a damping of ITCZ shifts appears to be a robust feature of the fully coupled runs.

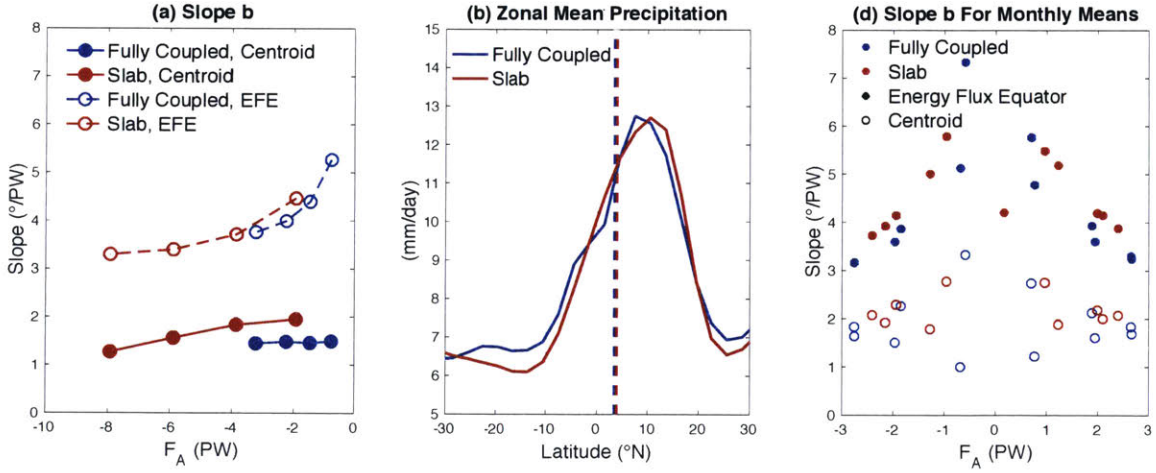

Figure 4.10. The slope of the $\Delta\phi_{ITCZ}$ - F_A relationship for the polar-amplified forcing distribution. (a) For the centroid metric (solid) and energy flux equator metric (dashed), versus the atmosphere's anomalous cross-equatorial energy transport. (b) Zonal mean precipitation

distributions for the fully coupled model's second-highest forcing amplitude case and the slab ocean model's weakest forcing case. Dashed lines indicate the ITCZ positions, calculated using the centroid metric. (c) The slope b calculated from monthly mean climatologies of the fully coupled and slab ocean models' control runs, for both the centroid metric and the energy flux equator metric.

4.4. Forcing Confined to the Tropics

To test the robustness of the ocean circulation's damping effect on ITCZ shifts, we compare the previous section's results to those where the forcing is confined to the tropics. By limiting the albedo adjustments to the tropics, these runs' heating profiles (Figure 4.2b) have larger gradients than the polar-amplified distributions, increasing in amplitude from zero at the equator, peaking at 14.5 ° latitude, and decaying to zero at 30 ° latitude. It is difficult to imagine a realistic interhemispheric forcing of this magnitude that is confined to the tropics, particularly for a fully coupled atmosphere-ocean system, but the response of our model to these idealized forcing distributions provides a useful contrast to the polar-amplified distributions discussed above.

The resulting ITCZ shifts (Figure 4.11a) are still damped in the fully coupled runs relative to the slab ocean runs, but by a smaller amount than they are for the polar-amplified forcing distribution. From the smallest amplitude forcing case to the largest amplitude case, the ratio of the slab to fully coupled runs' ITCZ shifts decreases from 1.7 to 1.5, lower than the 3.4 to 2.8 range for the same forcing amplitudes in Figure 4.6a. The atmosphere in the fully coupled runs also transports a larger fraction of the forcing southward across the equator; the degree of compensation C by the atmosphere's cross-equatorial energy transport ranges from 0.63 to 0.66 (Figure 4.11b), compared to a range of 0.31 to 0.34 in Figure 4.6b. The slab ocean runs' range of

C, 1.00 to 1.02, is also higher in these runs than before, but the relative increase in C in the fully coupled runs is higher.

The largest contributor to the reduction in the damping of ITCZ shifts is a reduction in the ocean's cross-equatorial energy transport. Smaller contributions come from changes in the compensation by longwave radiation and the slope b. The ocean's cross-equatorial energy transport is roughly 60 % of the atmosphere's in these runs (Figure 4.11b), much lower than before (Figure 4.6b), and there are now only minimal changes in LW/F_A between the slab ocean and fully coupled runs. For a given forcing amplitude, changes in b between the fully coupled and slab runs are small, whereas for similar polar-amplified forcing amplitudes they contribute to a larger fraction of the damping. The consequence of the small changes in LW/FA and b is that the ocean's anomalous cross-equatorial energy transport, lower than it was in the polar-amplified forcing cases, is the sole agent acting to damp the ITCZ shift in the fully coupled runs.

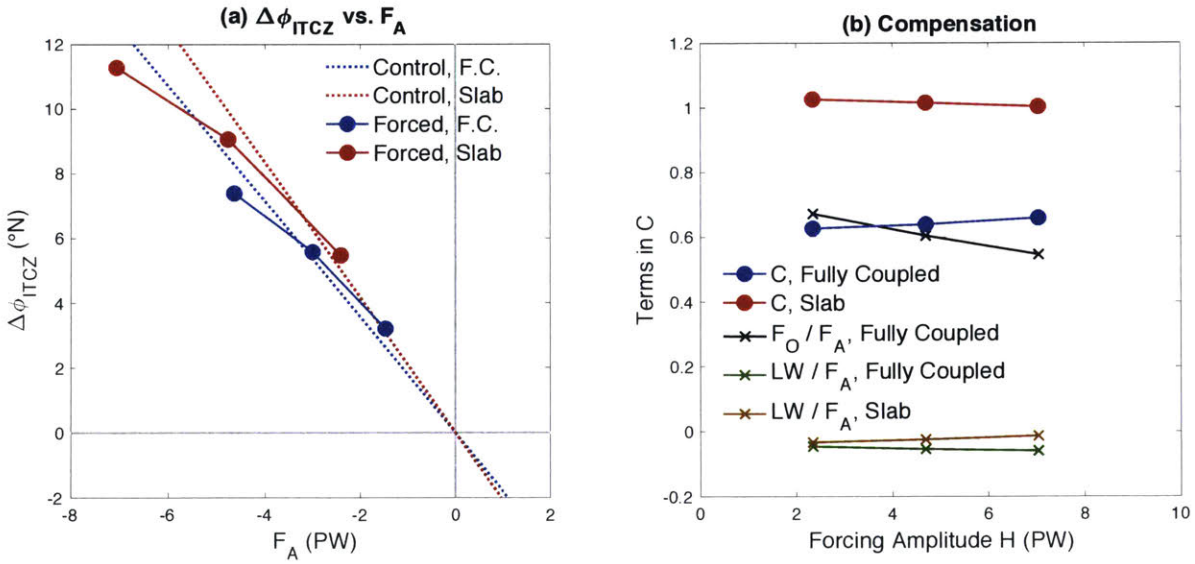

Figure 4.11. ITCZ shifts and the hemispheric energy balance, as in Figure 4.6, for the tropics-only forcing distribution.

4.4.1. Ocean Circulation and Energy Transport Anomalies

The most noticeable difference in the ocean's circulation, compared to the polar-amplified forcing cases, is the relatively small change in the small basin's deep MOC, even in the highest forcing case (Figure 4.12f). Instead of a weakened deep MOC transporting heat anomalously southward across the equator, as in Figure 4.5f, the largest streamfunction anomalies in the small basin are confined to the thermocline, similar to the large basin (Figure 4.12c). Both basins' anomalous circulations are surface-intensified CECs like those described in Section 4.3.2, driven by the surface zonal wind stress anomalies and transporting heat southward across the equator due to the temperature contrast between the surface and return branches. The small basin/large basin split of the ocean's cross-equatorial energy transport is 30/70 % in the highest forcing case, reflecting the relative sizes of the basins. The reduced fraction of cross-equatorial heat transport accomplished in the small basin is partially responsible for the reduction of the total oceanic transport and the reduced F_O/F_A: without a weakening of the deep MOC, the size of the small basin limits the heat transported by its wind-driven CEC.

The pattern of surface zonal wind anomalies (Figure 4.12b) are more localized for the tropics-only forcing distribution, and the anomalous wind-driven CECs in both basins are confined to within roughly 20 ° latitude of the equator. Rather than supplying the CECs with water pumped downward in the extratropics due to a southward shift of the SH surface westerly jet, as in Figure 4.5b, the surface wind anomalies in Figure 4.12 reflect a more local northward shift of the trade winds in the tropics. Reduced eddy momentum fluxes in the SH extratropics (not shown) weaken the SH surface westerly jet, but the jet does not shift and anomalies in the trade winds and resulting meridional Ekman transport switch sign at 20 °S. This reduction in the CEC widths relative to the polar-amplified forcing runs leads to a reduction in their gross

stabilities. Both the large and small basin wind-driven CECs have a gross stability of 12 K, reduced from 15-19 K for the large basin in Figure 4.7b, that does not vary strongly with the forcing amplitude since SST anomalies are weaker in these runs (compare Figure 4.12b to Figure 4.5b). The reduction in the CEC's gross stability is due to a warming of the western boundary current that comprises the lower branch of the CEC, with that current crossing the equator at shallower depths and warmer temperatures in these tropics-only forcing cases. This warming of the boundary current, driven by Ekman pumping at lower latitudes compared to the polar-amplified forcing runs, is partially responsible for the reduction of the ocean's cross-equatorial energy transport relative to the atmosphere.

Though clearly driven by the surface wind stress anomalies, the CECs in the tropics-only forcing runs are weaker than circulations in Ekman balance with those anomalies would be. The strength of the cross-equatorial mass transport in these runs is only 61-63 % of the implied Ekman transport, compared to 85-95 % for the polar-amplified forcing runs in Figure 4.7a. Diagnosing the model's zonal momentum balance in the surface layer, the zonal wind stress anomalies in these runs are partially offset by the horizontal diffusion of zonal momentum. As a result, the Coriolis acceleration on the meridional flow is weaker than it would be if the surface flow was in Ekman balance. The horizontal viscosity in the momentum equation for this version of the MITgcm ocean model is a spatially uniform 3×10^5 m^2 s^{-1}, similar to other ocean general circulation models in the tropics (e.g. Griffies et al. 2005), following the Munk scaling for western boundary currents (Munk 1950). However, most of the dissipation of anomalous zonal momentum in these runs occurs in the interior of the basins, and this type of diffusion-driven weakening of the CECs is likely unphysical. By confining the anomalous CECs to a narrower range of latitudes, gradients in surface currents resulting from the more local wind stress

anomalies are higher, and the model more strongly dissipates the resulting momentum. Through Eq. (4.4), the reduction in the CECs' mass transport anomalies relative to the atmosphere compounds their reduced gross stability and reduced small basing heat transport, leading to the lower F_O/F_A values in the tropics-only forcing cases.

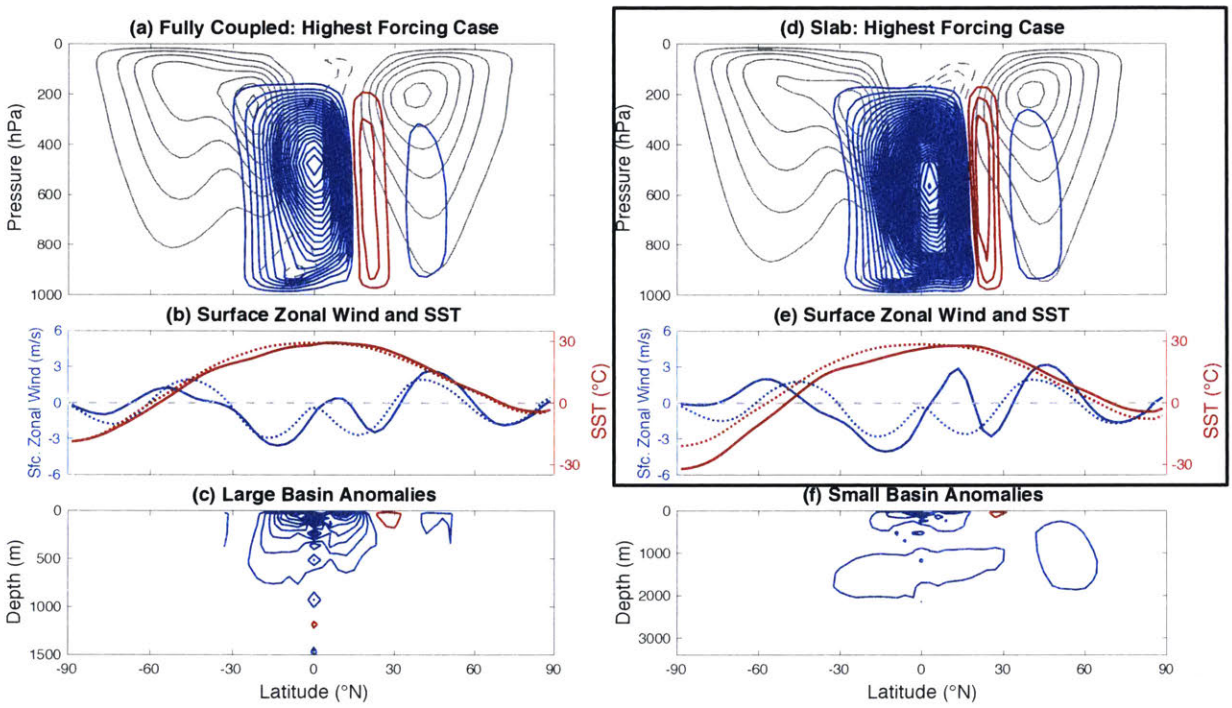

Figure 4.12. The response of the zonal mean circulation, as in Figure 4.5, to the highest amplitude tropics-only forcing.

4.4.2. Changes in LW/F_A and the Slope b

The response of the longwave radiation is very similar in the slab ocean and fully coupled runs (Figure 4.11b) and LW/F_A is smaller than in the polar-amplified forcing runs (Figure 4.6b). By concentrating the forcing in a region where the radiative feedbacks in our model are positive, the

tropics-only forcing distribution results in small negative values of LW/F_A. The similar values of LW/F_A in the slab ocean and fully coupled runs are related to the distribution of net heating in the atmosphere (Figure 4.13a): though the ocean reduces the interhemispheric heating contrast, it does not significantly modify its distribution. The anomalous cross-equatorial energy transport in the both basins' narrower CECs is diverged and converged almost entirely within 25 ° of the equator, in close alignment with the forcing distribution and preventing its interaction with the model's spatial pattern of radiative feedbacks from altering LW/F_A.

The weak damping of the ITCZ shifts by changes in the slope b in the fully coupled runs is again found to be more pronounced when b is plotted versus F_A (Figure 4.13b). The causes of the reduction in b, for both the centroid and EFE metrics, in the fully coupled runs are identical to those discussed in Section 4.3.4. Subtropical SH precipitation is similarly reduced when slab and fully coupled runs with similar F_A are compared (not shown), and a reduction in the ocean's anomalous southward heat transport at the equator again leads to a heating of the atmosphere just north of the equator. Since the anomalous circulation in the small basin now more closely resembles the wind-driven CEC in the large basin, the local reduction in the global ocean's heat transport is more pronounced for these runs and the reduction in b using the EFE metric are higher when compared to the polar-amplified forcing runs (Figure 4.10a). Though it is not the primary mechanism by which the ocean damps ITCZ shifts, a reduction in the slope of the ITCZ position-atmospheric cross-equatorial energy transport relationship appears to be robust.

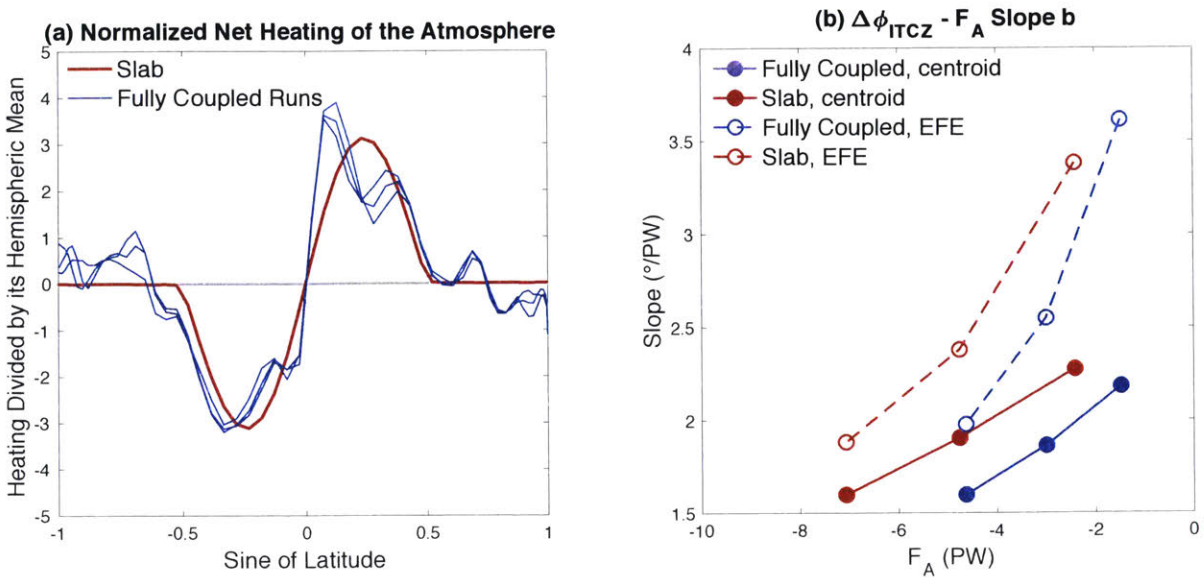

Figure 4.13. The effect of the ocean on the atmosphere's radiative fluxes and slope *b* in the tropics-only forcing cases. (a) Normalized net heating of the atmosphere, following Eq. (4.5b), as in Figure 4.9a. (b) The slope *b* calculated using the energy flux equator and centroid metrics, versus the atmosphere's anomalous cross-equatorial energy transport, as in Figure 4.10a.

4.5. Discussion of the Role of the CEC in the Atmosphere's Energy Balance

In our simulations, the ocean accomplishes its cross-equatorial energy transport by "wrapping" a cross-equatorial cell around the STCs, with its lower branch crossing the equator at colder temperatures than the STCs' lower limbs. By crossing the equator in a frictional western boundary current, the CEC's lower branch is able to reverse the sign of its potential vorticity. Our results disagree with the type of ocean circulation envisaged by Schneider (2017) which, as schematized in his Figure 2, suggests that the ocean accomplishes its cross-equatorial energy transport by shifting the upwelling zone in the interior ocean along with the ITCZ: for a

northward ITCZ shift this would result in a cross-equatorial SH subtropical cell that mirrors its counterpart Hadley cell. In our simulations, though the latitude of mean ascent in the atmosphere shifts with the ITCZ, the tropical ocean's upwelling zone never shifts off of the equator (Figure 4.14). We propose that the tropical ocean circulation for a northward ITCZ shift is more accurately schematized in Figure 4.1: instead of the upwelling zone shifting to the latitude of the ITCZ, southward cross-equatorial flow at the surface is balanced by a northward flow in the thermocline below the STCs. The southward cross-equatorial surface flow does not imply a shift in the upwelling zone and distribution of surface divergence; rather, it is the addition of a constant southward flow throughout the tropics to the background divergent flow.

Anchoring the upwelling zone to the equator is a surface zonal wind stress distribution that results in a peak Ekman transport divergence there. In our simulations, and as described in GM17, an ITCZ shift results in a pattern of wind stress anomalies that are linear about the equator and, when those anomalies are divided by the Coriolis parameter, Ekman transport anomalies that are roughly constant with latitude. This result is in agreement with Miyama et al. (2003), which describes the cross-equatorial cell in the Indian Ocean as driven by surface zonal wind stresses that are similarly linear and asymmetric about the equator. Should the STCs' upwelling zone be coupled to the ITCZ position and shift off of the equator, the water in the lower limb of one hemisphere's STC would have to reverse the sign of its potential vorticity to cross the equator. It could cross the equator in a western boundary current, like the CEC's lower branch in our simulations, or by mixing with water from the other hemisphere (e.g. Hüttl-Kabus and Böning 2008). Above, an atmospheric streamfunction that would drive off-equatorial upwelling would be relatively vertically uniform, with values at the top of the Ekman layer very similar to those near the tropopause and vertical velocities that are constant with pressure. This is

not the case for either our polar-amplified forcing simulations (Figure 4.5a) or tropics-only forcing simulations (Figure 4.12a), which both have atmospheric streamfunctions with meridional mass transports that are weaker near the surface than they are near the tropopause and vertical velocities that peak at about 500 hPa. This decoupling of the Ekman mass transport from the total Hadley cell mass transport has important implications for the CEC's energy transport.

The second point where our results differ from the framework proposed by Schneider (2017) is the strength of the CEC. Schneider assumes that the wind-driven CEC has the same strength as the cross-equatorial Hadley cell; in our simulations, the CECs are much weaker than their atmospheric counterparts (Figure 4.7a). They are broadly in Ekman balance with the surface zonal wind stress, but the Ekman transport is not constrained to be the same strength as the Hadley cells, instead balancing the divergence of angular momentum transport in the tropics as described in Section 4.3.2. This can be more easily appreciated by examining the vertical structure of the atmospheric mass transport streamfunction (e.g. Figure 4.8a): the streamfunction maximum occurs in the mid-troposphere, away from the frictional boundary layer and its associated Ekman transport.

The differences in the two descriptions of the CEC and its heat transport have an impact on how the atmosphere's energy balance is evaluated to predict the magnitude of the ITCZ shift. Schneider (2017) estimates F_O/F_A to be equal to the ratio of the ocean's heat uptake at the equator to the net heating of the atmosphere at the equator, consistent with his assumption that the upwelling zone shifts with the ITCZ. For a northward ITCZ shift, this amounts to an identical shift northward of the vertically and zonally integrated distribution of northward ocean heat transport in the tropics. In our simulations, the effect of the CEC is not to shift the OHT distribution north, but to subtract a relatively constant value throughout the tropics (Figure 4.9b).

Interestingly, the two approaches to the energy balance give similar estimates for the amplitude of the damping of ITCZ shifts by the ocean circulation, due to offsetting differences in their description of the ocean's cross equatorial heat transport. We describe a CEC that is weaker than the one proposed by Schneider, compensated for by an increase in its gross stability owing to its cooler subsurface branch. We propose a more physically consistent way to estimate the value of F_O/F_A and its damping of ITCZ shifts below, separately estimating the cross-equatorial mass transports and gross stabilities of the atmosphere and ocean.

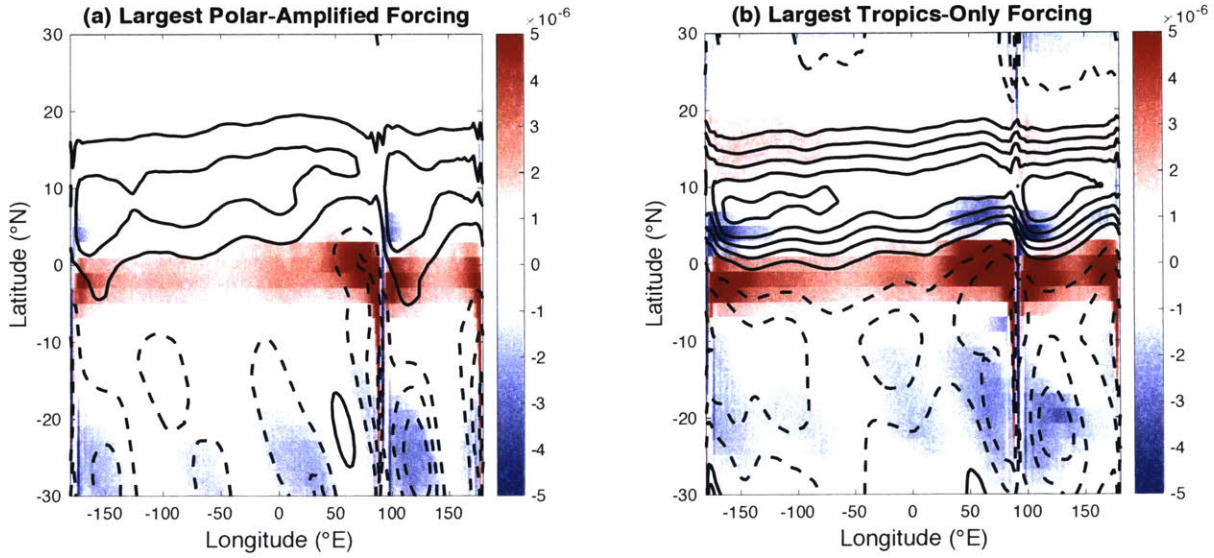

Figure 4.14. Vertical motion in the atmosphere and ocean in the fully coupled model for the highest amplitude (a) polar-amplified and (b) tropics-only forcing cases. Colors indicate annual mean vertical velocity (m s^{-1}) at 55 m depth in the ocean. Contours indicate vertical mean, annual mean pressure velocity in the atmosphere, with negative values and ascent shown as solid contours, and positive values and descent shown as dashed contours. The contour interval is 0.01 Pa s^{-1}, and the zero contour is not shown.

4.6. Summary and Estimates of ITCZ Shifts on Earth

For a range of forcing amplitudes and distributions designed to shift the ITCZ in an aquaplanet GCM, we find the shifts are always damped in a model configuration that includes an active ocean circulation relative to a configuration where it is passive, "sticking" the ITCZ to latitudes near the equator. The magnitude of the damping has a weak dependence on the forcing amplitude, decreasing as the amplitude increases, and is strongly affected by the forcing distribution, decreasing when the forcing is confined to the tropics. The reason the ITCZ shifts in the active ocean circulation cases are damped can be diagnosed from the hemispheric energy balance, with the largest contribution coming from the ocean's anomalous cross-equatorial heat transport. This heat transport acts to reduce the interhemispheric heating contrast imposed on the atmosphere and reduces the fraction of the original forcing it must compensate by transporting energy across the equator.

A robust feature of the anomalous ocean circulation is a cross-equatorial cell confined to the thermocline, coupled to the Hadley cells above by the surface zonal wind stress. These CECs have the same features in GM17: for a northward ITCZ shift, warm water transported southward across the equator is pumped into the thermocline at cooler temperatures in the southern hemisphere, returning northward across the equator in a western boundary current. The resulting cross-equatorial energy transport is southward, opposing the original heating of the northern hemisphere relative to the southern. Independent of the details of the subsurface ocean circulation, the energy transported across the equator by the CEC can be estimated from its surface properties, with its strength set by the surface zonal wind stress distribution and its gross stability set by the meridional SST gradient.

Secondary impacts on the ITCZ position by the CEC arise from the distribution of its energy transport. If the distribution of the interhemispheric heating contrast is concentrated at higher latitudes, its mismatch with the CEC's heat transport convergence distribution leads to an altered "net heating" profile of atmospheric heating. Combined with a spatial pattern of radiative feedbacks, the relative contributions of radiative fluxes and atmospheric cross-equatorial energy transport to balancing the net heating changes which leads to a further damping of the ITCZ shift. Radiative feedbacks in simulations of global warming using comprehensive GCMs are, like in our model, relatively positive equatorward of 30 ° latitude (Zelinka and Hartmann 2012), and their interaction with the CEC's heat transport would likely also contribute to the damping of ITCZ shifts on Earth. The CEC can also alter the relationship between the ITCZ position and the atmosphere's cross-equatorial energy transport, but the mechanism by which it does this depends on the metric used to define the ITCZ position. Using a centroid metric based on area-weighting the zonal mean tropical rainfall distribution, we find a robust reduction in subtropical precipitation in the fully coupled model runs relative to the slab ocean runs. If the energy flux equator is used to locate the ITCZ, the structure of the surface branch of the CEC always results in an anomalous heating of the atmosphere between the equator and the ITCZ, reducing the amount it shifts for a given atmospheric cross-equatorial energy transport anomaly. Both metrics predict a damping of the ITCZ shift in our model.

A strong control on the efficacy of the CEC and its cross-equatorial heat transport is the distribution of the interhemispheric heating contrast. For polar-amplified distributions, the gross stability of the CEC is set by the SST difference between the equator and the latitude of the surface westerly jet in the cooled hemisphere; if the heating distribution is confined to the tropics, the CEC is narrowed and its gross stability is reduced by 20-37 % depending on the

forcing amplitude. In the case of tropics-only forcing, the narrower CEC aligns with the anomalous Hadley cell, which responds directly to the heating distribution. For polar-amplified forcing distributions, the CEC is considerably wider than the bulk of the atmospheric streamfunction anomalies (compare Figure 4.5c to Figure 4.8a), which occur north of 15 °S, and result in a CEC whose width is set by extratropical rather than tropical dynamics. In all of our experiments, and those of GM17, a polar-amplified heating contrast results in a southward shift of the SH surface westerly jet, and for all but the highest forcing amplitude case here, the NH jet is shifted to the south as well. Year-to-year shifts in the annual mean position of the tropospheric westerly jet in the fully coupled model's control run are, like the polar-amplified forcing runs, associated with polar-amplified temperature anomalies and are dominant modes of the model's interannual variability (not shown). The extratropical zonal wind anomalies in the polar-amplified forcing runs, extending from the tropopause to the surface, have a similar vertical structure as the model's unforced variability; we interpret the westerly jet shifts in the forced runs as resulting from the projection of the polar-amplified forcing distribution onto a mode of natural variability in the model (Ring and Plumb 2008).

Though our experiments were performed using an idealized GCM, the energy balance framework we propose can be used to estimate the ocean's impact on ITCZ shifts on Earth. The largest impact the ocean has on ITCZ shifts in our simulations, quantified in Eq. (4.3), is through the ratio of its cross-equatorial energy transport to the atmosphere's, F_O/F_A, which is the product of mass transport, gross stability, and heat capacity ratios (Eq. 4.4). Figure 4.8b indicates that, if the torque exerted on the atmosphere by the surface wind stress balances the Hadley cells' divergence of angular momentum, the ratio ψ_O/ψ_A can be estimated from seasonal cycle of the Hadley cell's angular momentum balance.

Performing the same analysis on ERA-Interim reanalysis (Dee et al. 2011) over the period 1979-2016 as was done for our model in Figure 4.8b, this balance approximately holds in the Earth's tropics from 3-9 ° latitude (Figure 4.15a; the results are not strongly sensitive to the chosen tropical latitude range). A least-squares fit of the monthly mean climatologies shows that 91 % of the hemispherically asymmetric torque exerted by the zonal wind stress is balanced by the Hadley cells' hemispherically asymmetric angular momentum transport divergence. Not all of the surface zonal wind stress occurs over the ocean, however, since roughly 75 % of the tropical surface is covered by land. Of the total wind stress torque, 70 % occurs over the ocean, nearly in agreement with the land fraction. It is this wind stress over the ocean that would drive the type of oceanic CEC described here and in GM17.

Converting the hemispherically asymmetric wind stress into a cross-equatorial Ekman transport (as was done for the Ekman mass transport in Figure 4.7a), we compare it against the strength of the atmosphere's cross-equatorial mass transport in Figure 4.15b. Again performing a least-squares fit of the monthly mean climatology, the strength of the Ekman transport over the ocean is 28 % of the atmosphere's mass transport, giving a ratio ψ_O/ψ_A of 0.28. This ratio is similar to the 0.25 estimated over the seasonal cycle of our model's control run (red star, Figure 4.7a).

Though the atmospheric and oceanic mass transports are coupled by the atmosphere's angular momentum balance and the surface wind stress, the gross stabilities must be estimated separately. As was shown in Section 4.4, the ocean's gross stability is sensitive to the distribution of the interhemispheric forcing, so we must assume a latitude at which the water forming the lower branch of the CEC is pumped into the thermocline. Likely forcing agents of ITCZ shifts on Earth, such as changes in ice cover or in the strength of the AMOC, are concentrated at higher

latitudes, so we estimate the gross stability of the CEC as set by the meridional SST contrast between the equator and the latitude of the surface westerly jet, roughly 15 K. A fit of the seasonal cycle of the atmosphere's cross-equatorial energy transport gives a fairly constant gross stability of 14 K (Donohoe et al. 2013). Combined with the two fluids' heat capacities, this gives a ratio of the ocean's to the atmosphere's energy transports of 1.2. That is, for an ITCZ shift on Earth, we estimate an anomalous CEC would transport 20 % more energy across the equator than the atmosphere.

The ratio of the energy transports can be converted to a damping factor for ITCZ shifts by using Eq. (4.3). If changes in LW/F_A due to the CEC's heat transport are neglected, a slab compensation C_S of 0.8, typical for an extratropical or high-latitude forcing, gives a value of 0.25 for LW/F_A from Eq. (4.5c). If the slope b is taken as a constant, the ratio of the resulting ITCZ shifts from Eq. (4.3b) for a case where F_O/F_A is 1.2 to a case where it is zero is 0.51, giving a damping factor of 2.0. By neglecting changes in LW/F_A and b, both of which act to further damp the ITCZ shift in our model for polar-amplified forcing, this estimate of the damping factor might be conservative. It is clear, though, that to accurately simulate or predict the response of the ITCZ to an interhemispheric heating contrast, the impact of the tropical wind-driven circulation and its heat transport must be taken into account.

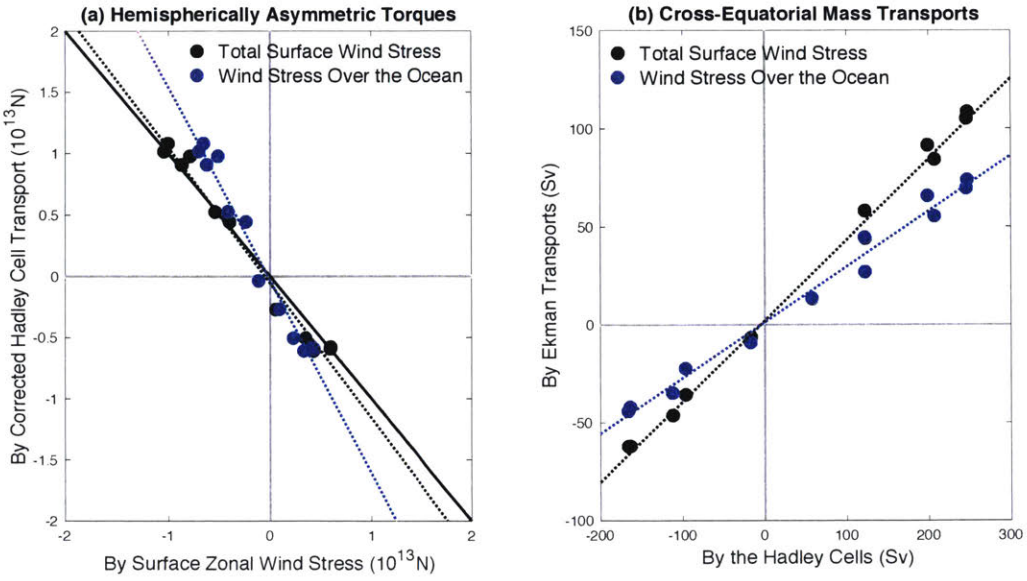

Figure 4.15. Monthly mean climatologies of atmosphere-ocean coupling on Earth using ERA-Interim reanalysis from 1979-2016. (a) Hemispherically asymmetric torques, as in Figure 4.8b, averaged from 3-9 ° latitude. (b) Northward Ekman transport in the surface ocean, as in Figure 4.7a and averaged between 3-9 °N and 3-9 °S, versus the strength of the atmospheric overturning circulation at the equator. In both panels, the dashed lines are linear least-squares fits of monthly mean climatologies.

Chapter 5

The Impact of the Ocean Circulation on Hadley Cell Strength in a Fully Coupled Aquaplanet GCM

The impact of the ocean circulation and its heat transport on the strength of the Hadley cells is studied in a fully coupled atmosphere-ocean global climate model (GCM) across a wide range of climates. By varying the reference longwave optical thickness in the model's gray radiation scheme by a factor of eight across the simulations, we simulate climates with global mean sea surface temperatures ranging between -5 and 35 °C. Comparing the fully coupled model runs to simulations with a passive "slab" ocean, we find that poleward heat transport by the ocean's subtropical cells significantly weaken the Hadley circulation across the whole range of optical thicknesses. The weakening is largest, about 70 %, in cold climates, reducing to about 30 % in warm climates. Cooling the tropics relative to the subtropics, the subtropical cells act to reduce the heating contrast across the Hadley cell, weakening the strength of the circulation. This weakening in our simulations is larger than in previous studies due to mixing at the poleward edge of the subtropical cell acting to increase its gross stability. Energy fluxes by atmospheric eddies act to oppose the reduction in the cross-Hadley cell heating contrast, transporting anomalous near-surface moist static energy downgradient toward the equator. In simulations that include horizontally circulating ocean gyres, the Hadley cell is strengthened relative to simulations without them, primarily due to a reduction in the strength and heat transport of the subtropical cells. Fluxes of angular momentum by atmospheric eddies plays a role in the warmer

simulations and is sensitive to the distribution of the zonal mean zonal winds in the middle and upper troposphere, further weakening the Hadley cells in the fully coupled runs. The leading-order impact of the ocean circulation on the strength of the Hadley cell, and its implications for a warming climate, are discussed.

5.1. Introduction

The Hadley cells are the largest north-south atmospheric circulations on Earth, coupling the climates of the tropics and subtropics. Ranging from roughly 30 °S to 30 °N, they cover half of Earth's surface area. High precipitation rates, peaking in the tropics, are tied to the cells' ascending branches, and subtropical dry zones are associated with descent along their poleward edges. These ascending and descending branches are connected by poleward-flowing air aloft and equatorward-flowing air at the surface, forming two overturning cells whose strengths are couple the climate of both regions.

Two frameworks spanning a wide range of circulation regimes have proven useful for understanding controls on the Hadley cells' strength. The first (Schneider 1977, Held and Hou 1980, Lindzen and Hou 1988, Plumb and Hou 1992) describes the cells as thermally direct in the inviscid, axisymmetric limit: the cells' upper, poleward-flowing branches conserve angular momentum and strengthen or weaken with the meridional heating contrast across each cell. Many different factors can affect the meridional heating contrast, and the strength of the Hadley cells in idealized climate simulations is sensitive to, among others, direct CO_2 forcing (Merlis 2015), El-Nino-like forcing (Tandon et al. 2013), and the heat transport of the tropical ocean (Levine and Schneider 2011). The second framework proposes that fluxes of angular momentum by eddies originating in the extratropics are important in the momentum balance of the upper

branch (Walker and Schneider 2006), and that the Hadley cells' strength responds linearly to the divergence of these fluxes. Eddy momentum fluxes have been shown to modulate, for example, interannual variations in the strength of the Hadley cells in reanalysis (Caballero 2007), and the strength of the summer cell and the transition to a monsoonal circulation in simulations using an idealized climate model (Bordoni and Schneider 2008, Schneider and Bordoni 2008).

Tying these two frameworks together is the zonal momentum balance of the Hadley cells' upper branch where, in a statistically steady state, the Coriolis acceleration on the poleward-flowing air is in an approximate balance with momentum advection by the zonal mean flow and the divergence of eddy momentum fluxes (e.g. Walker and Schneider 2006):

$$\bar{v}\left(f - \frac{\partial \bar{u}}{dy}\right) \approx S_e. \qquad (5.1)$$

Overbars indicate time and zonal averages, S_e is the eddy (motions departing from the time and zonal mean) momentum flux divergence, and f is the Coriolis parameter. This equation can be integrated vertically in pressure from the center of the Hadley cells to the tropopause to yield a "bulk Rossby number" Ro for the circulation (Levine and Schneider 2011).

$$\psi_{HC}(1 - Ro) = \psi_e \qquad (5.2a)$$

$$\psi_{HC} = \frac{2\pi a \cos\varphi_{HC}}{g} \int_0^{P_{HC}} \bar{v}\, dP \qquad (5.2b)$$

$$\psi_e = \frac{2\pi a \cos\varphi_{HC}}{fg} \int_0^{P_{HC}} S_e \, dP \qquad (5.2c)$$

where P_{HC} and φ_{HC} are the pressure and latitude of the center of the overturning streamfunction, a is the radius of the Earth, and g is the acceleration due to gravity. The vertically integrated mass transport, ψ_{HC}, is then the strength of the Hadley cell, ψ_e is the "eddy-driven" mass transport, and the bulk Rossby number measures the relative importance of the eddy momentum fluxes. If Ro is equal to one, eddy momentum fluxes have no impact on the strength of the circulation and the Hadley cells are in their angular momentum-conserving limit; if Ro equals zero, the circulation is entirely controlled by eddy momentum fluxes and the cells' strengths are linearly related to the divergence of those fluxes. For intermediate values of the Rossby number, such as for the Earth in the annual mean (~ 0.3, Levine and Schneider 2011), the strength of the Hadley cell is set by both the meridional heating contrast and the eddy momentum flux divergence. The bulk Rossby number, however, is not a fixed quantity, and changes in the strength of the circulation can be dominated by eddy momentum fluxes when Ro is large or by advection by the mean flow when Ro is small.

A clear-cut case where an altered meridional heating contrast drove large changes in Hadley circulation strength are the simulations of Levine and Schneider (2011; hereafter LS11). Using a three-dimensional atmospheric GCM, by coupling the atmosphere to an idealized representation of the ocean's subtropical cells (STCs; as in Klinger and Marotzke 2000), they found the Hadley cells were consistently weaker in simulations that included heat transport by the STCs. Coupled to the Hadley cells above by the easterly trade winds and their associated surface stresses, the STCs reduce the atmospheric heating contrast by transporting warm tropical surface water poleward and by upwelling at the equator cooler water subducted in the subtropics.

In the deep tropics, the STCs are able to transport heat poleward more efficiently than the Hadley cells owing to the relatively high stratification of the tropical ocean (Held 2001, Czaja and Marshall 2006). In this way the STCs cool the ascending branch of the Hadley cells and heat their descending branches, reducing the heating contrast.

The results of LS11 raise several questions about the impact of the ocean circulation on the strength of the Hadley cells. First, can other components of the climate system, such as radiative fluxes, offset some of the heating contrast changes resulting from the ocean's heat transport? Can horizontally circulating ocean gyres impact the Hadley cells' strength through their heat transport? And do simple representations of ocean heat transport of the type employed in LS11 adequately capture the impact of the STCs on the Hadley cells?

To address these questions, we run an aquaplanet global climate model (GCM), described in Section 5.2, with and without a fully coupled ocean circulation. The ocean circulation model is run either without vertical barriers to the flow, or with one pole-to-pole barrier that creates large gyres. The model is then run across a large range of global mean surface temperatures, similar to LS11, and differences between runs with and without active ocean circulations are compared in Section 5.3. We find that, like LS11, the ocean circulation always acts to weaken the Hadley cells, though it is more efficient at doing so in our runs. We also find that heat transport by atmospheric eddies partially offsets the effects of ocean heat transport, which we quantify in an energetic framework in Section 5.4. The energetic framework ties the energy transport by the Hadley cells to their strength, and it is shown that the ocean circulation increases the Hadley cell's gross stability, contributing to the reduction in their strength. The effects of eddy momentum fluxes on Hadley cell strength, which are sensitive to the distribution of the zonal winds in the upper troposphere, are described in Section 5.5. Our results are summarized in

Section 5.6, where we compare them to those in LS11 and discuss their relevance to Earth's Hadley cells under global warming scenarios.

5.2. Model Setup and Design of Experiments

We use a coupled atmosphere-ocean version of the MITgcm (Marshall et al. 1997a, b, 2004) in configurations with and without an active ocean circulation. The physics of both the atmospheric and oceanic components of the model, run on a cubed-sphere grid (Adcroft et al. 2004), are described in more detail in Green and Marshall (2017). To summarize, the atmospheric component of the model has 26 pressure levels and a modified version of the Frierson (2007) gray radiation scheme that includes a water vapor feedback on the longwave optical thickness (Byrne and O'Gorman 2013). The planetary albedo, equal to the surface albedo since there are no clouds or atmospheric absorption of shortwave radiation in our model, varies symmetrically from 0.2 at the equator to 0.6 at the poles. The model has a sponge layer that linearly damps winds above 43 hPa, preventing the subtropical westerly jets from extending to the top of the atmosphere. We run the model with a seasonal cycle of insolation for a circular orbit with a 360-day year at an obliquity of 23.45 °.

The model's surface is water-covered and run in three configurations: a stationary "Slab" ocean of constant depth, a fully coupled ocean circulation with an infinitesimally thin barrier running from the north to the south pole, and a fully coupled ocean circulation without that barrier. The fully coupled ocean configuration without the north-south barrier, designated "Aqua", has 15 vertical levels down to a depth of 3400 m and, without a barrier to interrupt the zonal flow, has an ocean circulation that is zonally symmetric in the long-term mean. When the north-south barrier is added in the "Ridge" configuration, the zonal flow is interrupted and

horizontally circulating gyres are created, similar to Enderton and Marshall (2009). The Slab ocean version of the model is run with a stationary layer of water with a constant depth of 25 m, chosen to be similar to tropical mixed layer depths in the fully coupled configurations. The Slab ocean's temperature is set by surface energy fluxes and does not have any "q-fluxes" meant to mimic ocean heat transport. Neither the Slab nor the fully coupled ocean models form sea ice once SSTs drop below freezing, eliminating the sea ice albedo feedback; the fully coupled model extrapolates the equation of state of seawater (Jackett and McDougall 1995) below the freezing point.

To vary the climate of the model, the reference longwave optical thickness is increased and reduced from its reference value to alternately warm and cool the climate from a configuration that is similar to present-day Earth. Eight experiments, multiplying the background optical thickness (the variable a in Byrne and O'Gorman 2013 Eq. 4) by 0.25, 0.50, 0.75, 1.00, 1.25, 1.50, 1.75, and 2.00 yield climates with global mean sea surface temperatures (SSTs) that range from roughly -5 to 35 °C. For optical thicknesses and warmer climates than those presented here, drag on the zonal winds in the sponge layer plays a non-negligible role in the momentum balance of Eq. (5.1), strengthening the Hadley cells in an unphysical way. Similar experiments were conducted in LS11 for global mean SSTs ranging from about -10-45 °C; their model does not have a sponge layer, allowing them to run it into warmer climates.

Each value of the longwave thickness multiplier is run in the Slab, Aqua, and Ridge configurations, yielding 24 experiments total. After being spun up to a state of statistical equilibrium, each experiment is run for a further 100 years, and results are averaged over that period to generate monthly climatologies which are averaged into an annual mean. The seasonal cycle of the Hadley cell in our model is similar to that described in Dima and Wallace (2003) – a

smoothly varying cross-equatorial cell is projected on top of the annual mean circulation (not shown), implying that the annual mean Hadley cell is not the average of the solisticial seasons. Additionally, experiments were run for all three model configurations without a seasonal cycle using the annual mean distribution of insolation, at 0.50, 1.00, and 2.00 times the background optical thickness. Each of these nine runs' Hadley cells had strengths that were close to the annual mean of their seasonally varying counterparts and, since our conclusions are not changed by these runs, they are not included. Each run's annual mean results are also averaged between the hemispheres, reflecting the hemispheric symmetry of the model configurations. The Aqua and Ridge experiments are spun up the longest, up to 2000 years, to reach a point without any detectable trends in global mean SSTs or the circulation strengths and energy transports of the atmosphere and ocean. There are still trends in deep ocean temperatures in the warmer runs, peaking at the ocean bottom at 0.6 °C per century in the warmest Aqua case; they nearly vanish in the upper kilometer. Every Slab experiment is spun up for only 200 years, reaching statistical equilibrium faster than their fully coupled counterparts due to the relatively low heat capacity of the 25 m-thick ocean.

5.3. Changes in the Circulation with Climate

5.3.1. The Strengths of the Hadley Cell and the Eddy Momentum Flux Divergence

The Hadley cell is weaker in the fully coupled runs for all values of the longwave optical thickness (Figure 5.1). This weakening is most pronounced in the coldest runs (top row), reducing slightly for the reference run (middle row) and the warmest run (bottom row). For these

three climates, the Hadley cell is also slightly stronger in the Ridge configuration as compared to Aqua. There are similarities in the three models' Hadley cells, though: as the climate warms, all three configurations show similar monotonic expansions in height of the Hadley cell and in the latitude of its poleward edge. This northward expansion comes at the expense of the mid-latitude Ferrell cell, which weakens significantly. A notable difference in the structure of the Hadley cell between the fully coupled and Slab cases is in the coldest set of runs, where both the Aqua and Ridge configurations have a counter-rotating cell in the deep tropics. Cooling of the equatorial atmosphere by the ocean's heat transport divergence (100 and 88 W/m^2 for Aqua and Ridge, respectively) is stronger than the net heating by radiation at the top of the atmosphere (63 and 65 W/m^2) in these runs, forcing the atmosphere to converge energy there and driving time mean descent (see Bischoff and Schneider 2016).

The eddy momentum flux divergence (solid gray contours) peaks in the subtropics and is consistently higher in the Slab runs than in Aqua or Ridge. Its latitude is roughly constant with climate and between the models which, since the Hadley cell expands as the climate warms, results in it moving from near the subtropical edge of the cell in the coldest climate to near the cell center in the warmest. As the Hadley cell expands, the location of the zero contour of the zonal mean zonal wind (black line) shifts poleward as well, forcing the waves responsible for the momentum fluxes to break at lower pressures and squeezing the divergence of the flux to a smaller region near the tropopause.

We quantify the relative importance of the eddy momentum flux divergence on the strength of the Hadley cell across climates and models by returning to the zonal momentum balance of Eq. (5.2). The center of the Hadley cell (φ_{HC} and P_{HC}) is defined as the latitude of the maximum streamfunction value at the model pressure level halfway between the surface and

where the streamfunction decreases below 5 Sv (1 Sv = 10^9 kg s^{-1}) and is indicated by asterisks in Figure 5.1. We use a flexible definition for P_{HC}, rather than a fixed value, to allow for the upward expansion of the cell as the climate warms. The strength of the Hadley cell, ψ_{HC}, is then equal to the streamfunction value at that location, giving a bulk measure of the strength of the cell without tracking local maxima like those seen near the tropopause in the warmest runs. The eddy-driven mass transport, ψ_e, is calculated following Eq. (5.2c) and the bulk Rossby number Ro is backed out from Eq. (5.2a). Values for the Hadley cell strength, the eddy-driven mass transport, and the bulk Rossby for each model are shown in Figure 5.2a, b, and c respectively.

In agreement with Figure 5.1, the Hadley cell is always weaker in the fully coupled runs, for both the ψ_{HC} metric (solid lines with markers) and the maximum of the overturning streamfunction (dashed lines). For the coldest runs, ψ_{HC} is 73 and 67 % weaker in Aqua and Ridge respectively, reducing to 34 and 31 % weaker for the second-warmest case. As the climate warms, the Slab ocean runs' Hadley cell weakens by more than half, from 196 Sv to 92 Sv, but the Aqua and Ridge runs' cells stay almost constant in strength, varying by 13 Sv or less. Compared to the large differences in ψ_{HC} between the fully coupled and Slab runs, the eddy-driven mass transports (Figure 5.2b) are similar between the three model configurations, with ψ_e generally higher in the Slab runs. As a result, the bulk Rossby numbers are higher in the Slab runs (Figure 5.2c), indicating a more thermally-driven regime, than in the fully coupled runs, whose lower Rossby numbers indicate a more mechanically-driven regime. Because the differences in ψ_e between the fully coupled runs and the Slab runs are smaller than the differences in ψ_{HC}, we attribute the weakening of the Hadley cells in the fully coupled runs primarily to a reduction in the heating contrast across the cell, rather than to a reduction in the eddy momentum flux divergence.

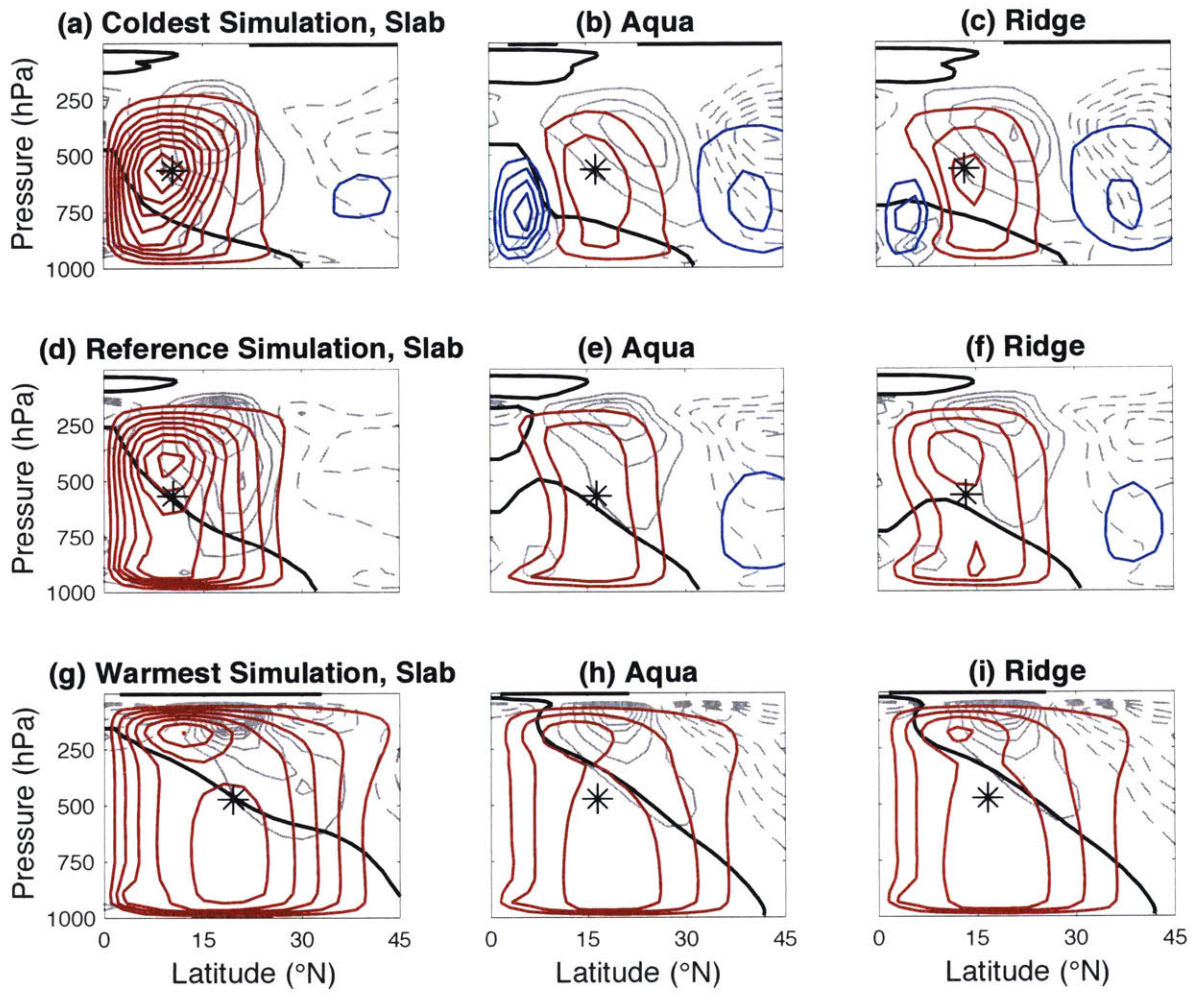

Figure 5.1. Atmospheric mass transport overturning streamfunction. Color contours indicate clockwise (red) and counter-clockwise (blue) rotation. Contour interval: 20 Sv, and the zero contour is not shown. The black contour is the zero contour of the zonal mean zonal wind. Grey contours indicate the positive (solid) and negative (dashed) northward eddy momentum flux divergence. Contour interval: 5×10^{-6} m s^{-2}, and the zero contour is not shown. Asterisks indicate the location of the center of the Hadley cell, where the streamfunction is read to define the strength of the cell (ψ_{HC}).

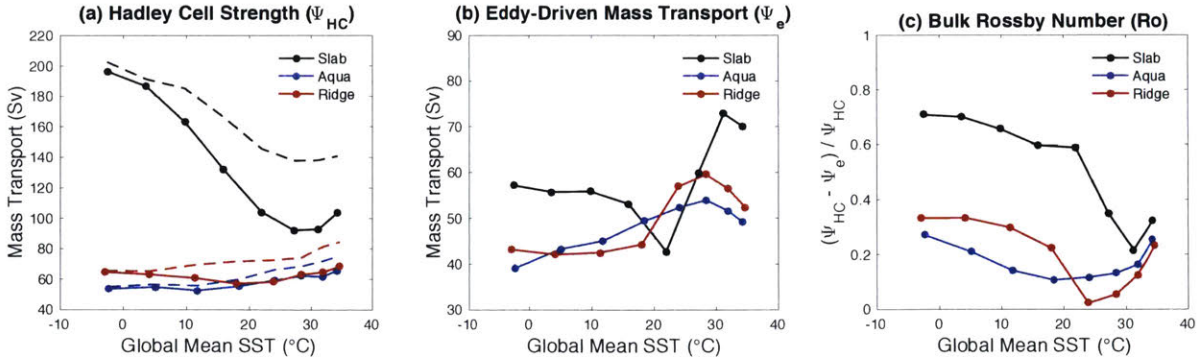

Figure 5.2. The Hadley cell's momentum balance. (a) The strength of the Hadley cell. Solid lines with symbols indicate values of the mass transport of the mass transport streamfunction at the cell's center (ψ_{HC}), and dashed lines show streamfunction maxima. (b) The northward mass transport of the cell's upper branch driven by eddy momentum flux divergence. (c) The cell's bulk Rossby number.

5.3.2. The Ocean Circulation and its Impact on SSTs

Both the Aqua and Ridge configurations have oceanic subtropical cells which overturn in the same sense as the Hadley cells above (Figure 5.3), with warm surface water flowing poleward and cooler subsurface water returning equatorward. The left column of Figure 5.3 shows the zonal mean Eulerian streamfunction in the Aqua runs, calculated in the same manner using the meridional velocity as the atmospheric streamfunctions shown in Figure 5.1. In these Aqua cases, the Eulerian streamfunction describing the STC extends all the way down to the sea floor. As discussed in Marshall et al. (2007), this is because bottom stress acts to balance the surface stress that drives the circulation. Parametrized small-scale lateral mixing of momentum in the ocean's interior diffuses some of the surface stress, and the near-bottom branch of the STCs are not quite as strong as their surface branches. In the Ridge cases, the north-south ridge breaks up

the zonal symmetry, mixing in western boundary currents helps to balance the surface stress, and the Eulerian mean does not extend to the bottom (not shown).

Baroclinic eddies and their associated mass transports significantly modify the subsurface ocean circulation and the structure of the STCs. Defined as the sum of the Eulerian mean and eddy-induced circulations, the residual mean circulation (Marshall and Radko 2003) is shown for the Aqua and Ridge runs in the middle and right columns of Figure 5.3. Acting on tilted isopycnals, the Gent-McWilliams/Redi scheme (Griffies 1998) employed in this version of the MITgcm produces an eddy-induced circulation that acts to reduce the isopycnal slope and overturns in the opposite sense as the Eulerian mean circulation. The resulting residual mean circulation – the sum of the Eulerian mean and the eddy-induced circulations – is confined to the thermocline and describes STCs whose subsurface branch approximately conserves temperature as it flows equatorward. At the surface, the strength of the residual circulation is equal to the Eulerian mean and is set by the strength of the surface zonal wind stress.

For both the Aqua and Ridge cases, the STC expands with the Hadley cell as the climate warms. They also strengthen with the near-surface branch of the Hadley cell, with the Aqua STC's strength, increasing from 55 Sv in the coldest case to 71 Sv in the warmest case, closely matching its atmospheric counterpart and the Ekman mass transport associated with the surface zonal wind stress. The STC in the Ridge runs, due to the presence of zonal mean zonal pressure gradients associated with the north-south barrier, is weaker than the near-surface branch of the Hadley cell and the Ekman transport. The zonal mean zonal pressure gradients produce geostrophic transport in the surface layer that opposes the Ekman transport, weakening the STC (McCreary and Lu 1994). This effect becomes more pronounced as the STC expands; the cell's

mass transport is 64 Sv in the warmest run, 14 % weaker than the atmospheric streamfunction at 900 hPa.

By blocking the zonal flow, the north-south barrier in the Ridge runs sets up horizontally circulating gyres (Figure 5.4), separated by maxima in minima in the zonal wind stress (not shown). Counter-clockwise-rotating tropical gyres are bound by the equator and the latitude of peak trade wind strength, clockwise-rotating subtropical gyres extend from the latitude of the peak trade wind strength to the peak westerly surface winds, and so on for the subpolar and polar gyres. The gyres transport heat by acting on east-west temperature gradients. For example, the subtropical gyre transports heat poleward because its northward-flowing western boundary current, whose waters originate at the equatorward boundary of the gyre, is warmer than the equatorward flow in the interior of the basin. The tropical and subtropical gyres overlap with the STCs; their boundary marks the location of the peak trade wind strength and STC mass transport, and the poleward edge of the STCs approximately lines up with the location of the subtropical gyres' peak mass transport. From the coldest to the warmest runs, the tropical gyres strengthen, from 24 to 66 Sv, while the subpolar gyres weaken, from 94 to 34 Sv. The strength of the subtropical gyres does not significantly change: it is 91, 89, and 96 Sv in the coldest, reference, and warmest runs respectively.

A consistent effect of the ocean circulation and its heat transport is to reduce the tropical-subtropical SST contrast relative to the Slab runs (Figure 5.5). Poleward ocean heat transport peaks between 15 and 20 ° latitude for every Aqua and Ridge run, cooling equatorward latitudes and heating poleward latitudes. Ocean heat transport between 15 and 20 ° is dominated by the STCs, which are stronger and have large cross-cell temperature contrasts at those latitudes than the gyres. The background meridional SST gradient is largest in the coldest runs, as is the

magnitude of the equatorial cooling in the fully coupled runs, reflecting the equatorial upwelling of subtropical water with the largest temperature difference to the tropical surface. As the climate warms and the meridional SST gradient is reduced, this equatorial cooling also reduces.

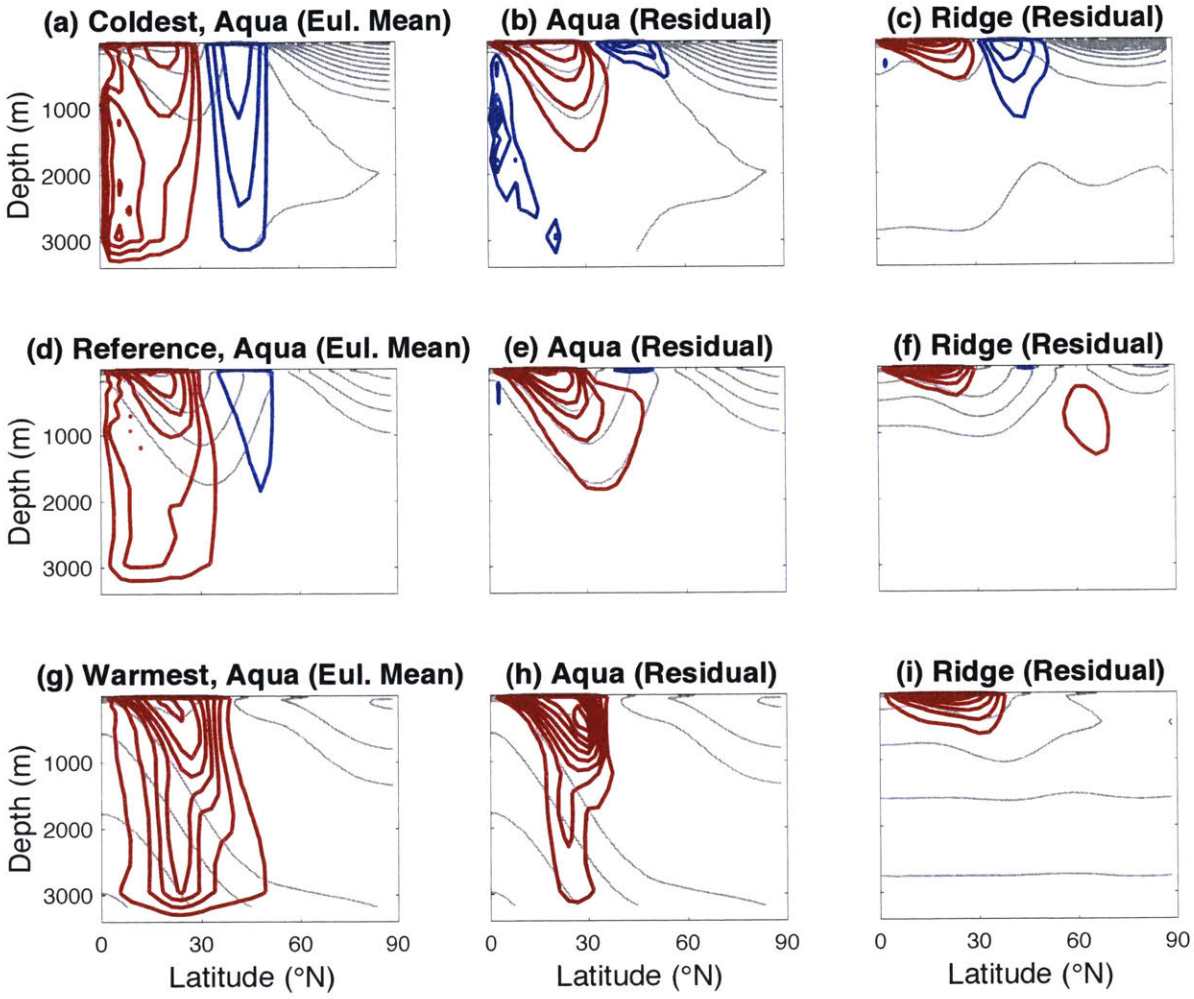

Figure 5.3. Oceanic overturning streamfunction. Color contours indicate clockwise (red) and counter-clockwise (blue) rotation. The left column shows the Eulerian mean streamfunction of Aqua runs; the middle and right columns show the residual mean streamfunction of Aqua and Ridge runs, respectively. Contour interval: 10 Sv, and the zero contour is not shown. Grey contours indicate the zonal mean temperature. Contour interval: 5 °C.

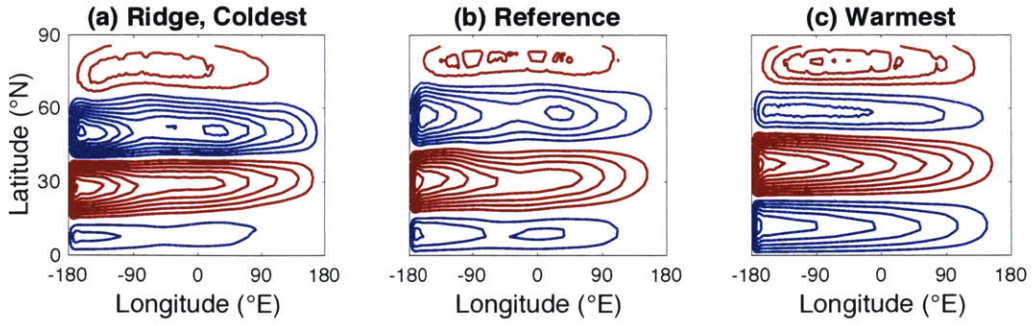

Figure 5.4. Vertically integrated mass transport streamfunction for Ridge runs. Red contours indicate clockwise rotation, and blue contours indicate counter-clockwise rotation. Contour interval: 10 Sv, and the zero contour is not shown.

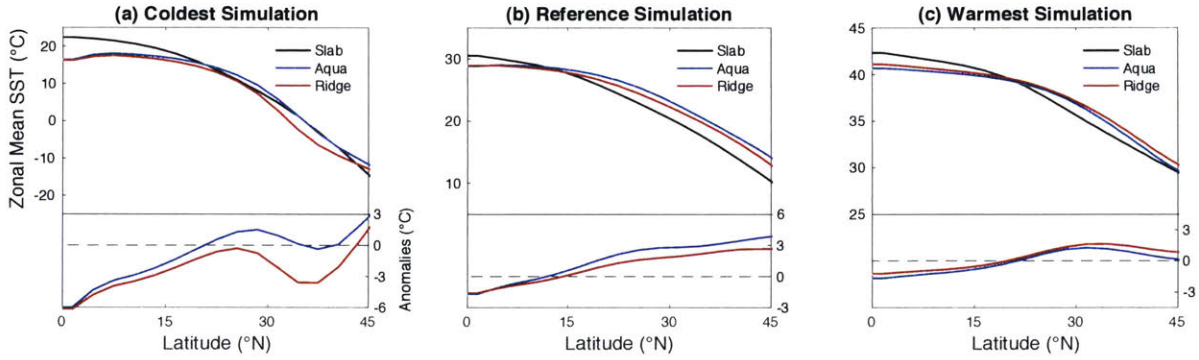

Figure 5.5. Zonal mean sea surface temperature. Top panels indicate zonal mean SSTs, and bottom panels indicate departures from Slab runs for Aqua (blue) and Ridge (red).

5.4. The Cross-Cell Heating Contrast and the Role of Ocean Heat Transport

5.4.1. Hadley Cell Energy Balance and Heating Contrast

With the addition of an active ocean circulation not affecting the atmosphere's eddy-driven mass transport as strongly as it weakens the Hadley cell's total mass transport, we turn to its impact on

the cell's heating contrast to explain the weakened circulation. In a steady state, the atmosphere's zonal mean energy balance represents a balance between divergent poleward energy transport by the atmosphere ($\nabla \cdot AHT$), heating by radiation (r), and heating by ocean poleward heat transport convergence ($-\nabla \cdot OHT$):

$$\nabla \cdot \left(AHT_{steady} + AHT_{eddies}\right) = r - \nabla \cdot OHT \qquad (5.3)$$

where the subscripts "steady" and "eddies" denote transport by the time mean, zonal mean circulation and by motions departing from that time and zonal mean. In the tropics, AHT_{steady} is equal to the energy transported by the Hadley cells. Equation 5.3 can be integrated over the Hadley cell's ascending branch, from the equator where the atmosphere's and ocean's poleward energy transports are zero in our hemispherically symmetric runs, to the latitude of the center of the cell (φ_{HC}). Solving for the Hadley cell's heat transport AHT_{HC} at that location,

$$AHT_{HC} = R_{asc} - (AHT_{eddies} + OHT)_{HC} \qquad (5.4a)$$

where R_{asc} is the integrated radiative heating over the ascending branch, and AHT_{eddies} and OHT are evaluated at φ_{HC}. Equation 5.4a represents an energy balance over the ascending branch of the Hadley cell: the cell must transport as much energy out of the tropics as is fluxed into the tropics by radiation, atmospheric eddies, and the ocean's circulation. Similarly, Eq. (5.3) can be integrated over the descending branch of the Hadley cell from φ_{HC} to its edge, defined as the latitude where the near-surface wind switches from easterly to westerly, where there is negligible heat transport by the steady atmospheric circulation:

$$AHT_{HC} = -R_{desc} + (AHT_{eddies} + OHT)_{edge} - (AHT_{eddies} + OHT)_{HC}. \qquad (5.4b)$$

Here, heating of the subtropics by the Hadley cell's energy transport is balanced by cooling by radiation and the divergence of eddy and ocean heat transports out of the region of the descending branch. Equations 5.4a and 5.4b can then be averaged to yield an equation for the heating contrast across the Hadley cell that balances AHT_{HC}:

$$AHT_{HC} = \frac{1}{2}(R_{asc} - R_{desc}) + \left(\frac{1}{2}AHT_{eddies,edge} - AHT_{eddies,HC}\right) + \left(\frac{1}{2}OHT_{edge} - OHT_{HC}\right)$$

$$= \Delta R + \Delta AHT_{eddies} + \Delta OHT. \qquad (5.5)$$

The strength of the Hadley cell's energy transport increases linearly in Eq. (5.5) with the heating contrast across the cell by radiation, atmospheric eddies, and the ocean heat transport. For example, if the equator-to-pole albedo contrast was increased and ΔR grew, all else being equal, the Hadley cell would be expected to strengthen and transport more energy poleward. We will argue that the Hadley cell is weakened by the distribution of the ocean's heat transport, resulting in negative values of ΔOHT and reducing the demands on the Hadley cell's heat transport.

To compare the Slab runs to the fully coupled runs, at a given multiplier of the reference longwave optical thickness, we evaluate the terms in Equation 5.5 at their latitudes in the Slab runs. We use the same latitudes across the three model configurations to avoid attributing changes in the radiative heating contrast to the net heating by shortwave radiation, which is fixed in our model and has a strong dependence on latitude. Our results are not sensitive to the choice

of reference model configuration, changing only slightly if the latitudes in the Aqua runs are used instead.

Differences in the heating contrast terms of Equation 5.5 between the fully coupled and Slab runs, and between Ridge and Aqua runs, are shown in Figure 5.6. Across all climates, the energy transport by the Hadley cell is reduced by about 1 PW (10^{15} W) in the fully coupled runs (Figure 5.6a, b). This reflects a reduced heating contrast across the cell by the same amount, where the roughly 2 PW heating contrast reduction due to the ocean's heat transport is partially compensated by the roughly 1 PW increase in the contrast due to energy transport by atmospheric eddies. With the model's distribution of absorbed shortwave radiation fixed and comparatively weak gradients in the longwave radiation, changes in the radiative heating contrast are small. The Hadley cell's energy transport is slightly stronger in the Ridge runs compared to Aqua (Figure 5.6c), again reflecting a change in ΔOHT that is partially compensated by atmospheric eddies. There is a dependence in those two terms on the global mean SST that is absent in Figures 5.6a and 5.6b, but the changes in AHT_{HC} do not shown the same dependence. Consistent between both the Ridge and Aqua runs, and between the fully coupled and Slab runs, are changes in the Hadley cell's energy transport follow changes in the cell's heating contrast due to the ocean's heat transport, with energy transport by atmospheric eddies partially compensating.

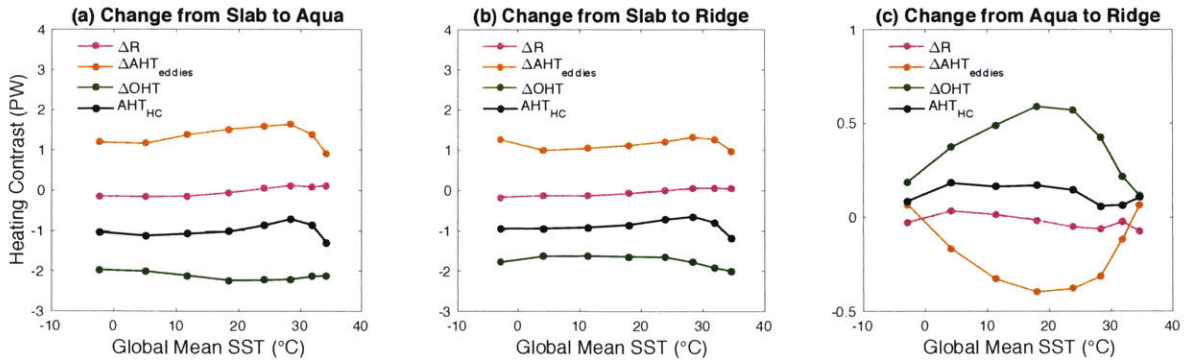

Figure 5.6. Contributions to changes in the Hadley cell heating contrast, following Eq. (5.5). (a, b) Changes in heating contrast terms in the Aqua and Ridge runs, respectively, from the Slab runs. (c) Changes in Ridge runs relative to Aqua.

5.4.2. Ocean Heat Transport

The reduction of the heating contrast across the Hadley cell by ocean heat transport is primarily a result of the subtropical cell's poleward heat transport. Ocean heat transports at the edge of the ascending branch, OHT_{HC}, and at the edge of the Hadley cell, OHT_{edge}, are shown in Figure 5.7. For both Aqua and Ridge, OHT_{HC} is larger than OHT_{edge}, and is nearly constant with global mean SST. Lying around the latitude of the peak easterly surface wind stress, OHT_{HC} is associated with the meridionally overturning STCs. As discussed in Section 5.3.2, oceanic barotropic eddies act to oppose the Eulerian mean circulation in the Aqua runs, and the total ocean heat transport (solid blue line) is weaker than that of the Eulerian mean circulation (dashed blue line). In the Ridge runs, the effects of eddies are weak and the total values of OHT_{HC} nearly match that of the Eulerian mean circulation.

At the edge of the Hadley cell, poleward ocean heat transport out of the subtropics (red lines) acts in opposition to the ocean heat transport at the edge of the ascending branch. If

OHT_{edge} were zero, the contribution to the Hadley cell's heating contrast by the ocean circulation in Eq. (5.5) would be the negative of OHT_{HC} but, by cooling the cell's descending branch, OHT_{edge} reduces the magnitude of ΔOHT. Despite not having subtropical gyres, the Aqua runs have similar values of OHT_{edge} as the Ridge runs, with contributions by both the steady circulation (dashed red line, Figure 5.7a) and eddies (the difference between solid and dashed lines). Though the equatorward flow of the STC's subsurface branch conserves temperature, the streamfunction contours at the poleward edge of the STC in the Aqua runs bend poleward first as they descend (Figure 5.3b), resulting in a northward subsurface heat transport. In the Ridge runs, eddies again have a smaller effect on the heat transport compared to the Aqua runs, and OHT_{edge} is nearly equal to the steady heat transport by the subtropical gyres. The similarity between OHT_{edge} in the Ridge and Aqua runs means that reduced heat transport by the STCs in the Ridge runs is the main contributor to the smaller magnitude ΔOHT as compared to the Aqua runs (Figure 5.7c).

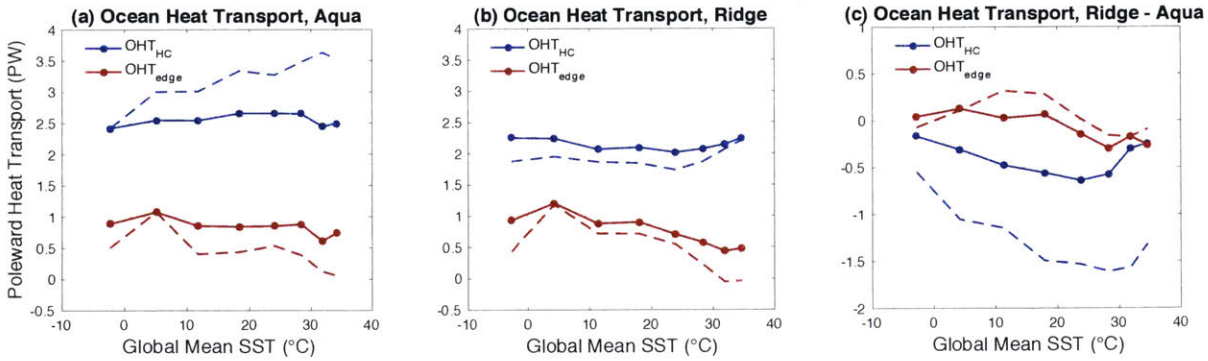

Figure 5.7. Ocean heat transport at the center (OHT_{HC}, blue) and poleward edge (OHT_{edge}, red) of the Hadley cell. Solid lines with circles indicate total (steady + eddy) transports, and dashed lines indicate transport by the steady circulation.

5.4.3. Heat Transport by Atmospheric Eddies

Energy transport by atmospheric eddies in our model runs is down the gradient of near-surface moist static energy. For both the Slab and fully coupled runs, eddy energy transport at the center of the Hadley cell increases as the climate warms (Figure 5.8a) and follows the contrast in near-surface moist static energy (MSE) between the ascending and descending branches (Figure 5.8b). Equal to the sum of the sensible heat, latent heat, and potential energy contents, the MSE of near-surface air in the ascending branch is warmer than in the descending branch because it is both warmer and has a higher specific humidity, leading to a positive MSE contrast across the Hadley cell. Eddy energy transport, peaking in the lower troposphere, can be thought of as diffusing MSE downgradient (e.g. Flannery 1984, Frierson et al. 2007), and approximately follows the MSE contrast across the Hadley cell. This is also true when comparing the model configurations, with the eddy heat transport and MSE contrast reduced in the fully coupled runs compared to the Slab runs, and with both slightly higher in Ridge than in Aqua.

Compensation by atmospheric eddies of the ocean's impact on the Hadley cell's heating contrast is then a passive response to ocean-driven changes in SST. Like ΔOHT, changes in ΔAHT_{eddies} between the fully coupled and Slab runs are primarily a result of energy transport anomalies at the center of the Hadley cell ($AHT_{eddies,HC}$ in Eq. (5.5)). The reduction in poleward eddy energy transport there increases the heating contrast across the cell, partially compensating for the addition of poleward ocean heat transport. As shown in Figure 5.5, ocean heat transport cools SSTs near the equator relative to the subtropics, reducing the SST contrast between the ascending and descending branches of the Hadley cell (Figure 5.8c). Without opposing changes in near-surface relative humidity, differences in the MSE contrast (Figure 5.8b) are similar to the differences in the SST contrast between both the fully coupled and Slab runs, and the Ridge and

Aqua runs. So, changes in the eddy energy transport can be thought of as a passive response to changes in the ocean heat transport: as ocean heat transport increases, it cools the tropics relative to the subtropics, causing same-sign changes in near-surface MSE which are then transported down-gradient by atmospheric eddies.

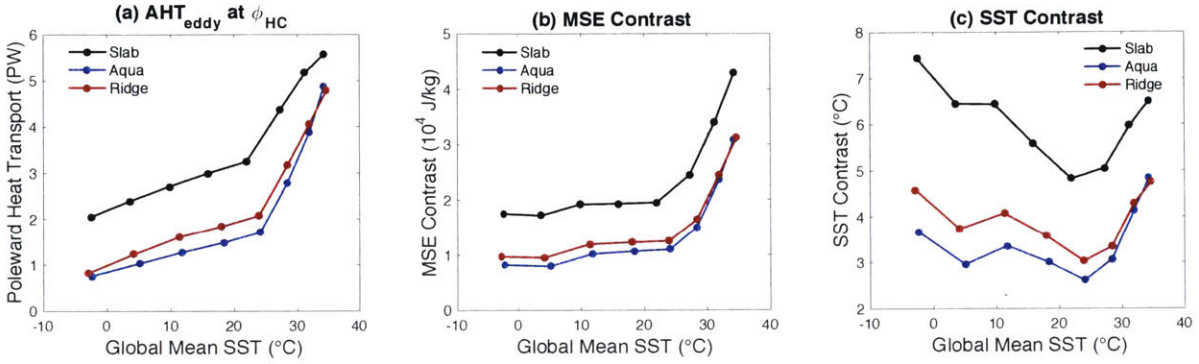

Figure 5.8. Conditions at the center of the Hadley cell. (a) Energy transport by atmospheric eddies ($AHT_{eddies,HC}$). (b) The difference in the area-averaged near-surface moist static energy between the regions of the ascending and descending branches of the Hadley cell, each of which are calculated by area-averaging the MSE of the first model level over their corresponding latitude range. (c) Same as (b) but for sea surface temperature.

5.4.4. The Relationship Between Hadley Cell Energy Transport and Mass Transport

The nearly constant reduction of the Hadley cell heating contrast across climates by the ocean circulation does not translate into a constant reduction of the strength of the Hadley cell, which decreases in magnitude as the climate warms (Figure 5.2a). Relating the two quantities is the gross stability (Held 2001, Czaja and Marshall 2006), equal to the energy transport (AHT_{HC})

divided by the mass transport (ψ_{HC}). The gross stability is a measure of the energy contrast between the circulation's upper and lower branches, with higher values indicating more energy transport (higher vertical energy contrast) for a given mass transport. Shown in Figure 5.9a, the gross stability of the Hadley cell in the Slab runs increases by 210 % from the coldest to the warmest climates (solid black line), more than twice its increase in the Aqua and Ridge runs (57 and 99 %, respectively).

Because the Hadley cell's gross stability increases away from the equator (e.g. Held 2001), its changes are difficult to attribute to the vertical energy contrast when the latitude of the cell's peak mass transport is changing. In the coldest runs, that latitude (φ_{HC}) is equatorward in the Slab runs compared to the fully coupled runs: 11 ° versus 17 ° for Aqua and 14 ° for Ridge. As the climate warms and edge of the ascent zone expands poleward, the differences in these latitudes between the three reduces, converging at the second-warmest simulations. When the Hadley cell's mass and energy transports in the Slab runs are read at φ_{HC} from the Aqua runs, both the Hadley cell strength and gross stability behave similarly to the fully coupled runs (dashed black lines, Figure 5.9a) and the differences between the two do not strongly change with global mean SST.

The relatively large weakening of the Hadley cell by the ocean circulation in cold climates is then largely due to a narrowing of the ascent region of the Hadley cell. The energy transport by the time mean, zonal mean circulation in the coldest Slab run is similar at the latitude of the peak mass transport for the Slab and fully coupled runs (Figure 5.9b) but, because the Hadley cell's gross stability is lower at 11 ° than it is at 14 ° or 17 °, the mass transport increase from the fully coupled to the slab runs is largest at 11°. As the climate warms, the Hadley cell's gross stability increases (by 200 % at 11 ° in the Slab runs), the Hadley cell is more

efficient at transporting energy in the tropics, and its mass transport peaks farther poleward (Figure 5.9c). We then interpret the large increase in the Slab run's Hadley cell strength in cold climates as follows: without ocean heat transport, the Hadley cell's energy transport is forced to increase. Since its gross stability is lower near the equator, the Hadley cell's mass transport must increase most strongly in the tropics, peaking further equatorward and narrowing the cell's ascent region.

Thermally-driven weakening of the Hadley cell by the ocean's heat transport can then be split into two contributions: widening of the ascending branch of the cell, which is most pronounced at cold climates, and a reduction in the cross-cell heating contrast, which is relatively invariant. The reduction of the cross-cell heating contrast results, necessarily, in a reduction of the poleward energy transport by the Hadley cell, which can be split into contributions by changes in the cell's mass transport and its gross stability. Comparing their values between the Slab and fully coupled runs at the latitude φ_{HC} in the Aqua runs (black dashed lines, Figure 5.9a), changes in both are fairly constant with global mean SST. Averaging across the runs, 69 % of the weakened energy transport in the Aqua runs is due to a reduction in the mass transport, 50 % is due to the reduced gross stability, and 19 % is offset by their nonlinear combination. For the Ridge runs, the split is similar: 64 %, 56 %, and 20 %, respectively. Reduced energy transport by the Hadley cell, driven by oceanic poleward heat transport partially compensated by energy transport by atmospheric eddies, is accomplished by reductions in both the cell's mass transport and its gross stability.

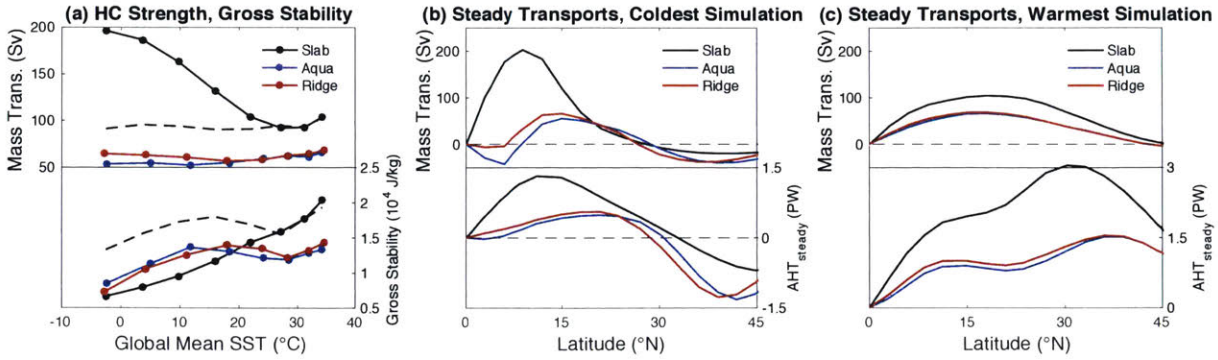

Figure 5.9. Hadley cell gross stability. (a) Hadley cell strength (ψ_{HC}, top) and gross stability (bottom). Dashed black lines indicate Slab values evaluated at the latitude of ψ_{HC} in comparable Aqua runs. (b) Strength of the mass transport streamfunction evaluated at the pressure of the middle of the Hadley cell (top) and the poleward energy transport by the time mean, zonal mean circulation (bottom) in the coldest run. (c) Same as (b), but for the warmest run.

5.5. The Effects of Eddy Momentum Fluxes

Changes in the eddy-driven Hadley cell mass transport between the three model configurations are generally small relative to the direct thermal forcing by the ocean circulation, but they are important for the warmest simulations. Half of the weakening between the Slab and fully coupled runs for the warmest case can be attributed to a reduced ψ_e, as can most of the difference between the Aqua and Ridge runs (Figure 5.2). Between the Slab and fully coupled runs, the reduced ψ_e is due to the redistribution of the eddy momentum flux divergence, rather than changes in the total eddy flux of momentum into the subtropics. The eddy momentum flux divergence (EMFD) has higher peak values in the Slab runs (Figure 5.10a), but its integral in pressure and latitude from the equator to the edge of the Hadley cell is nearly constant between the Aqua, Ridge, and Slab runs (Figure 5.10b). This can also be seen from Figure 5.1, where it is

clear that EMFD has higher maximum values in the Slab runs, but its distribution is generally narrower compared to Aqua or Ridge. The differences in the EMFD distributions then makes the calculation of ψ_e in Eq. (5.2c) sensitive to the latitude where it is calculated. If Slab runs' ψ_e is calculated at φ_{HC} from Aqua runs (poleward for the cooler runs), it is consistently stronger than the fully coupled runs' ψ_e (not shown).

The propagation and breaking of waves in the subtropics is coupled to the structure of the zonal wind, which is notably different in the fully coupled runs. The peak zonal mean zonal wind, corresponding to the strength of the subtropical jet at the poleward edge of the Hadley cell, is always weaker in the fully coupled runs (Figure 5.10c). With the Hadley cells having similar widths between Slab, Aqua, and Ridge runs, the meridional shear of the zonal wind ($\partial\bar{u}/\partial y$ in Eq. (5.1)) is then lower in the fully coupled runs. This result is consistent with the Slab runs' higher bulk Rossby numbers (Figure 5.2c), since Ro in Eq. (5.2a) is equal to the vertical integral of the shear divided by the Coriolis parameter. Consequently, the latitude range of the values of the zonal mean zonal wind where eddies originating in the extratropics break is broader in the fully coupled runs. We propose this is the reason the EMFD distribution is broader in Aqua and Ridge. That distribution of zonal mean zonal winds is also shifted poleward in the fully coupled runs (Figure 5.11), in thermal wind balance with the reduced meridional temperature gradient, leading to the reduced ψ_e at a given latitude relative to the Slab runs.

With both the strength of the subtropical jet and the integrated EMFD similar between the Ridge and Aqua runs (Figure 5.10b, c), the increased eddy-driven mass transport for warmer climates in the Ridge runs is a result of an equatorward shift of the EMFD distribution. Like the Slab runs relative to Aqua, the reduced heat transport by the subtropical cell in the Ridge runs results in an increased meridional temperature gradient in the center of the Hadley cell and an

equatorward shift of the 5 m s^{-1} zonal mean zonal wind line in the upper troposphere (Figure 5.11). This shifts the distribution of the EMFD equatorward and increases ψ_e. For colder runs, the Hadley cell's ascending branch is narrower in the Ridge runs for the same reason it is narrower in the Slab runs; if the Ridge runs' ψ_e is calculated at φ_{HC} from Aqua runs, it is stronger across the full range of global mean SST.

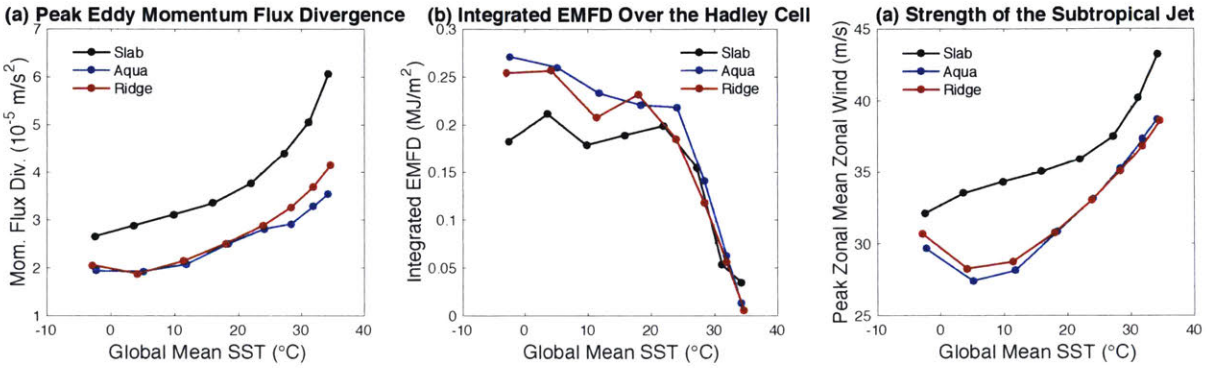

Figure 5.10. Eddy momentum flux divergence (EMFD) and the strength of the subtropical jet. (a) The peak EMFD. (b) EMFD integrated in pressure and latitude over the width of the Hadley cell. (c) The peak zonal mean zonal wind.

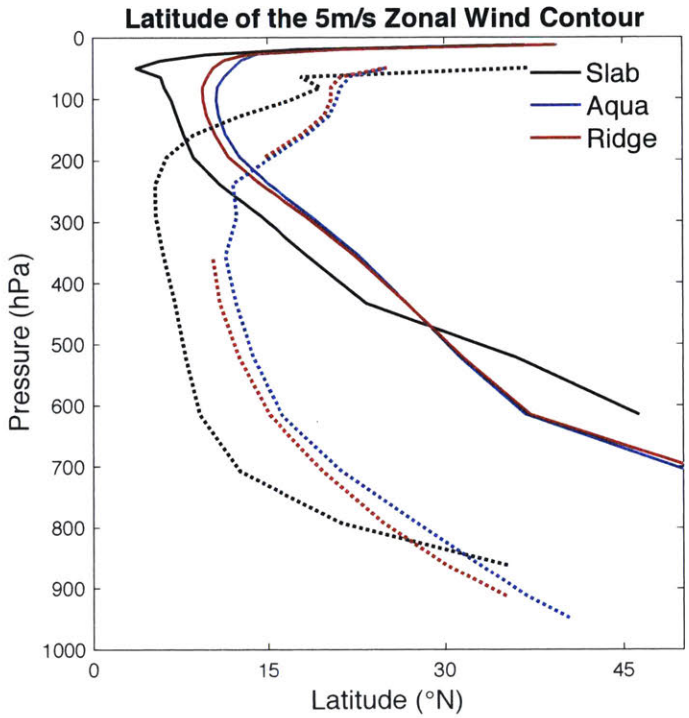

Figure 5.11. Latitude of the 5 m s^{-1} zonal mean zonal wind contour for the warmest (solid lines) and coldest (dotted lines) simulations.

5.6. Summary and Discussion

We have explored the influence of the tropical-subtropical ocean circulation on the strength of the atmosphere's Hadley cells in a fully coupled atmosphere-ocean GCM. Across a wide range of global mean temperatures, the Hadley cells are significantly weaker compared to simulations with a stationary slab ocean. This weakening is largest for colder climates, about 70%, where a reduction of the heating contrast across the Hadley cell combines with a widening of the cell's ascent region in the fully coupled runs. In warmer climates, the width of the ascent region is similar between fully coupled and slab ocean runs, and the magnitude of the weakening from the slab ocean to the fully coupled runs is reduced to about 30 %.

The primary mechanism behind the weakened Hadley circulation is the poleward heat transport by the ocean's subtropical cells, which acts to reduce the heating contrast across the Hadley cell. We quantified the changes in the heating contrast between the slab ocean and fully coupled runs using an energetic framework, splitting it into contributions by fluxes of radiation and heat transport by atmospheric eddies and the ocean circulation. The STCs' poleward heat transport, acting to cool the ascending branch of the Hadley cell and heat the descending branch, is partially compensated by a reduced poleward energy transport by atmospheric eddies. The eddies' anomalous energy transport is well described by the meridional gradient in near-surface moist static energy, which we interpret as a passive response to ocean-driven changes in sea surface temperatures.

Angular momentum fluxes by atmospheric eddies play a secondary role in the changes to the Hadley cell's strength between the model configurations, but their effects are not negligible, particularly in warm climates. Generally, they act to further weaken the Hadley cell in the fully coupled runs. One effect of the ocean's heat transport is to weaken the strength of the atmosphere's subtropical jet, which widens the region of zonal mean zonal winds where waves originating in the extratropics break. We hypothesize this then spreads out the divergence of their momentum fluxes over a larger region and weakens their mechanical forcing of the Hadley cell.

Adding a pole-to-pole barrier in the ocean has the effect of strengthening the Hadley cell relative to simulations without one. We attribute part of this change to a reduction of the heat transport by the subtropical cell, which is weakened by the presence of zonal mean zonal pressure gradients. The Ridge geometry also creates horizontally circulating ocean gyres, but their impact on the energy balance of the Hadley cell is minimal and offset by reductions in heat transport due to oceanic baroclinic eddies. Angular momentum fluxes by atmospheric eddies

contribute to the Hadley cell strengthening in warm climates; their influence is tied to a slight equatorward shift of both the zonal mean zonal winds and the distribution of the eddy momentum flux divergence.

In some ways, our results are similar to those of Levine and Schneider (2011). Like LS11, the Hadley cell in our runs is always weaker when the ocean's poleward heat transport is included. We also find that changes in eddy momentum fluxes between the slab ocean and fully coupled runs play a secondary role in zonal momentum budget of the Hadley cell's upper branch. One notable difference in our Slab runs is the strong Hadley cell at cooler climates (compare our Figure 5.2a to their Figure 4), where their cell weakens relative to the reference climate. Several parameters in our gray radiation atmospheric model are different than theirs, notably the inclusion of a seasonal cycle, an equator-to-pole albedo gradient, and a water vapor feedback on the longwave radiation optical thickness. We performed several additional experiments with the slab ocean model where these parameters were varied, and only turning off the water vapor feedback significantly weakened the Hadley cell at cooler climates – for a global mean SST of 3 °C, ψ_{HC} was 76 Sv, 59 % weaker than the comparable slab ocean run in Figure 5.2a. The mechanisms connecting the water vapor feedback to the Hadley cell strength are unknown at the moment and could be explored in future work.

A difference between our results and those in LS11 is the mechanism behind the dependence on global mean SST of the ocean-driven weakening of the Hadley cell. Weakening of the Hadley cell by the ocean circulation is diminished at the warmest SSTs, which LS11 attributes to a reduced meridional SST gradient reducing the STC's gross stability and its heat transport. However, heat transport by the STCs (solid blue lines, Figure 5.7a, b) and its impact on the Hadley cell's heating contrast (Figure 5.6) in our runs does not depend strongly on global

mean SST, even though the meridional SST gradient decreases as the climate warms (Figure 5.5). Instead, we find the reason the weakening of the Hadley cell is largest for cold climates is the increase in the width of its ascending branch in those runs, compounded with the dependence of the Hadley cell's gross stability on latitude. In the warmer runs, the ascending branch has similar widths between the fully coupled and Slab runs, and the magnitude of the weakening in the fully coupled runs is diminished. This same behavior of the width of the ascending branch is seen in Figure 2 of LS11.

The reason the heat transported by the STC in our model does not exhibit the same dependence on the meridional gradient of SST as the model employed by LS11 is the effects of mixing at its poleward edge. The simple model of the STC's gross stability employed by LS11 (Klinger and Marotzke 2000, Held 2001) assumes that the subsurface branch of the STC conserves the surface temperature of water subducted by Ekman pumping in the subtropics. As it flows equatorward, the subsurface branch of our STCs does generally conserve temperature, with streamfunction contours roughly following isotherms (Figure 5.3, middle and right columns). When that water is subducted, though, it is cooled and the streamfunction contours cross isotherms before bending equatorward. Consequently, the gross stability of our STCs is significantly higher than estimates that assume its lower branch conserves the surface temperature of the latitude where it was subducted, even if we assume that subduction occurs during wintertime (Figure 5.12). The difference between the gross stability of our model's STC and the SST-based estimates means that the type of simple model employed by LS11 underestimates the heat transported by the STCs. Furthermore, Figure 5.12 implies that mixing at the STC's poleward edge likely plays an important role in setting its gross stability.

Though our model adds a measure of realism by including a fully coupled three-dimensional ocean, it is still idealized and lacks several features of more complex GCMs that likely play important roles in setting the strength of the Hadley cell. First, our gray radiation scheme does not include the effects of clouds – in particular, the subtropical low-level stratocumulus clouds that can significantly alter the cross-cell heating contrast. Of the terms in Figure 5.7 that contribute to the reduction of the cross-cell heating contrast in the fully coupled runs, changes in fluxes of radiation are so small they are negligible; this may not be the case in models with more complex parametrizations of radiation and convection. Also lacking land, our water-covered model might overestimate the importance of the ocean circulation and its heat transport on the Hadley cell strength. As the Hadley cells expand upward and poleward in our model, the impact of the sponge layer on the atmosphere's angular momentum balance increases, particularly in the extratropics where it weakens and narrows the surface westerly jet. Without the sponge layer removing zonal momentum from the atmosphere, this weakening and narrowing of the jet might not occur and the Hadley cell might not expand poleward as much as it does in our warmest simulations.

Despite these shortcomings, the weakening of the Hadley cell by the ocean circulation appears to be a robust result. The subtropical cells are coupled to the Hadley cells by the surface trade winds, making it unavoidable that their poleward heat transport reduces the heating contrast across the Hadley cells. This makes the STCs important to leading order in the dynamics of the Hadley cells, and any theory for the strength of the Hadley cells must take their heat transport into account. Moreover, simulations of the atmospheric circulation in a warming climate that do not include a coupled ocean circulation likely misrepresent any changes in the strength of the Hadley cells. In our simulations, the Hadley cell weakens as the climate warms in the slab ocean

model, but its strength remains roughly constant in both fully coupled configurations. A starting point for diagnosing the impact of the STCs on the Hadley cell strength in more complex models simulating climate change could be through the use of the heating contrast framework.

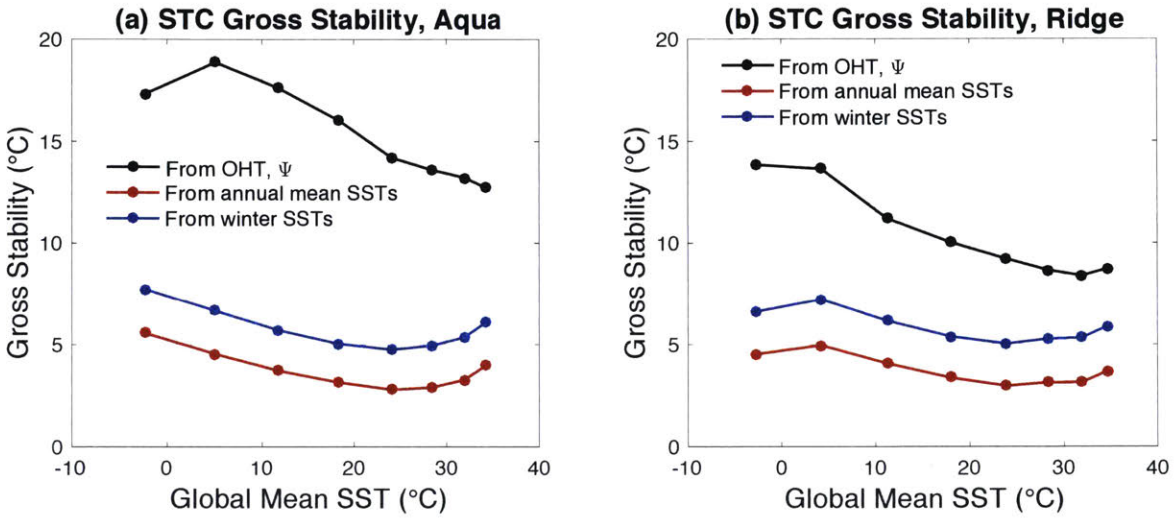

Figure 5.12. The gross stability of the subtropical cell at the latitude of the peak northward Ekman mass transport. (a) In the Aqua runs. Black line: the ratio of the ocean heat transport to the product of the strength of the overturning streamfunction and the specific heat capacity. Red line: applying Eq. (7) from Held (2001) to annual mean SSTs. Blue line: same as the red line, except using wintertime SSTs to calculate the average temperature of the subsurface branch; annual mean SST is used for the temperature of the surface branch. (b) Same as (a) but for the Ridge runs.

Chapter 6

Discussion

This thesis has touched on several aspects of coupled ITCZ, Hadley cell, and ocean circulation dynamics. The ocean circulation, through its heat transport and associated surface heat fluxes, is capable of both forcing and moderating ITCZ shifts. By transporting heat across the equator and fluxing it into and out of the extratropical NH atmosphere, the AMOC is capable of forcing ITCZ shifts by heating one hemisphere relative to the other. Evidence supporting the AMOC's role in 20th Century ITCZ variability was presented in Chapter 2, where it was found that on multi-decadal timescales the ITCZ has shifted north when the North Atlantic was warm, and south when the North Atlantic was cold.

Chapters 3, 4, and 5 have focused on how the coupling of the tropical ocean circulation and its heat transport to the ITCZ and Hadley cells affects the atmosphere's response to an imposed forcing. The ocean's subtropical cells are driven by the surface easterly trade winds and overturn in the same sense as the Hadley cells above, coupling the heat transport of the two fluids. The relatively high stratification of the tropical ocean means that the STCs efficiently transport heat in the tropics, first pointed out by Held (2001), which acts to both damp ITCZ shifts and weaken the Hadley cells relative to cases where cases where their heat transport is not accounted for. It was argued that, because the STCs' and Hadley cells' energy transports are coupled by the trade winds, the results from our experiments with an idealized aquaplanet GCM are robust and can be applied to the study of Earth's ITCZ and Hadley cells.

The broadest view on this work is that the ocean plays a leading-order role in the zonal mean, annual mean dynamics of tropical rainfall. The influence of AMOC variability on the ITCZ position has been studied extensively in climate models and inferred from paleoclimate records, but the coupling of the Hadley cells and STCs represents a previously underappreciated constraint. In particular, Chapters 3 and 4 represent a step forward in the study of ITCZ shifts, showing how the STCs act to damp any shifts and keep the ITCZ stuck to latitudes near the equator. The results in those chapters and the theory developed for the STCs' role in the atmosphere's hemispheric energy balance offer an explanation for recent results from more complex fully coupled GCMs showing a muted response of tropical rainfall to interhemispheric heating contrasts, and predict a factor of two damping of ITCZ shifts on Earth.

One application of the results of Chapter 3 has been to the study of ITCZ shifts during the stadial events of the past 50,000 years. Paleo proxies for precipitation are sparse and indirect, making constraining past ITCZ shifts difficult. The coupling of the ITCZ to the Hadley cells and trade winds, however, is a robust physical mechanism, and ITCZ shifts are expected to be associated with hemispherically asymmetric patterns of trade winds anomalies. For example, for the hypothesized southward ITCZ shifts during stadial events, the paleo record can be interrogated for a simultaneous intensification of NH trade winds and a weakening of SH trade winds. McGee et al. (2018), compiling proxy records of coastal upwelling and windblown dust, found this to be the case: during stadial events, these proxies for trade wind strength show globally synchronous, hemispherically asymmetric patterns indicative of southward ITCZ shifts. The signal is particularly robust in the tropical Atlantic Ocean, in agreement with climate model simulations of stadial events. Coupled ITCZ-trade wind shifts, then, might prove useful for further study and constraint of paleo ITCZ shifts.

The annual mean, zonal mean approach to the ITCZ has its limitations (e.g. Donohoe 2016), and past regional ITCZ shifts have been estimated to be much larger than the zonal mean (McGee et al. 2014), raising the question: are the ideas developed in this thesis relevant to the study of regional precipitation variability? An example where the wind-driven ocean might affect the atmospheric energy balance and circulation is the Asian monsoon system. Coupled to the seasonally reversing monsoon circulation, the Indian Ocean transports large quantities of heat southward across the equator in NH summer, cooling the SSTs of the upper ocean (Loschnigg and Webster 2000). Chapters 3 and 4 suggest that this upper ocean cooling would weaken the monsoon system, reducing the atmosphere's cross-equatorial mass and heat transport. Does this weakening of the summer cross-equatorial Hadley cell occur, and how might the cooler SSTs impact the precipitation distribution in the presence of land? Preliminary results from experiments, performed by Nick Lutsko, with an atmospheric GCM show a strong sensitivity of the model's monsoon system to the inclusion of an idealized representation of wind-driven ocean heat transport, meriting further study.

The upwelling and heat transport divergence associated with the STCs, balanced by surface heat fluxes in a steady state, is zonally asymmetric and cools the eastern sides of the Atlantic and Pacific basins more strongly than the western sides. How does this zonal asymmetry project onto the zonal mean, and how does it interact with the precipitation onto the African, South American, and the maritime continents? A framework for connecting regional heating and cooling of the atmosphere into its global energy balance and the tropical precipitation distribution was recently proposed by Boos and Korty (2016) and may provide a path forward for describing the regional impact of the ocean's heat transport in a changing climate. Boos and Korty translate local and remote heating of the atmosphere into regional patterns of heat

transport anomalies by describing the atmosphere's divergent energy transport as downgradient of an "energy flux potential", whose anomalies are related to the heating distribution by a Poisson equation. Solving the equation for the energy flux potential, shifts in the distribution of the atmosphere's energy transport are then applied to the climatological precipitation distribution to estimate regional precipitation anomalies. If the atmosphere's heat transport anomalies in the tropics can be attributed to changes in the steady circulation, which would drive upwelling and downwelling anomalies in the ocean at predictable locations, the resulting surface heat fluxes could be fed back into the Poisson equation and their impact on the precipitation distribution could be estimated as the model is iterated to equilibrium.

Another method of quantifying the regional impact of the ocean circulation on regional tropical precipitation could be through the use of models that tie the precipitation to the distribution of SSTs (see the review in Sobel 2007). Models of this type (e.g. Back and Bretherton 2009a, b) connect the atmosphere's vertical motion and rainfall to surface convergence and the coupling between the lower and middle troposphere, both of which are sensitive to SSTs. If, for a given change in climate, anomalies of surface convergence and SST are fed into a model of the wind-driven ocean circulation and the resulting heat transport divergence anomalies are translated back into SST anomalies, this model could also be iterated to reach a solution for the regional rainfall distribution.

A separate avenue for future work might be investigating controls on the relative strengths of the STCs and the Hadley cells. Held (2001) made a useful simplifying assumption that the two circulations have similar strengths – through Ekman balance, this must be true near the surface – but I found in Chapters 3 and 4 that a wind-driven oceanic cross-equatorial cell is likely much weaker than its atmospheric counterpart. In Chapter 5, I also found that the STCs

strengthen with global mean SSTs even though the total Hadley cell strength is roughly constant. These results should prompt a reevaluation of Held's assumption, which would predict an oceanic CEC that is much stronger and even more efficient at damping ITCZ shifts. The surface stress exerted by the easterly trade winds, and the meridional near-surface flow associated with that stress, are in balance with the atmosphere's angular momentum transport divergence; estimates of the strength of the near-surface flow must take this balance into account. The results of Chapter 4 suggest that changes in the annual mean trade wind strength associated with an ITCZ shift can be predicted from the climatological seasonal cycle, but physical arguments connecting the two have not progressed beyond simple scalings based on thermal wind balance (e.g. Emanuel 1995). A modeling hierarchy consisting of atmospheric GCMs run in axisymmetric and three-dimensional configurations, alternatively removing and including the effects of eddy momentum fluxes, might be a useful approach.

At the moment, measuring the impact of this thesis is a difficult proposition. The role of the STCs in ITCZ dynamics is an active field of research; for example, Section 4.5 seeks to respond to research published since Chapter 3 appeared in *Journal of Climate*. One predictor of the successes of the ideas I presented here might be the questions they raise and the avenues of research they open, some of which have been discussed in this Chapter. There is undoubtedly more research to be conducted in this field and more questions to be answered about the coupled ITCZ-Hadley cell-tropical ocean circulation system, but I must end here and thank you for your attention to and consideration of my thesis.

Appendix A1

Supplementary Material for Chapter 2

The Supporting Information for this manuscript contains four parts related to the calculations and results in Chapter 2. Section A1.1 describes the methods of analysis presented in the manuscript. Section A1.2 describes the validation of the S12, E20CM, and N20CR estimates of the ITCZ position against satellite data. Section A1.3 describes regressions against Ψ_{eq} and $T_{interhem}$ in the E20CM and N20CR reanalyses, which results are included in Tables A1.2 and A1.3. Figures A1.1 to A1.5 and Table A1.1 are referenced in Chapter 2; Figure A1.6 is referenced in section A1.2.

A1.1 Details of Calculations in Chapter 2

To define the AMO and PDO indices, we respectively area weight SST from 80 °W-0 ° longitude and 0 °-60 °N latitude, and 110 °E-100 °W longitude and 20 °N-70 °N latitude. The indices' values are then defined as the global mean SST subtracted from these area-weighted values.

All of the regressions performed in Figures 2.3, 2.4, A1.2, A1.3, A1.5, and Tables A1.1 and A1.3 use the AMO and PDO indices as predictors in a multiple regression analysis. All three time series (the AMO, PDO, and the predictand) are first low-pass filtered, then de-trended prior to the regression analysis. The low-pass filter is an order 10 Butterworth filter with a cutoff period of 10 years. Both the unfiltered yearly anomalies of the AMO and PDO indices and their low-pass filtered time series are nearly uncorrelated: R = -0.10 and -0.05, respectively.

Output from the regression analysis includes the correlation R between the predictor and predictand, the slope relating the predictand to the predictor, and an error estimate of the slope. For example, in the regressions against the ITCZ position, the slope has units of °N/K since the AMO and PDO time series have units of Kelvin. Anomalies of the predictand are calculated by multiplying the slopes by an AMO or PDO anomaly (in Kelvin). Anomalies in Tables A1.1 and A1.3, and Figures 2.1, 2.3, 2.4, and A1.1 to A1.5 are for $+1\sigma$ of the annual mean AMO (+0.14 K) or PDO (+0.12 K) time series, even if the time series have been low-pass or high-pass filtered.

Because the filtered time series no longer resemble AR-1 processes, the effective degrees of freedom of the regressions (to estimate the error of the slope) are calculated following Bretherton et al. (1999) Eq. (30), summing over the first 20 one-year lags. The significance of spatial correlations between the precipitation anomaly maps in Figure 2 is estimated by calculating the effective number of spatial degrees of freedom in the low-pass filtered precipitation anomalies following Bretherton et al. (1999) Eq. (3).

The indices of the Hadley cell strength at the equator (Ψ_{eq}) and the inter-hemispheric temperature contrast in the troposphere ($T_{interhem}$) are respectively calculated from annual mean values of the meridional overturning streamfunction and zonal mean temperatures in the NCEP/NCAR, E20CM, and N20CR reanalyses. Their time series are then low-pass filtered and detrended before being multiple-regressed against the AMO and PDO indices to obtain the values in Tables A1.1 and A1.3. The Hadley cell strength index,Ψ_{eq}, is the time series of the vertically averaged streamfunction evaluated at the equator. The streamfunction is calculated from zonal mean meridional velocities, which are first corrected to remove any vertical mean, annual mean meridional mass transport across a latitude circle. Hemisphere mean temperatures

in the troposphere are calculated by averaging zonal mean temperatures between the equator and the pole and between the surface and 300 hPa. The difference between the northern and southern hemisphere's values defines the $T_{interhem}$ index, where positive values indicate a relatively warm northern hemisphere troposphere.

In Figure 2.4, the temperature anomaly at a given latitude y can be split into symmetric and asymmetric components: $T(y) = T_{asym}(y) + T_{sym}(y)$, with $T_{asym}(y) = -T_{asym}(-y)$ and $T_{sym}(y) = T_{sym}(-y)$. The asymmetric component, T_{asym}, is plotted in Figure 2.4.

A1.2 Interannual Variability of the ITCZ Position over the Satellite Era

Time series of the annual mean ITCZ position between 1979 and 2008 are shown in Figure A1.6 for the GPCP (version 2.2; Adler et al. (2003)), S12, E20CM, and N20CR products. The GPCP version 2.2 product combines satellite estimations of precipitation with rain gage observations over land to estimate monthly mean precipitation on a global grid with 2.5 ° horizontal resolution. Since the GPCP product is the most directly constrained by observations, its time series is taken as the "observed" ITCZ position and the other products are compared to it. The three other products appear to match the GPCP time series well and exhibit the southward ITCZ shifts observed in 1983, 1992, and 1998.

Regressing annual mean values for the S12, E20CM, and N20CR time series against the GPCP time series, all three products explain similarly high amounts of variance. For the S12-GPCP regression, $R^2 = 0.79$; for E20CM-GPCP, $R^2 = 0.76$; and for N20CR-GPCP, $R^2 = 0.70$. Given that S12 uses EOFs calculated from GPCP precipitation anomalies, and the relatively high spatial coverage of rain gauges in the satellite era, it is perhaps unsurprising that its time series is

the most highly correlated with the GPCP's. The regression slopes indicate all three products, on average, underestimate the magnitude of ITCZ shifts, with E20CM most closely matching the GPCP observations. Despite underestimating the magnitude of ITCZ shifts, the S12, E20CM, and N20CR products capture well the direction of those shifts between 1979 and 2008, making all three equally suitable for studying ITCZ shifts.

A1.3 Regressions of the AMO and PDO onto the Atmospheric Circulation in 20th Century Reanalyses

Because of the shortcomings mentioned in Chapter 2.2, results for regressions against Ψ_{eq} and $T_{interhem}$ in E20CM and N20CR are not included in the main text. We include them here for comparison to the NCEP/NCAR results. First, we regress circulation indices in E20CM and N20CR against their more observationally-constrained values in NCEP/NCAR. Between 1948 and the end of their runs, low-pass filtered Ψ_{eq} and $T_{interhem}$ indices from E20CM and N20CR are significantly correlated with those from NCEP/NCAR (Table A1.2), with E20CM better matching the observed variability of both indices, particularly Ψ_{eq}. Annual mean (unfiltered) anomalies in E20CM and N20CR between 1979 and 2010 are also correlated with those in the NCEP/NCAR reanalysis. However, both reanalysis better describe observed variability in the ITCZ position during that period, discussed above in section A1.2, then in Ψ_{eq} and $T_{interhem}$, making them less suitable for studying atmospheric circulation variability.

Over the full period of the E20CM and N20CR reanalyses, the AMO is significantly correlated with both Ψ_{eq} and $T_{interhem}$, but the fraction of their variance it explains is reduced compared to the NCEP/NCAR reanalysis (Table A1.3). The PDO is significantly correlated with those indices only in the N20CR reanalysis, with the sign of the PDO- $T_{interhem}$ relationship

reversed: a warm North Pacific is associated with a cool NH troposphere. When the period of the regressions is limited to that covered by the NCEP/NCAR reanalysis (the values in parentheses in Table A1.3), the AMO is no longer significantly correlated with Ψ_{eq} in N20CR, and the PDO becomes significantly correlated with both Ψ_{eq} and $T_{interhem}$ in E20CM. Again, the sign of the PDO- $T_{interhem}$ relationship in N20CR is the opposite of what we expect. Given that E20CM more reliably reproduces observed atmospheric variability, particularly for Ψ_{eq}, we believe that the key results from the NCEP/NCAR regressions are unchanged. Namely, that a warm phase AMO is associated with an anomalous cross-equatorial Hadley cell and a relatively warm NH troposphere. A warm phase PDO is also associated with a cross-equatorial Hadley cell since 1948, but it is unclear if that is true earlier in the 20th Century, and the relationship between the PDO and inter-hemispheric temperature contrasts is unclear.

	R^2		Anomaly ($\pm 1\sigma$)	
	AMO	**PDO**	**AMO**	**PDO**
ITCZ (°N):				
S12	0.11	0.14	0.07 ± 0.05	0.10 ± 0.06
E20CM	0.20	0.04	0.12 ± 0.05	0.07 ± 0.07
N20CR	0.12	0.06	0.18 ± 0.11	0.13 ± 0.12
Ψ_{eq} (Sv):				
NCEP/NCAR	0.41	0.17	-2.8 ± 1.1	-3.4 ± 1.8
$T_{interhem}$ (K):				
NCEP/NCAR	0.74	0.02	0.16 ± 0.05	0.04 ± 0.07

Table A1.1. Regressions against the low-pass filtered AMO and PDO indices. Left two columns: fraction of the variance explained (R^2) by the AMO and PDO indices for anomalies of the ITCZ position, equatorial streamfunction Ψ_{eq}, and tropospheric inter-hemispheric temperature contrast

$T_{interhem}$. Right two columns: anomalies are for +1σ of the annual mean AMO (+0.14 K) and PDO (+0.12 K), and error estimates are ±1σ.

		R^2			Slope (±1σ)		
		NCEP/NCAR	**E20CM**	**N20CR**	**NCEP/NCAR**	**E20CM**	**N20CR**
Ψ_{eq}	**NCEP/NCAR**	1.00			1.00 ± 0.00		
	E20CM	0.55	1.00		0.53 ± 0.14	1.00 ± 0.00	
		[0.74]			[1.18 ± 0.11]		
	N20CR	0.25	0.20	1.00	0.42 ± 0.17	0.46 ± 0.30	1.00 ± 0.00
		[0.45]	(0.25)		[0.73 ± 0.14]	(0.78 ± 0.32)	
$T_{interhem}$	**NCEP/NCAR**	1.00			1.00 ± 0.00		
	E20CM	0.67	1.00		0.39 ± 0.14	1.00 ± 0.00	
		[0.31]			[0.49 ± 0.13]		
	N20CR	0.52	0.15	1.00	0.60 ± 0.23	0.68 ± 0.61	1.00 ± 0.00
		[0.34]	(0.07)		[0.67 ± 0.17]	(0.65 ± 0.82)	

Table A1.2. Validation of E20CM and N20CR reanalyses against the NCEP/NCAR reanalysis. Regressions using the NCEP/NCAR reanalysis are performed between 1948 and 2010 (E20CM) or 2011 (N20CR). Regressions between E20CM and N20CR are performed between 1948 and 2010, or 1900 and 2010 (values in parentheses). Values in brackets are for regressions performed on annual mean anomalies (no filtering) between 1979 and 2008. The slopes are calculated using the index for that cell's column as the predictor and the index for that cell's row as the predictand, and error estimates are ±1σ.

		R^2		Anomaly (±1σ)	
		AMO	**PDO**	**AMO**	**PDO**
Ψ_{eq} (Sv)	**NCEP/NCAR**	0.41	0.17	-2.8 ± 1.1	-3.4 ± 1.8
	E20CM	0.35	0.04	-1.9 ± 0.6	-0.8 ± 0.8
		(0.16)	(0.15)	(-1.2 ± 0.6)	(-2.2 ± 1.6)
	N20CR	0.08	0.18	-1.7 ± 1.3	-2.7 ± 1.4
		(0.03)	(0.15)	(-0.7±0.9)	(-2.8±1.7)
$T_{interhem}$ (K)	**NCEP/NCAR**	0.74	0.02	0.16 ± 0.05	0.04 ± 0.07
	E20CM	0.68	0.01	0.08 ± 0.02	0.01 ± 0.02
		(0.36)	(0.29)	(0.05 ± 0.02)	(0.09 ± 0.03)
	N20CR	0.09	0.20	0.08 ± 0.07	-0.13 ± 0.05
		(0.62)	(0.10)	(0.13±0.05)	(-0.09±0.08)

Table A1.3. Regressions against the AMO and PDO indices. Left two columns: fraction of the variance explained (R^2) by the AMO and PDO indices for the equatorial streamfunction anomaly Ψ_{eq} and tropospheric inter-hemispheric temperature contrast anomaly $T_{interhem}$. The NCEP/NCAR results are identical to those in Table A1.1. Right two columns: anomalies are for +1σ of the annual mean AMO (+0.14 K) and PDO (+0.12 K), and error estimates are ±1σ. Parentheses on E20CM and N20CR values are for regressions from 1948 to 2010 (E20CM) or 2011 (N20CR) to be consistent with the NCEP/NCAR regressions from 1948 to 2012 in Table A1.1.

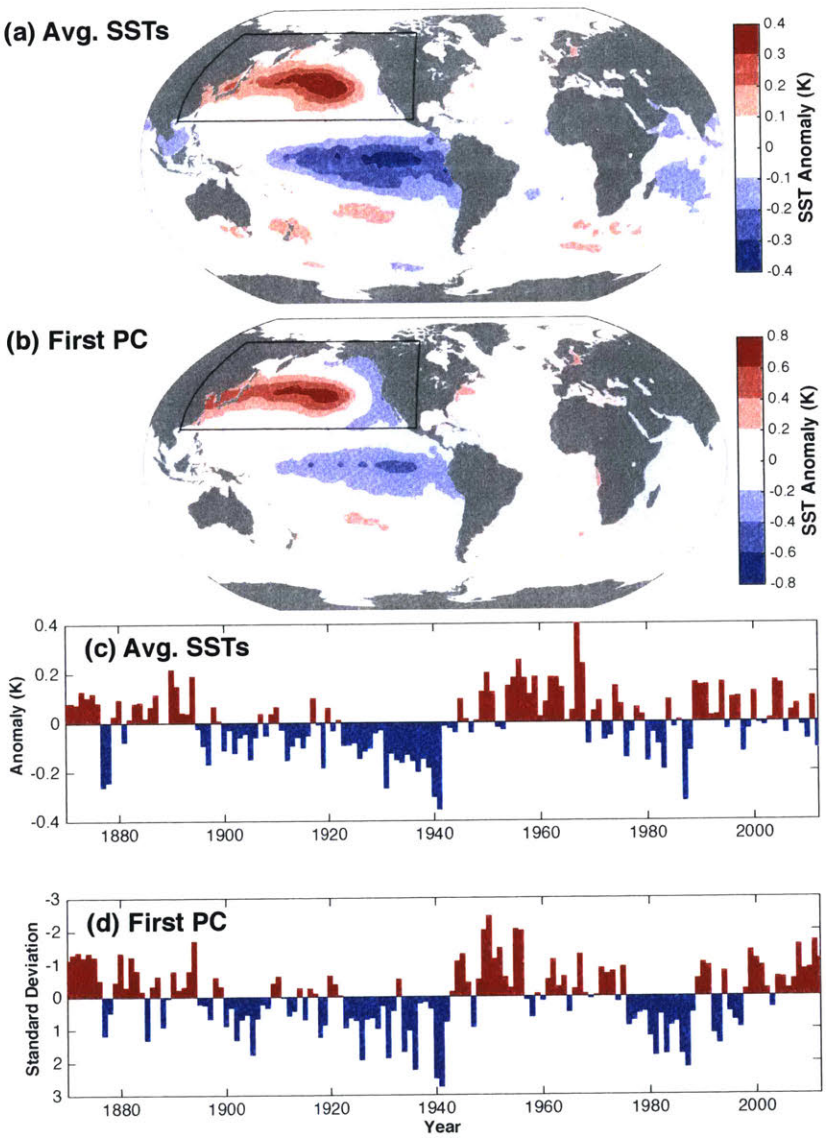

Figure A1.1. PDO time series and SST anomaly patters. (a) SST anomalies regressed against a +1σ anomaly of our annual mean PDO index, identical to Figure 1d. Contour interval: 0.1 K. (b) SST anomalies regressed against a -1σ anomaly of the first PC from an EOF analysis of monthly mean SST anomalies in the North Pacific (boxed region), as in Mantua et al. (1997). Contour interval: 0.2 K. (c) Time series of annual mean anomalies of our PDO index, identical to Figure 2.2e. (d) Time series of annual mean anomalies of the first PC, normalized by their standard deviation.

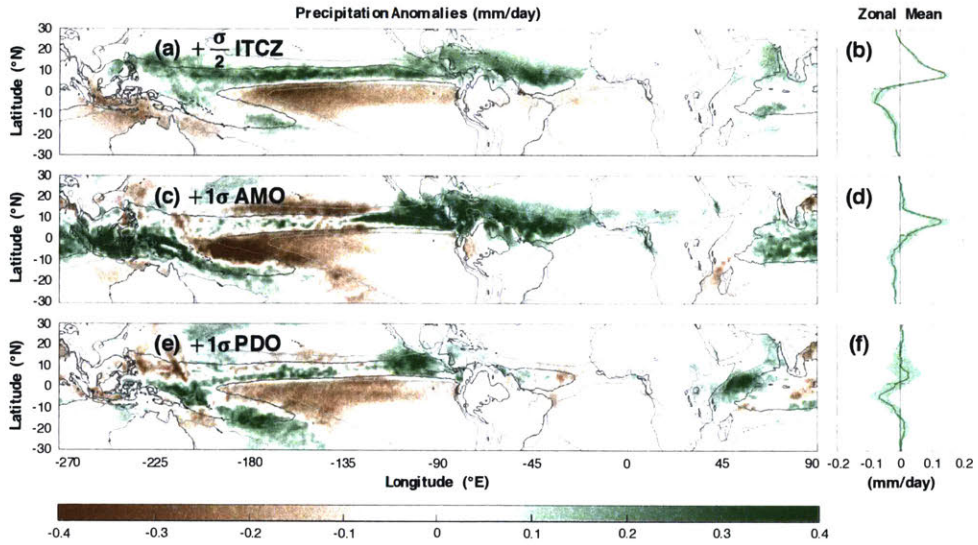

Figure A1.2. As in Figure 2.3, but for E20CM precipitation anomalies. The green dashed line indicates the time mean ITCZ position of 2.1 °N.

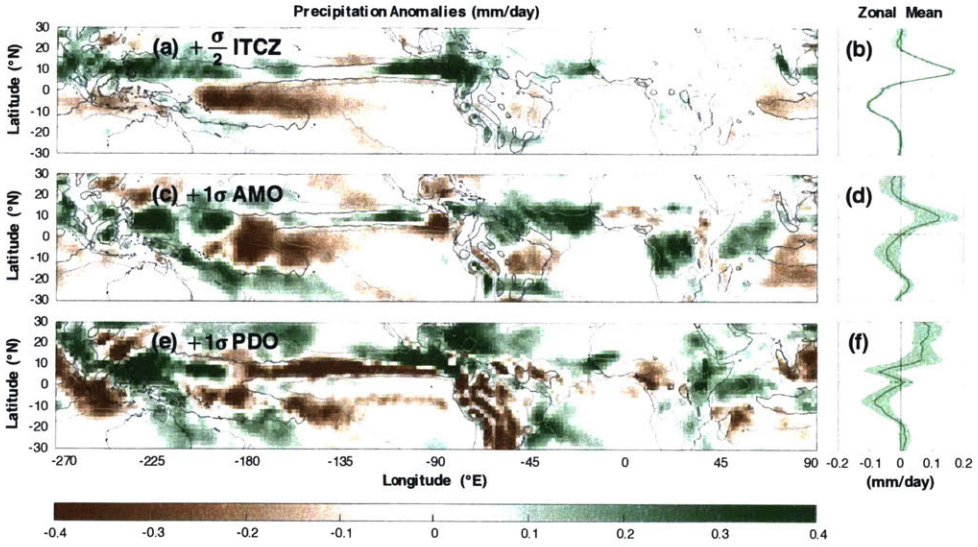

Figure A1.3. As in Figure 2.3, but for N20CR precipitation anomalies. The green dashed line indicates the time mean ITCZ position of 1.9 °N.

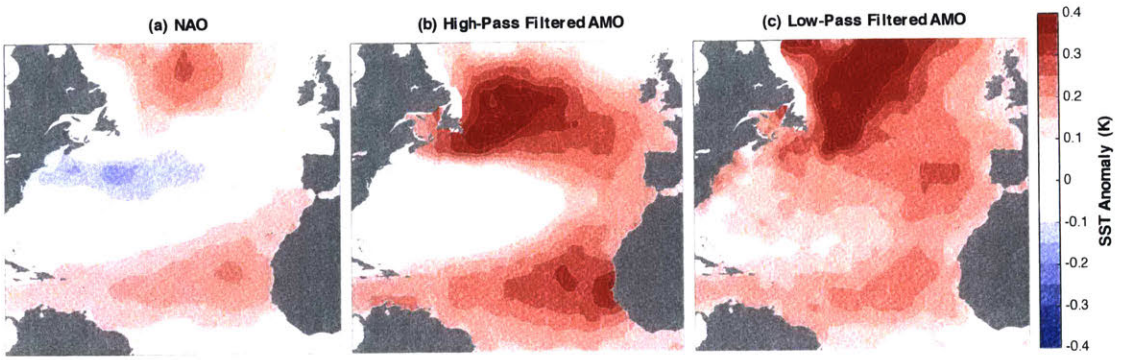

Figure A1.4. North Atlantic SST variability. Sea surface temperature anomalies regressed against (a) -1σ of the annual mean NAO index, and +0.14 K anomalies of the (b) high-pass and (c) low-pass filtered AMO index. The high- and low-pass filters employ cutoff periods of 10 years, and the filters are applied to both the SST anomalies and the AMO index prior to the regression. Contour interval: 0.05 K.

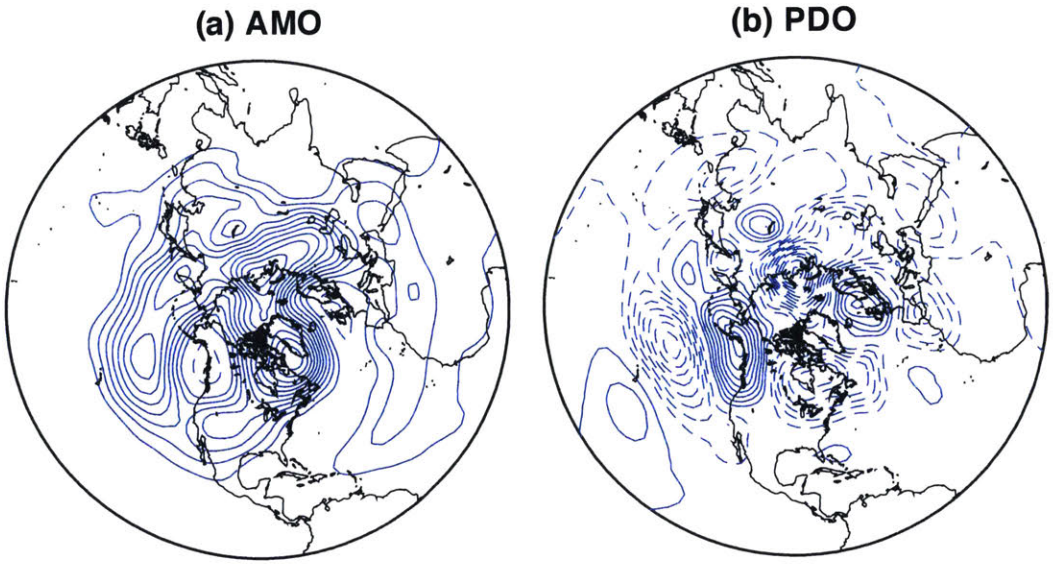

Figure A1.5. Geopotential height anomalies. Low-pass filtered geopotential height anomalies at 300 hPa in the NCEP/NCAR reanalysis associated with +1σ anomalies of the low-pass filtered

(a) AMO and (b) PDO indices. Solid contours indicate positive anomalies and dashed contours indicate negative anomalies. The contour interval is 2 m.

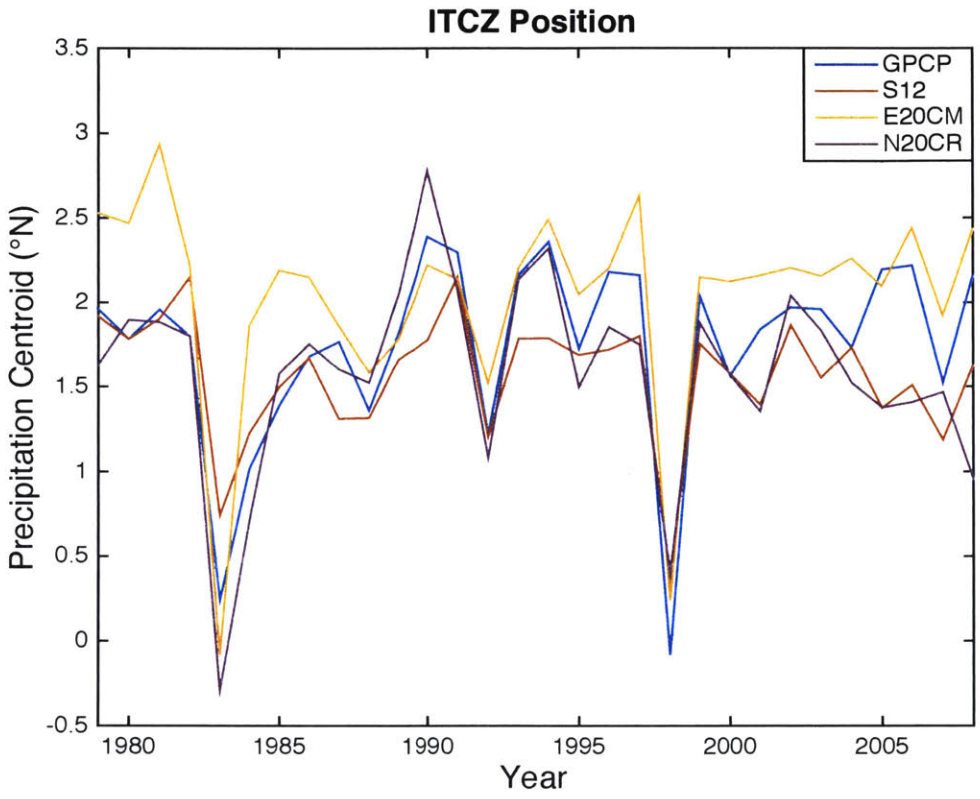

Figure A1.6. ITCZ position time series. The annual mean latitude of the precipitation centroid is shown for the (blue) GPCP, (red) S12, (yellow) E20CM, and (purple) N20CR products between 1979 and 2008.

Appendix A2

ITCZ Shifts in the Energy Flux Equator Framework

The "energy flux equator" framework proposed in Bischoff and Schneider (2014) and Schneider et al. (2014) is similar to but distinct from the approach of Donohoe et al. (2013) and that taken in our Eq. (3.3). Rather than relating the location of the precipitation centroid to the atmosphere's cross-equatorial energy transport by a constant regression coefficient, as in Eq. (3.3a), it defines the ITCZ position as the location where the atmosphere's meridional energy transport goes to zero. Despite these differences, though, the energy flux equator framework is useful in understanding why the slope of the relationship between the ITCZ position and the atmosphere's cross-equatorial energy transport in Figure 4b (-1.8 ° PW^{-1}) is shallower than in the observations (-2.7 ° PW^{-1}; Donohoe et al. 2013). Equation (2) in Schneider et al. (2014) estimates the ITCZ position (δ) as

$$\delta \approx -\frac{1}{a}\frac{F_0}{S_0 - L_0 - O_0} \quad (A2.1)$$

where a is the radius of the earth, F_0 is the cross-equatorial energy transport by the atmosphere, S_0 is the net downward shortwave radiation at the top of the atmosphere, L_0 is the outgoing longwave radiation at the top of the atmosphere, and O_0 is the downward flux of energy at the ocean surface which, in a steady state, represents ocean heat transport divergence. The subscript 0 denotes values taken at the equator.

The slope of the ITCZ-atmospheric energy transport relationship can be found by dividing Eq. (A2.1) by F_0:

$$\frac{\delta}{F_0} = -\frac{1}{2\pi a^2}\frac{1}{NEI} \quad (A2.2a)$$

where

$$NEI = \frac{1}{2\pi a}(S_0 - L_0 - O_0) \quad (A2.2b)$$

is the net input of energy into the atmosphere at the equator, in W m^{-2}. Using the 32 W m^{-2} diagnosed from our simulations and the 18 W m^{-2} assumed by Schneider et al. 2014, the slopes are -7 ° PW^{-1} and -13 ° PW^{-1} respectively. It is worth noting that the -7 ° PW^{-1} slope using the energy flux equator metric is much higher than the -1.8 ° PW^{-1} using the precipitation centroid metric, and that *NEI* is nearly identical (within 0.4 W m^{-2}) between the slab runs and the fully coupled runs by design. One way to increase the steepness of the slope, bringing it closer to the observations, would be to increase the albedo at the equator. This would decrease S_0, and likely L_0, and thus *NEI*.

However, *NEI* and hence equatorial albedo plays a negligible role when considering the relative ITCZ shifts in slab ocean and fully coupled model runs. We can see this as follows. Starting from Eq. (A2.1) and (A2.2b), a change in the ITCZ position ($\Delta\delta$) is expressed as

$$\Delta\delta = -\frac{1}{2\pi a^2}\Delta\left(\frac{F_0}{NEI}\right) \quad (A2.2a)$$

$$= -\frac{1}{2\pi a^2}\frac{1}{NEI}\left(\Delta F_0 - F_0\frac{\Delta NEI}{NEI}\right). \quad (A2.2b)$$

Inspecting the terms in Eq. (A2.2b), ΔF_0 is at least one order of magnitude larger than the other term in both the slab ocean and fully coupled model runs. This makes intuitive sense given the nature of the inter-hemispheric forcing: the albedo at the equator is not changed (S_0 is unchanged), the temperature there does not significantly change (L_0 changes are small), and the ocean is transporting energy across the equator, not converging or diverging it there (O_0 changes are small). In this limit, the fractional change in *NEI* is small and the ITCZ shift can be expressed as

$$\Delta\delta \approx -\frac{1}{2\pi a^2}\frac{\Delta F_0}{NEI}. \quad (A2.3)$$

The ratio of the ITCZ shift in the slab ocean case (subscript *slab*) to the fully coupled case (subscript *cpl*) is then the ratio of the anomalous cross-equatorial energy transports:

$$\frac{\Delta\delta_{slab}}{\Delta\delta_{cpl}} = \frac{(\Delta F_0)_{slab}}{(\Delta F_0)_{cpl}} \quad (A2.4)$$

and *NEI* plays no role. Using Eq. (A2.4), the ratio of the ITCZ shifts is 2.87, nearly identical to the 2.81 estimated using shifts calculated from Eq. (A2.2b), which makes no assumptions about

changes in the equatorial energy balance. It is worth noting that these ratios are lower that the value of 4 we use in our paper because of the metric used to calculate the ITCZ shift (precipitation centroid versus energy flux equator), not the model setup.

References

Adam, O., T. Bischoff, and T. Schneider, 2016: Seasonal and Interannual Variations of the Energy Flux Equator and ITCZ. Part I: Zonally Averaged ITCZ Position. *J. Climate,* 29, 3219-3230, doi: 10.1175/JCLI-D-15-0512.1.

Adcroft, A., J. M. Campin, C. Hill, and J. Marshall, 2004: Implementation of an Atmosphere-Ocean General Circulation Model on the Expanded Spherical Cube. *Mon. Wea. Rev.*, 132, 2845-2863, doi: 10.1175/MWR2823.1.

Adler, R.F., and Coauthors, 2003: The Version-2 Global Precipitation Climatology Project (GPCP) Monthly Precipitation Analysis (1979-Present). *J. Hydrometeor.*, 4, 1147-1167, doi: http://dx.doi.org/10.1175/1525-7541(2003)004<1147:TVGPCP>2.0.CO;2.

Arbuszewski, J., P. B. deMenocal, C. Cleroux, L. Bradtmiller, and A. Mix, 2013: Meridional shifts of the Atlantic intertropical convergence zone since the Last Glacial Maximum. *Nat. Geosci.*, 6, 959-962, doi: 10.1038/NGEO1961.

Back, L. E., and C. S. Bretherton, 2009a: On the Relationship between SST gradients, Boundary Layer Winds, and Convergence over the Tropical Oceans. *J. Climate,* 22, 4182-4196, doi: 10.1175/2009JCLI2393.1.

Back, L. E., and C. S. Bretherton, 2009b: A Simple Model of Climatological Rainfall and Vertical Motion Patterns over the Tropical Oceans. *J. Climate,* 22, 6477-6497, doi: 10.1175/2009JCLI2393.1.

Bischoff, T., and T. Schneider, 2014: Energetic Constraints on the Position of the Intertropical Convergence Zone. *J. Climate,* 27, 4937-4951, doi: 10.1175/JCLI-D-13-00650.1.

Bischoff, T., and T. Schneider, 2016: The Equatorial Energy Balance, ITCZ Position, and Double-ITCZ Bifurcations. *J. Climate,* 29, 2997-3013, doi: 10.1175/JCLI-D-15-0328.1.

Boos, W. R., and R. L. Korty, 2016: Regional energy budget control of the intertropical convergence zone and application to mid-Holocene rainfall. *Nat. Geosci.,* 9, 892-897, doi: 10.1038/ngeo2833.

Bordoni, S., and T. Schneider, 2008: Monsoons as eddy-mediating regime transitions of the tropical overturning circulation. *Nat. Geosci.,* 1, 515-519, doi: 10.1038/ngeo248.

Boyle, E., and L. Keigwin, 1987: North Atlantic thermohaline circulation during the past 20,000 years linked to high-latitude surface temperature. *Nature,* 330, 35-40, doi: 10.1038/330035a0.

Bretherton, C. S., M. Widmann, V. P. Dymnikov, J. M. Wallace, and I. Blade, 1999: The effective number of spatial degrees of freedom of a time-varying field. *J. Climate,* 12, 1990-2009, doi: 10.1175/1520-0442(1999)012<1990:TENOSD>2.0.CO;2.

Broccoli, A. J., K. A. Dahl, and R. J. Stouffer, 2006: Response of the ITCZ to Northern Hemisphere cooling. *Geophys. Res. Lett.,* 33, L01702, doi: 10.1029/2005GL024546.

Buckley, M., and J. Marshall, 2016: Observations, inferences, and mechanisms of the Atlantic Meridional Overturning Circulation: A review. *Rev. Geophys.,* 54, 5-63, doi: 10.1002/2015RG000493.

Byrne, M. P., and P. A. O'Gorman, 2013: Land–Ocean Warming Contrast over a Wide Range of Climates: Convective Quasi-Equilibrium Theory and Idealized Simulations. *J. Climate,* 26, 4000-4016, doi: 10.1175/JCLI-D-12-00262.1.

Caballero, R., 2007: Role of eddies in the interannual variability of Hadley cell strength. *Geophys. Res. Lett.,* 34, doi: 10.1029/2007GL030971.

Charney, J. G., 1963: A Note on Large-Scale Motions in the Tropics, *J. Atmos. Sci.*, 20, 607-609.

Chiang, J. C., and C. M. Bitz, 2005: Influence of high latitude ice cover on the marine Intertropical Convergence Zone. *Climate Dyn.*, 25, 477-496, doi: 10.1007/s00382-005-0040-5.

Chiang, J. C. H., and A. R. Friedman, 2012: Extratropical cooling, interhemispheric thermal gradients, and tropical climate change. *Annu. Rev. Earth Planet. Sci.*, 40, 383-412, doi: 10.1146/annurev-earth-042711-105545.

Clement, A., K. Bellomo, L. N. Murphy, M. A. Cane, T. Mauritsen, G. Radel, and B. Stevens, 2015: The Atlantic Multidecadal Oscillation without a role for ocean circulation. *Science,* 350, 320-324, doi: 10.1126/science.aab3980.

Clement, A., M. A. Cane, L. N. Murphy, K. Bellomo, T. Mauritsen, and B. Stevens, 2016: Response to Comment on "The Atlantic Multidecadal Oscillation without a role for ocean circulation". *Science,* 352, 1527-1527, doi: 10.1126/science.aaf2575.

Compo, G. P., and Coauthors, 2011: The twentieth century reanalysis project. *Quart. J. Roy. Meteor. Soc.*, 137, 1-28, doi: 10.1002/qj.776.

Collins, J. A., A. Govin, S. Mulitza, D. Heslop, M. Zabel, J. Hartmann, U. Rohl, and G. Wefer, 2013: Abrupt shifts of the Sahara-Sahel boundary during Heinrich stadials. *Clim. Past,* 9, 1181-1191, doi: 10.5194/cp-9-1181-2013.

Czaja, A., and J. Marshall, 2006: The Partitioning of Poleward Heat Transport between the Atmosphere and Ocean. *J. Atmos. Sci.*, 63, 1498-1511, doi: 10.1175/JAS3695.1.

Dee, D. P., and Coauthors, 2011: The ERA-Interim reanalysis: Configuration and performance of the data assimilation system. *Quart. J. Roy. Meteor. Soc.*, 137, 553–597, doi: 10.1002/qj.828.

Deser, C., M. A. Alexander, S.-P. Xie, and A. S. Philips, 2010: Sea surface temperature variability: Patterns and mechanisms. *Annu. Rev. Mar. Sci.*, 2, 115-143, doi: 10.1146/annurev-marine-120408-151453.

Dima, I. M., and J. M. Wallace, 2003: On the Seasonality of the Hadley Cell. J. Atmos. Sci., 60, 1522-1527, doi: 10.1175/1520-0469(2003)060<1522:OTSOTH>2.0.CO;2.

Donohoe, A., J. Marshall, D. Ferreira, and D. McGee, 2013: The Relationship between ITCZ Location and Cross-Equatorial Atmospheric Heat Transport: From the Seasonal Cycle to the Last Glacial Maximum. *J. Climate,* 26, 3597-3618, doi: 10.1175/JCLI-D-12-00467.1.

Donohoe, A., J. Marshall, D. Ferreira, K. Armour, and D. McGee, 2014: The Interannual Variability of Tropical Precipitation and Interhemispheric Energy Transport. *J. Climate,* 27, 3377-3392, doi: 10.1175/JCLI-D-13-00499.1.

Donohoe, A., 2016: Atmospheric science: Energy and Precipitation. *Nat. Geosci.*, 9, 861-862, doi: 10.1038/ngeo2846.

Emanuel, K. A., J. D. Neelin, and C. S. Bretherton, 1994: On large-scale circulations in convecting atmospheres. *Quart. J. Roy. Meteor. Soc.*, 120, 1111-1143, doi: 10.1002/qj.49712051902.

Emanuel, K. A., 1995: On Thermally Direct Circulations in Moist Atmospheres. *J. Atmos. Sci.*, 52, 1529-1534, doi: 10.1175/1520-0469(1995)052<1529:OTDCIM>2.0.DO;2.

Enderton, D., and J. Marshall, 2009: Explorations of Atmosphere-Ocean-Ice Climates on an Aquaplanet and Their Meridional Energy Transports. *J. Atmos. Sci.*, 66, 1593-1611, doi: 10.1175/2008JAS2680.1.

Ferrari, R., and D. Ferreira, 2011: What processes drive the ocean heat transport? *Ocean Modell.*, 38, 171-186, doi: 10.1016/j.ocemod.2011.02.013.

Ferreira, D., J. Marshall, and J. M. Campin, 2010: Localization of Deep Water Formation: Role of Atmospheric Moisture Transport and Geometrical Constraints on Ocean Circulation. *J. Climate,* 23, 1456-1476, doi: 10.1175/2009JCLI3197.1.

Feulner, G., S. Rahmstorf, A. Levermann, and S. Volkwardt, 2013: On the Origin of the Surface Air Temperature Difference between the Hemispheres in Earth's Present-Day Climate. *J. Climate,* 26, 7136-7150, doi: 10.1175/JCLI-D-12-00636.1.

Flannery, B. P., 1984: Energy Balance Models Incorporating Transport of Thermal and Latent Energy. *J. Atmos. Sci.,* 41, 414-421, doi: 10.1175/1520-0469(1984)041<0414:EBMITO>2.0.CO;2.

Friedman, A. R., Y.-T. Hwang, J. C. Chiang, and D. M. W. Frierson, 2013: Interhemispheric Temperature Asymmetry over the Twentieth Century and in Future Projections. *J. Climate,* 26, 5419-5433, doi: 10.1175/JCLI-D-12-00525.1.

Frierson, D. M. W., 2007: The Dynamics of Idealized Convection Schemes and Their Effect on the Zonally Averaged Tropical Circulation. *J. Atmos. Sci.*, 64, 1959-1976, doi: 10.1175/JAS3935.1.

Frierson, D. M. W., I. M. Held, P. Zurita-Gotor, 2007: A Gray-Radiation Aquaplanet Moist GCM. Part II: Energy Transports in Altered Climates. *J. Atmos. Sci.*, 64, 1680-1693, doi: 10.1175/JAS3913.1.

Frierson, D. M. W., and Y.-T. Hwang, 2012: Extratropical influence on ITCZ shifts in slab ocean simulations of global warming. *J. Climate,* 25, 720-733, doi: 10.1175/JCLI-D-11-00116.1.

Frierson, D. M. W., Y.-T. Hwang, N. S. Fučkar, R. Seager, S. M. Kang, A. Donohoe, E. A. Maroon, X. Liu, and D. S. Battisti, 2013: Contribution of ocean overturning circulation to

tropical rainfall peak in the Northern Hemisphere. *Nat. Geosci.*, 6, 940-944, doi: 10.1038/ngeo1987.

Green, B., and J. Marshall, 2017: Coupling of Trade Winds with Ocean Circulation Damps ITCZ Shifts. *J. Climate,* 30, 4395-4411, doi:10.1175/JCLI-D-16-0818.1.

Green, B., J. Marshall, and A. Donohoe, 2017: Twentieth century correlations between extratropical SST variability and ITCZ shifts. *Geophys. Res. Lett.*, 44, 9039-9047, doi: 10.1002/2017GL075044.

Griffies, S. M., A. Gnanadesikan, R. C. Pacanowski, V. D. Larichev, J. K. Dukowicz, and R. D. Smith, 1998: Isoneutral Diffusion in a z-Coordinate Ocean Model. *J. Phys. Oceanogr.*, 28, 805-830, doi: 10.1175/1520-0485(1998)028<0805:IDIAZC>2.0.CO;2.

Griffies, S. M., and Coauthors, 2005: Formulation of an ocean model for global climate simulations. *Ocean Sci.*, 1, 45-79, doi: 10.5194/os-1-45-2005.

Gulev, S. K., M. Latif, N. Keenlyside, W. Park, and K. Koltermann, 2013: North Atlantic Ocean control on surface heat flux on multidecadal timescales. *Nature,* 499, 464-467, doi: 10.1038/nature12268.

Hawcroft, M., J. M. Haywood, M. Collins, A. Jones, A. C. Jones, and G. Stephens, 2016: Southern Ocean albedo, inter-hemispheric energy transports and the double ITCZ: global impacts of biases in a coupled model. *Climate Dyn.*, 1-17, doi: 10.1007/s00382-016-3205-5.

Heaviside, C., and A. Czaja, 2013: Deconstructing the Hadley cell heat transport. *Quart. J. Roy. Meteor. Soc.*, 139, 2181-2189, doi: 10.1002/qj.2085.

Held, I. M., and A. Y. Hou, 1980: Nonlinear Axially Symmetric Circulations in a Nearly Inviscid Atmosphere. *J. Atmos. Sci.*, 37, 515-533, doi: 10.1175/1520-0469(1980)037<0515:NASCIA>2.0.CO;2.

Held, I. M., 2001: The Partitioning of the Poleward Energy Transport between the Tropical Ocean and Atmosphere. *J. Atmos. Sci.*, 58, 943-948, doi: 10.1175/1520-0469(2001)058<0943:TPOTPE>2.0.CO;2.

Henry, L. G., J. F. McManus, W. B. Curry, N. L. Roberts, A. M. Piotrowski, and L. D. Keigwin, 2016: North Atlantic ocean circulation and abrupt climate change during the last glaciation. *Science*, 353, 470-474, doi: 10.1126/science.aaf5529.

Hersbach, H., C. Peubey, A. Simmons, P. Berrisford, P. Poli, and D. Dee, 2015: ERA-20CM: a twentieth-century atmospheric model ensemble. *Quart. J. Roy. Meteor. Soc.*, 141, 2350-2375, doi: 10.1002/qj.2528.

Hurrell, J. W., 1995: Decadal trends in the North Atlantic Oscillation: regional temperatures and precipitation. *Science*, 269, 676-679, doi: 10.1126/science.269.5224.676.

Hüttl-Kabus, S., and C. W. Böning, 2008: Pathways and variability of the off-equatorial undercurrents in the Atlantic Ocean. *J. Geophys. Res.*, 113, C10018, doi: 10.1029/2007JC004700.

Hwang, Y.-T., and D. M. W. Frierson, 2013: Link between the double-Intertropical Convergence Zone problem and cloud biases over the Southern Ocean. *Proc. Natl. Acad. Sci. U. S. A.*, 110, 4935-4940, doi: 10.1073/pnas.1213302110.

Jackett, D. R., and T. J. McDougall, 1995: Minimal Adjustment of Hydrographic Profiles to Achieve Static Stability. *J. Atmos. Oceanic Technol.*, 12, 381-389, doi: 10.1175/1520-0426(1995)012<0381:MAOHPT>2.0.CO;2.

Jayne, S. R., and J. Marotzke, 2001: The dynamics of ocean heat transport variability. *Rev. Geophys.*, 39, 385-411, doi: 10.1029/2000RG000084.

Kalnay, E., and Coauthors, 1996: The NCEP/NCAR 40-year reanalysis project. *Bull. Amer. Meteor. Soc.*, 77, 437-471, doi: 10.1175/1520-0477(1996)077<0437:TNYRP>2.0.CO;2.

Kang, S. M., I. M. Held, D. M. W. Frierson, and M. Zhao, 2008: The Response of the ITCZ to Extratropical Thermal Forcing: Idealized Slab-Ocean Experiments with a GCM. *J. Climate*, 21, 3521-3532, doi: 10.1175/2007JCLI2146.1.

Kang, S. M., D. M. W. Frierson, and I. M. Held, 2009: The tropical response to extratropical thermal forcing in an idealized GCM: The importance of radiative feedbacks and convective parameterization. *J. Atmos. Sci.*, 66, 2812-2827, doi: 10.1175/2009JAS2924.1.

Kang, S. M., I. M. Held, and S.-P. Xie, 2014: Contrasting the tropical responses to zonally asymmetric extratropical and tropical thermal forcing. *Climate Dyn.*, 42, 2033-2043, doi: 10.1007/s00382-013-1863-0.

Kang, S. M., Y. Shin, and S.-P. Xie, 2018: Extratropical forcing and tropical rainfall distribution: energetics framework and ocean Ekman advection. *npj Climate Atmos. Sci.*, 1, doi: 10.1038/s41612-017-0004-6.

Kay, J. E., C. Wall, V. Yettella, B. Medeiros, C. Hannay, P. Caldwell, and C. Bitz, 2016: Global Climate Impacts of Fixing the Southern Ocean Shortwave Radiation Bias in the Community Earth System Model (CESM). *J. Climate*, 29, 4617-4636, doi: 10.1175/JCLI-D-15-0358.1.

Kerr, R. A., 2000: A North Atlantic climate pacemaker for the centuries. *Science*, 288, 1984-1985, doi: 10.1126/science.288.5473.1984.

Klinger, B. A., and J. Marotzke, 2000: Meridional Heat Transport by the Subtropical Cell. *J. Phys. Oceanogr.*, 30, 696-705, doi: 10.1175/1520-0485(2000)030<0696:MHTBTS>2.0.CO;2.

Levine, X. J., and T. Schneider, 2011: Response of the Hadley Circulation to Climate Change in an Aquaplanet GCM Coupled to a Simple Representation of Ocean Heat Transport. *J. Atmos. Sci.*, 68, 769-783, doi: 10.1175/2010JAS3553.1.

Lindzen, R. S., and A. Y. Hou, 1988: Hadley Circulations for Zonally Averaged Heating Centered off the Equator. *J. Atmos. Sci.*, 45, 2416-2427, doi: 10.1175/1520-0469(1988)045<2416:HCFZAH>2.0.CO;2.

Loschnigg, J., and P. J. Webster, 2000: A Coupled Ocean-Atmosphere System of SST Modulation for the Indian Ocean. *J. Climate*, 13, 3342-3360, doi: 10.1175/1520-0442(2000)013<3342:ACOASO>2.0.CO;2.

Mantua, N. J., S. R. Hare, Y. Zhang, J. M. Wallace, and R. C. Francis, 1997: A Pacific interdecadal climate oscillation with impacts on salmon production. *Bull. Amer. Meteor. Soc.*, 78, 1069-1079, doi: 10.1175/1520-0477(1997)078<1069:APICOW>2.0.CO;2.

Marshall, J., A. Adcroft, C. Hill, L. Perelman, and C. Heisey, 1997a: A finite-volume, incompressible Navier Stokes model for studies of the ocean on parallel computers. *J. Geophys. Res.: Oceans*, 102, 5753-5766, doi: 10.1029/96JC02775.

Marshall, J., C. Hill, L. Perelman, and A. Adcroft, 1997b: Hydrostatic, quasi-hydrostatic, and nonhydrostatic ocean modeling. *J. Geophys. Res.: Oceans*, 102, 5733-5752, doi: 10.1029/96JC02776.

Marshall, J., and Coauthors, 2001: North Atlantic climate variability: phenomena, impacts and mechanisms. *Int. J. Climatol.*, 21, 1863-1898, doi: 10.1002/joc.693.

Marshall, J., and T. Radko, 2003: Residual mean solutions for the Antarctic Circumpolar Current and its associated overturning circulation. *J. Phys. Oceanogr.*, 33, 2341-2354, doi: 10.1175/1520-0485(2003)033<2341:RSFTAC>2.0.CO;2.

Marshall, J., A. Adcroft, J. M. Campin, C. Hill, and A. White, 2004: Atmosphere-Ocean Modeling Exploiting Fluid Isomorphisms. *Mon. Wea. Rev.*, 132, 2882-2894, doi: 10.1175/MWR2835.1.

Marshall, J., D. Ferreira, J.-M. Campin, and D. Enderton, 2007: Mean Climate and Variability of the Atmosphere and Ocean on an Aquaplanet. *J. Atmos. Sci.*, 64, 4270-4286, doi: 10.1175/2007JAS2226.1.

Marshall, J., A. Donohoe, D. Ferreira, and D. McGee, 2014: The ocean's role in setting the mean position of the Inter-Tropical Convergence Zone. *Climate Dyn.*, 42, 1967-1979, doi: 10.1007/s00382-013-1767-z.

McCreary Jr., J. P., and P. Lu, 1994: Interaction between the Subtropical and Equatorial Ocean Circulations: The Subtropical Cell. *J. Phys. Oceanogr.*, 24, 466-497.

McGee, D., A. Donohoe, J. Marshall, and D. Ferreira, 2014: Changes in ITCZ location and cross-equatorial heat transport at the Last Glacial Maximum, Heinrich Stadial 1, and the mid-Holocene. *Earth Planet. Sci. Lett.*, 390, 69-79, doi: 10.1016/j.epsl.2013.12.043.

McGee, D., E. Moreno-Chamarro, B. Green, J. Marshall, E. Galbraith, and L. Bradtmiller, 2018: Hemispherically asymmetric trade wind changes as signatures of past ITCZ shifts. *Quat. Sci. Rev.*, 180, 214-228, doi: 10.1016/j.quascirev.2017.11.020.

Mechoso, C. R., and Coauthors, 2016: Can reducing the incoming energy flux over the Southern Ocean in a CGCM improve its simulation of tropical climate? *Geophys. Res. Lett.*, 43, 11,057-11,063, doi: 10.1002/2016GL071150.

Merlis, T. M., 2015: Direct weakening of tropical circulations from masked CO_2 radiative forcing. *Proc. Natl. Acad. Sci. U. S. A.*, 112, 13167-13171, doi: 10.1073/pnas.1508268112.

Miyama, T., J. P. McCreary Jr., T. G. Jensen, J. Loschnigg, S. Godfrey, and A. Ishida, 2003: Structure and dynamics of the Indian-Ocean cross-equatorial cell. *Deep Sea Res., Part II,* 50, 2023-2047, doi: 10.1016/S0967-0645(03)00044-4.

Munk, W. H., 1950: On the wind-driven ocean circulation. *J. Meteor,* 7, 79-93, doi: 10.1175/1520-0469(1950)007<0080:OTWDOC>2.0.CO;2.

Neelin, J. D., and I. M. Held, 1987: Modeling Tropical Convergence Based on the Moist Static Energy Budget. *Mon. Wea. Rev.*, 115, 3-12, doi: 10.1175/1520-0493(1987)115<0003:MTCBOT>2.0.CO;2.

Neelin, J. D., 1997: Implications of Convective Quasi-Equilibrium for the Large-Scale Flow. *The Physics and Parameterization of Moist Atmospheric Convection,* R. K. Smith, Ed., Springer Netherlands, 413-446.

O'Reilly, C. H., M. Huber, T. Woollings, and L. Zanna, 2016: The signature of low frequency oceanic forcing in the Atlantic Multidecadal Oscillation. *Geophys. Res. Lett.*, 43, 2810-2818, doi: 10.1002/2016GL067925.

Peixoto, J. P., and A. H. Oort, 1992: *Physics of Climate.* American Institute of Physics, 555 pp.

Plumb, R. A., and A. Y. Hou, 1992: The Response of a Zonally Symmetric Atmosphere to Subtropical Thermal Forcing: Threshold Behavior. *J. Atmos. Sci.*, 49, 1790-1799, doi: 10.1175/1520-0469(1992)049<1790:TROAZS>2.0.CO;2.

Rayner, N. A., D. E. Parker, E. B. Horton, C. K. Folland, L. V. Alexander, D. P. Rowell, E. C. Kent, and A. Kaplan, 2003: Global analyses of sea surface temperature, sea ice, and night

marine air temperature since the late nineteenth century. *J. Geophys. Res.*, 108, 4407, doi: 10.1029/2002JD002670.

Ring, M. J., and R. A. Plumb, 2008: The Response of a Simplified GCM to Axisymmetric Forcings: Applicability of the Fluctuation-Dissipation Theorem. *J. Atmos. Sci.*, 65, 3880-3898, doi: 10.1175/2008JAS2773.1.

Rose, B. E. J., K. C. Armour, D. S. Battisti, N. Feldl, and D. D. B. Koll, 2014: The dependence of transient climate sensitivity and radiative feedbacks on the spatial pattern of ocean heat uptake. *Geophys. Res. Lett.*, 41, 1071-1078, doi: 10.1002/2013GL058955.

Schneider, E. K., 1977: Axially Symmetric Steady-State Models of the Basic State for Instability and Climate Studies. Part II. Nonlinear Calculations. *J. Atmos. Sci.*, 34, 280-296, doi: 10.1175/1520-0469(1977)034<0280:ASSSMO>2.0.CO;2.

Schneider, N., and B. D. Cornuelle, 2005: The Forcing of the Pacific Decadal Oscillation*. *J. Climate,* 18, 4355-4373, doi: 10.1175/JCLI3527.1.

Schneider, T., and S. Bordoni, 2008: Eddy-Mediated Regime Transitions in the Seasonal Cycle of a Hadley Circulation and Implications for Monsoon Dynamics. *J. Atmos. Sci.*, 65, 915-934, doi: 10.1175/2007JAS2415.1.

Schneider, T., T. Bischoff, and G. H. Haug, 2014: Migrations and dynamics of the intertropical convergence zone. *Nature,* 513, 45-53, doi: 10.1038/nature13636.

Schneider, T., 2017: Feedback of Atmosphere-Ocean Coupling on Shifts of the Intertropical Convergence Zone. *Geophys. Res. Lett.*, 44, 11,644-11,653, doi: 10.1002/2017GL075817.

Schott, F. A., M. Dengler, and R. Schoenefeldt, 2002: The shallow overturning circulation of the Indian Ocean. *Prog. Oceanogr.*, 53, 57-103, doi: 10.1016/S0079-6611(02)00039-3.

Schott, F. A., J. P. McCreary, G. C. Johnson, 2004: Shallow Overturning Circulations of the Tropical-Subtropical Oceans. *Earth's Climate: The Ocean-Atmosphere Interaction, Geophys. Monogr.*, Vol. 147, Amer. Gerophys. Union, 261-304, doi: 10.1029/147GM15.

Seo, J., S. M. Kang, and D. M. W. Frierson, 2014: Sensitivity of Intertropical Convergence Zone Movement to the Latitudinal Position of Thermal Forcing. *J. Climate,* 27, 3035-3042, doi: 10.1175/JCLI-D-13-00691.1.

Smith, T. M., P. A. Arkin, L. Ren, and S. S. P. Shen, 2012: Improved reconstruction of global precipitation since 1900. *J. Atmos. Oceanic Technol.*, 29, 1505-1517, doi: 10.1175/JTECH-D-12-00001.1.

Smith, T. M., S. S. P. Shen, L. Ren, and P. A. Arkin, 2013: Estimating monthly precipitation reconstruction uncertainty beginning in 1900. *J. Atmos. Oceanic Technol.*, 30, 1107-1122, doi: 10.1175/JTECH-D-12-00197.1.

Sobel, A. H., 2007: Simple models of ensemble-averaged precipitation and surface wind, given the sea surface temperature. *The Global Circulation of the Atmosphere,* T. Schneider and A. H. Sobel, Eds., Princeton Univ. Press, 219-251.

Stager, J. C., D. B. Ryves, B. M. Chase, and F. S. R. Pausata, 2011: Catastrophic Drought in the Afro-Asian Monsoon Region During Heinrich Event 1. *Science,* 331, 1299-1302, doi: 10.1126/science.1198322.

Sun, C., J. Li, F.-F. Jin, and R. Ding, 2013: Sea surface temperature inter-hemispheric dipole and its relation to tropical precipitation. *Environ. Res. Lett.*, 8, doi:10.1088/1748-9326/8/4/044006.

Tandon, N. F., E. P. Gerber, A. H. Sobel, and L. M. Polvani, 2013: Understanding Hadley Cell Expansion versus Contraction: Insights from Simplified Models and Implications for Recent Observations. *J. Climate,* 26, 4304-4321, doi: 10.1175/JCLI-D-12-00598.1.

Tomas, R. A., C. Deser, and L. Sun, 2016: The Role of Ocean Heat Transport in the Global Climate Response to Projected Arctic Sea Ice Loss. *J. Climate,* 29, 6841-6859, doi: 10.1175/JCLI-D-15-0651.1.

Trenberth, K. E., and J. M. Caron, 2001: Estimates of Meridional Atmosphere and Ocean Heat Transports. *J. Climate,* 14, 3433-3443, doi: 10.1175/1520-0442(2001)014<3433:EOMAAO>2.0.CO;2.

Trenberth, K. E., and D. J. Shea, 2006: Atlantic hurricanes and natural variability in 2005. *Geophys. Res. Lett.,* 33, doi: 10.1029/2006GL026894.

Tulloch, R., and J. Marshall, 2012: Exploring mechanisms of variability and predictability of Atlantic meridional overturning circulation in two coupled climate models. *J. Climate,* 25, 4067-4080, doi: 10.1175/JCLI-D-11-00460.1.

Voigt, A., B. Stevens, J. Bader, and T. Mauritsen, 2014: Compensation of Hemispheric Albedo Asymmetries by Shifts of the ITCZ and Tropical Clouds. *J. Climate,* 27, 1029-1045, doi: 10.1175/JCLI-D-13-00205.1.

Walker, C. C., and T. Schneider, 2006: Eddy Influences on Hadley Circulations: Runs with and Idealized GCM. *J. Atmos. Sci.,* 63, 3333-3350, doi: 10.1175/JAS3821.1.

Zelinka, M. D., and D. L. Hartmann, 2012: Climate Feedbacks and Their Implications for Poleward Energy Flux Changes in a Warming Climate. *J. Climate,* 25, 608-624, doi: 10.1175/JCLI-D-11-00096.1.

Zhang, R., and T. L. Delworth, 2005: Simulated Tropical Response to a Substantial Weakening of the Atlantic Thermohaline Circulation. *J. Climate,* 18, 1853-1860, doi: 10.1175/JCLI3460.1.

Zhang, R., and T. L. Delworth, 2006: Impact of Atlantic multidecadal oscillations on India/Sahel rainfall and Atlantic hurricanes. *Geophys. Res. Lett.,* 33, doi: 10.1029/2006GL026267.

Zhang, R., T. L. Delworth, and I. M. Held, 2007: Can the Atlantic Ocean drive the observed multidecadal variability in Northern Hemisphere mean temperature? *Geophys. Res. Lett.,* 34, doi: 10.1029/2006GL028683.

Zhang, R., R. Sutton, G. Danabasoglu, T. L. Delworth, W. M. Kim, J. Robson, and S. G. Yeager, 2016: Comment on "The Atlantic Multidecadal Oscillation without a role for ocean circulation". *Science,* 352, 1527-1527, doi: 10.1126/science.aaf1660.